FACULTY
OF MATHEMATICS
AND PHYSICS
Charles University

DOCTORAL THESIS

Andrés Pinar Solé

Study of Molecular Systems on Surfaces Investigated by Means of Scanning Probe Microscopy

Department of Surface and Plasma Science

Supervisor of the doctoral thesis: doc. Ing. Pavel Jelínek, Ph. D.

Study programme: Physics

Study branch: Physics of Surfaces and Interfaces

Prague 2024

I declare that I carried out this doctoral thesis independently, and only with the cited sources, literature and other professional sources. It has not been used to obtain another or the same degree.

I understand that my work relates to the rights and obligations under the Act No. 121/2000 Sb., the Copyright Act, as amended, in particular the fact that the Charles University has the right to conclude a license agreement on the use of this work as a school work pursuant to Section 60 subsection 1 of the Copyright Act.

In ..... date ....

Author's signature

Aknowledgements

I'd like to express my heartfelt thanks to Mr. Pavel Jelínek PhD, my supervisor, for giving me the opportunity to begin my doctoral journey. Under his guidance, I've not only learned important qualities like persistence, independent thinking, and attention to detail, but I've also gained a deep understanding of fascinating quantum phenomena. Mr. Jelínek has been a bridge between the worlds of experimentation and theory, and I'm truly grateful for his trust and support while giving me the opportunity to learn how to became a scientist. Besides the academic guidance he also embraced me on a personal level and was always available to offer help or advice, which to me is the most valuable of the aforementioned.

Furthermore, my thanks extend to Mr. Oleksandr Stetsovych PhD, my experimental mentor, whose generosity in sharing both his patience and expertise has been invaluable to my journey, and to Mr. Diego Soler Polo PhD for his detailed explanations and fruitful discussions about theory.

I also would like to thank my laboratory colleagues and coworkers in Prague and Olomouc. Their collaborative spirit, shared insights, and camaraderie have made the research environment enriching and fulfilling in many aspects, not only in the academic.

Finally, thanks to my family for their unwavering support and encouragement throughout this academic pursuit, they have been my pillars of strength.

Title: Study of Molecular Systems on Surfaces Investigated by Means of Scanning Probe Microscopy

Author: Andrés Pinar Solé

Department: Department of Surface and Plasma Science

Supervisor: doc. Ing. Pavel Jelínek, Ph. D., Institute of Physics of the ASCR

Abstract: The primary objective of this thesis is to provide a comprehensive assessment of why the nickelocene molecule distinguishes itself as a viable candidate for investigating magnetic properties in molecular systems. After covering both its experimental and theoretical framework, the magnetic characterization and theoretical simulations of various molecular systems using the nickelocene STM tip are described. In addition, the cobaltocene molecule is introduced as another viable spin sensor.

Keywords: SPM, STM, nc-AFM, STS, IETS, tip functionalization, exchange interaction, molecular magnetism, magnetic characterization.

Contents

Introduction

In the realm of Scanning Tunneling Microscopy (SPM), the magnetic ground state of a target molecule is probed by employing a metallic tip and examining its inelastic electron spin spectroscopy (IETS) characteristics. The magnetic probing capabilities of the SPM can be enhanced by decorating the SPM tip with different kinds of molecules and atoms with magnetic properties. The use of SPM tip functionalization extends beyond magnetic characterization. A notable illustration of this technique is observed in non-contact atomic force microscopy (nc-AFM), where CO tips are frequently employed to achieve high-resolution atomic-scale imaging. In the context of magnetic characterization, the application of spin-polarized SPM tips has emerged, involving the functionalization of SPM tips with atoms or molecules to acquire magnetic information and perform IETS. However, the reliability and reproducibility of this approach often face challenges when it comes to determining the state of the tip after the polarization process. Within this context, the nickelocene molecule emerges as a candidate by behaving in a controlled and reproducible manner as the absorption process onto the tip can be meticulously managed, resulting in highly reproducible spectra. The cyclopentadienyl rings protect the molecule from bonding with the sample, conserving its spin as a good quantum number, facilitating electron exchange coupling, and enabling the extraction of information from the magnetic system. The cobaltocene molecule exhibits numerous similarities with nickelocene, except for the spin, rendering it another compelling alternative for investigating molecular magnetism.

During my Ph.D., I focused on mastering the SPM techniques and sample preparation (Chapter 1). I became familiar with the state of the art regarding the utilization of nickelocene as a magnetic sensor (Chapter 2). I also acquired knowledge about the theoretical tools needed to analyze nickelocene's spectrum and developed a Python script, created by my colleagues from the theory department, to simulate the experiments. I further analyzed some previous works with this simulation script (Chapter 2). Finally, I utilized nickelocene to gain insights into various magnetic systems (Chapter 3).

Chapter 1

Scanning Probe Microscopy

Scanning Probe Microscopy (SPM) is a nanoscale investigative tool whose uniqueness lies in its capacity to not only visualize but also manipulate matter at the nanoscale. This technique employs a microscopic probe as a sensitive detector, to explore and discern the local properties of surfaces and interfaces with spatial precision. This thesis mainly focuses on the Scanning Tunneling Microscope (STM) complemented with non-contact Atomic Force Microscopy (nc-AFM) and its implementation for studying magnetic molecular systems by Inelastic Electron Tunneling Spectroscopy (IETS).

1.1 Scanning Tunneling Microscopy (STM)

Scanning Tunneling Microscopy has been a leading technique in nanoscale investigations since its inception in the early 1980s[1]. In essence, STM relies on the principle of quantum tunneling, a quantum mechanical phenomenon where electrons exhibit a non-zero probability of traversing a potential vacuum barrier that would be forbidden according to classical mechanics [2–4]. In the context of STM, this tunneling barrier is the vacuum gap that separates the metallic tip from the conductive sample surface. To put this principle into

practice, a bias voltage is applied to the sample, and the tip is brought into close proximity to the surface. Under these conditions, electrons can tunnel through the vacuum barrier, resulting in a measurable current, typically in the order of $I \approx 10$ pA, flowing from the sample to the tip or vice versa depending on the bias polarity.

The tip-sample distance and tunneling current are closely related. A tip-sample distance approach of 100 pm corresponds to an order of magnitude increment in the tunneling current [2]. This exponential behavior of the tunneling current with the tip-sample distance arises from the wavefunction of the tunneling electrons, which undergoes exponential decay when facing the finite potential vacuum gap. This wavefunction plays a pivotal role in determining the likelihood of finding the density of states on the opposite side of the potential barrier (the sample). The solution to the time-independent Schrödinger equation within the region defined by the barrier serves as a foundational element for the Bardeen tunneling theory [5]. It is employed to provide an approximate explanation for the quantum phenomena observed in STM by modeling it as electrodes that are brought into close proximity, enabling tunneling phenomena. When the electrodes A and B (Fig. 1.2) are far apart, their wavefunctions satisfy the Schrodinger equation of the free electron:

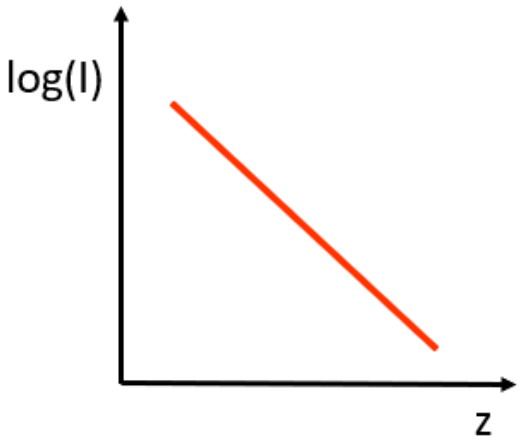

Figure 1.1: Logarithmic dependance of the current (I) and the tip-sample distance (Z) in an STM.

$$i\hbar\frac{\partial\Psi}{\partial t} = \left(-\frac{\hbar^2}{2m_e}\frac{\partial^2}{\partial z^2} + U\right)\Psi, \tag{1.1}$$

where U is the vacuum barrier potential and Ψ is the wavefunction of any of the

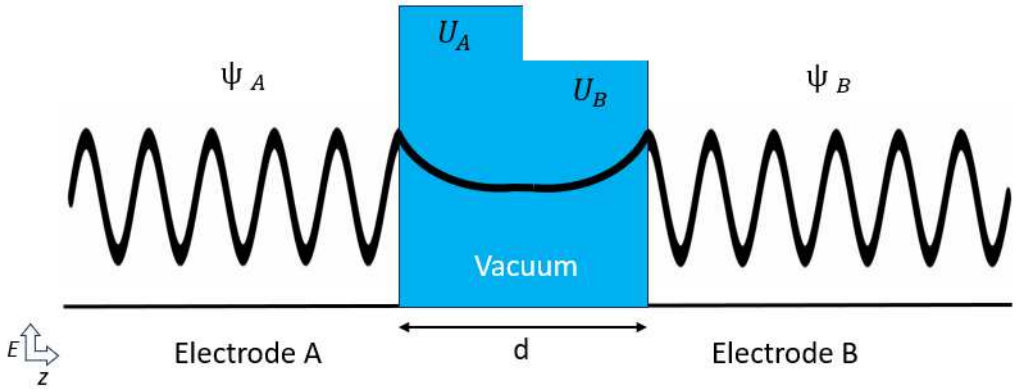

Figure 1.2: The free electron wavefunctions Ψ_A, Ψ_B from the electrodes A and B exponentially decay when reaching the vacuum barrier (blue) composed by the potentials U_A, U_B. As the electrodes get closer reducing the vacuum gap distance d, these wavefunctions overlap making available quantum tunneling.

electrodes. By bringing the electrodes together (Fig. 1.2), their wavefunctions Ψ_A, Ψ_B and their potentials U_A, U_B merge to fulfill the Schrodinger equation of the combined system:

$$i\hbar\frac{\partial\Psi}{\partial t} = \left(-\frac{\hbar^2}{2m_e}\frac{\partial^2}{\partial z^2} + U_A + U_B\right)\Psi. \tag{1.2}$$

The evaluation of the tunneling current involves the application of time-dependent perturbation theory (Eq. 1.2) and is the basis of STM principle. The probability of finding an electron at position d on the other side of the vacuum barrier is approximately proportional to $|\Psi(d)|^2 = |\Psi(0)|^2 T(\Phi, d)$.

From this approach one can extract $T(\Phi, d)$, the transmission factor, which dictates the probability of an electron tunneling event between the tip and the sample as a function of the work function Φ and the tip-sample distance d. The work function Φ (height of the tunneling barrier) defines the energy needed for an electron to abandon the solid. As the tip and the sample usually have different work functions, the average is considered $\Phi = (\Phi_{tip} + \Phi_{sample})/2$. The transmission factor approximates to:

$$T(\Phi, d) \propto exp\left(-2d\sqrt{\frac{2m}{\hbar^2}\Phi}\right). \tag{1.3}$$

The Fermi levels of the tip and the sample can be shifted by applying a bias voltage V, and the electrons will tunnel from the tip to the sample or the opposite way, depending on the bias polarity. Including the bias shift, the transmission factor can be approximated as:

$$T(\Phi, d, \epsilon, V) \propto exp\left(\frac{-8dm^2}{\hbar}\sqrt{\Phi + \frac{V}{2} - \epsilon}\right). \tag{1.4}$$

where ϵ is the energy relative to the Fermi energy. The tunneling current can be obtained by integrating the solution of Eq.1.2 over all A and B states weighted by their occupation probability, taking into to account the charge of each electron and the spin multiplicity. Assuming cryogenic temperatures (T<10 K), K_bT is smaller than the energy resolution (K_b is the Boltzmann constant). This implies that the Fermi-Dirac distribution of the electrons over the states $f(E) = 1 + exp(\frac{E-E_F}{K_BT})$ gets closer to a step function and the tunneling current approximates to:

$$I = \frac{4\pi e}{\hbar}\int_0^V \rho_t(E_F - V + \epsilon)\rho_s(E_F + \epsilon)T(\Phi, d, \epsilon, V)d\epsilon, \tag{1.5}$$

where ρ_t ρ_s are the density of states of the tip and the sample.

Following the expressions 1.5 and 1.4, we can assume that the tunneling probability is inversely proportional to the tip-sample distance d and the tunneling barrier ϕ. Furthermore, electrons whose energy ϵ is close to V are more likely to tunnel and contribute the most to the tunneling current, while the current itself will be a weighted sum of all electron's tunnel probability depending on their energies relative to V.

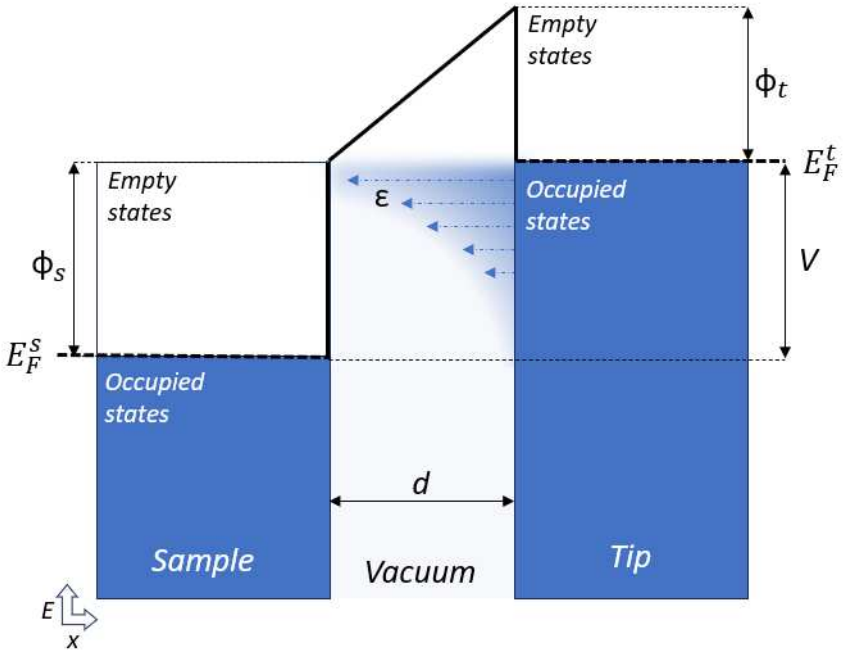

Figure 1.3: Energy diagram of an STM junction in 1D. From the initially leveled Fermi energies at absolute zero temperature, the system evolves by applying a bias voltage V, and a shift in energy appears between the sample and tip's occupied states. As the electrons have more energy, they acquire a probability to tunnel from the occupied states of the tip to the empty states of the sample, being more likely to tunnel closer to the tip's Fermi energy.

1.1.1 STM working principle

Once the tip and the sample are brought together the distance between them needs to be controlled by adjusting the current I and the bias V to scan and extract information from the STM. At a fixed bias, a certain tip-sample distance d (commonly referred to as tip height in the z-direction perpendicular to the sample) corresponds to a certain current value. The current I will strongly vary as a function of the height d and the bias V. STM scanning is typically performed using two different modes: constant current and constant height (Fig. 1.4) [2].

Constant current STM mode

In constant current mode, the bias V and the current I are fixed values. As the scanning tip moves across the surface in both the horizontal (x and y) directions, a feedback system continually adjusts the tip's height by moving it closer to or farther away from the sample surface aiming to keep the tunneling current between the tip and the sample at the setpoint value. When the scanning tip encounters an atomic step or molecule on the surface and moves laterally towards it during the scan, the tunneling current increases due to the reduced distance between the tip and the sample. By recording the feedback signal, which corresponds to the tip's height d as a function of its lateral position, a map or image of the tip's height is generated. This image reflects the apparent STM surface topography of the sample at a certain bias, not the real topography, as the surface topography based solely on constant tunneling current is a simplified approximation. For instance, an atom with higher conductivity will appear taller, while the less conductive atom will require the tip to approach closer to maintain the same tunneling current.

Before the current I is corrected by the feedback, it needs to be filtered, transformed into a DC voltage signal, and amplified to enable scanning. Typical tunneling current setpoints are usually around 1 pA to 10 nA, and for that, the Femto operational amplifier

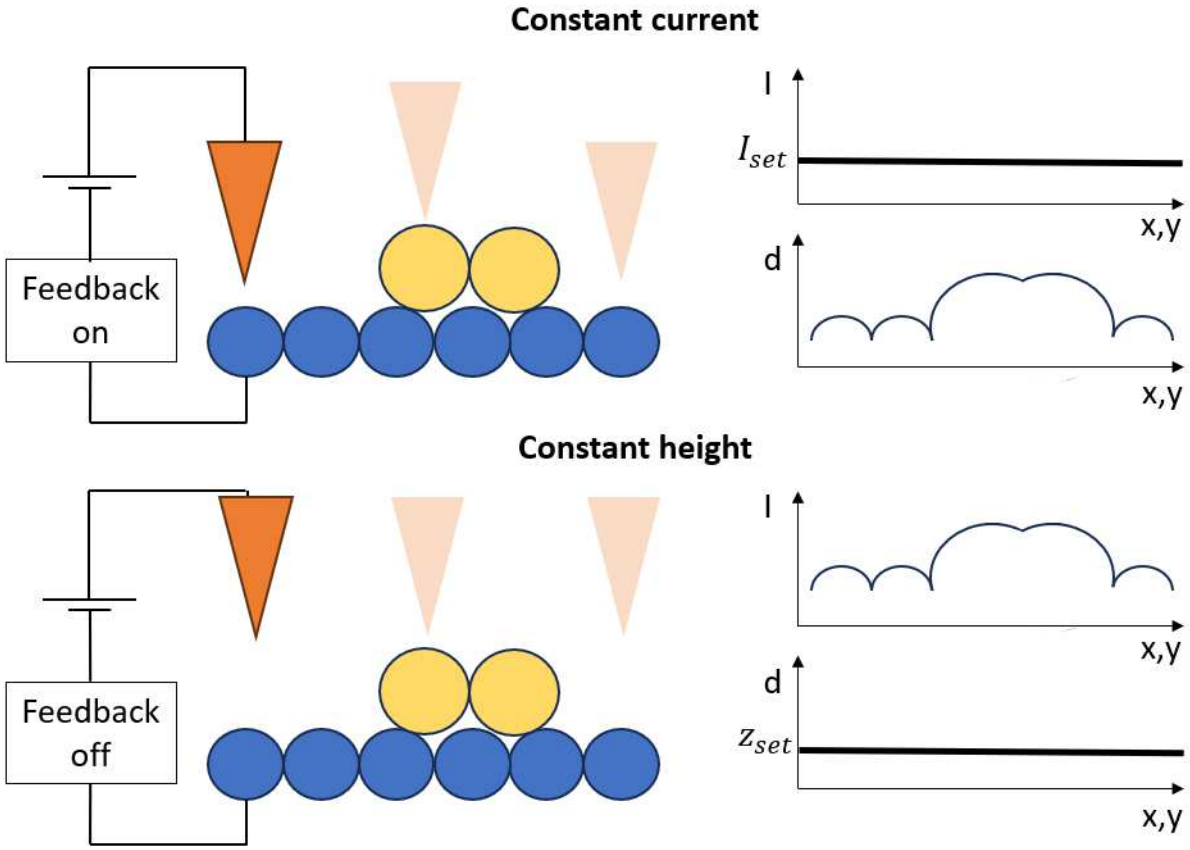

Figure 1.4: The STM tip (orange) scans over the sample's atoms (blue and yellow) in the x,y direction at a constant bias V. When the feedback is on (closed loop), the STM keeps the current constant at the given setpoint by retracting or approaching the tip towards the sample in the z direction, compensating the tip-sample distance d as it scans in the x,y plane. In the constant height mode, the feedback loop is open and the current changes as the tip-sample distance and the conductivity of the species varies.

was utilized. The feedback loop is responsible for maintaining the setpoint tunneling current between the tip and the sample by varying the tip-sample distance as the scanning probe moves across the surface in the X and Y directions. The core components of the feedback loop include the system output (the actual tunneling current), the current setpoint, and the proportional-integral (PI) controller. Its function is to adjust the voltage applied to the z-piezo element, which controls the tip-sample distance. In the proportional controller, the controlling factor is directly related to the error signal $I_{in}(t) - I_{set}(t)$, where I_{in} is the

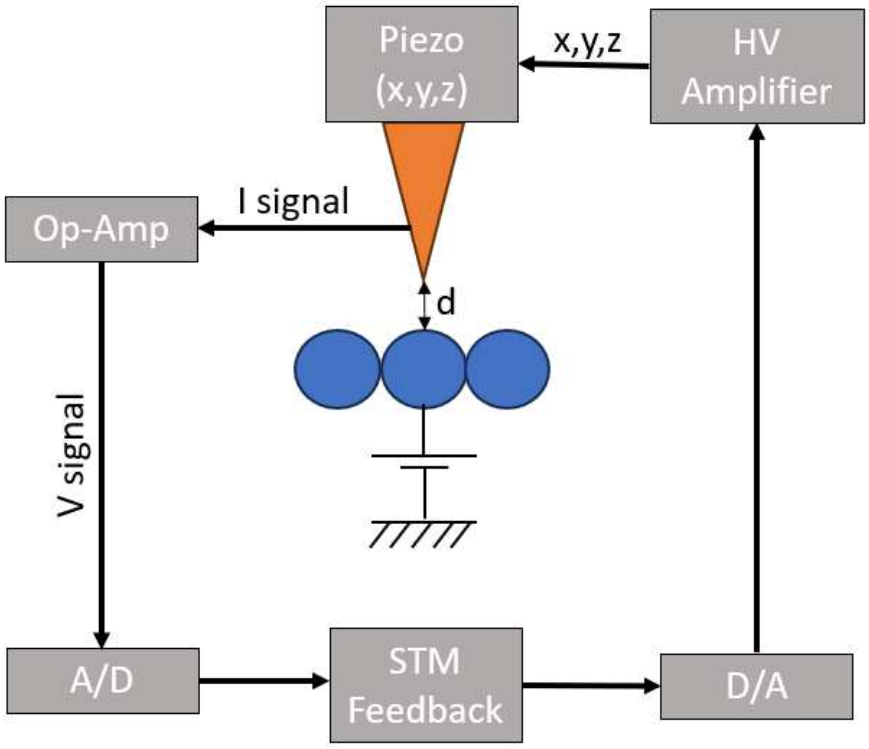

Figure 1.5: STM diagram. The tunneling current signal is generated between the biased tip-sample junction, then it is amplified and transformed into a voltage signal using a series of op-amps. Subsequently, the signal is digitized and incorporated into the feedback loop, where it is compared with the current setpoint. The feedback loop generates an output signal containing information for the piezos to correct the tip-sample distance and follow the feedback. Prior to reaching the piezo, this signal must undergo analog conversion and amplification by the high voltage amplifier.

input current signal, and I_{set} is the current setpoint. On the other hand, in the integral controller, the controlling factor is linked to the accumulated error signal over time. Typical proportional values range between 1-10 pm, depending on the scanning speed and the roughness of the surface. A larger proportional constant K_p implies a quicker response since the larger the error, the larger the compensation, acting like a low-pass filter. However, an excessively large proportional value will lead to instability. Larger integration constant K_i values eliminate steady-state errors more quickly, but an excess will overshoot the current setpoint, smearing the contrast. Common values range between 1-100 nm/s.

$$I(t) = K_p(I_{in}(t) - I_{set}(t)) + K_i \int_0^t (I_{in}(t) - I_{set}(t))dt \tag{1.6}$$

The analog current signal coming from the junction must be transformed into a digital signal in order to be fed to the feedback, and consequently, the feedback signal must be transformed back again to analog and amplified before it actuates the piezo elements to follow the topography (Fig. 1.5).

Constant height STM mode

In constant height mode, the tip-sample distance d remains unchanged, and the STM scans with the feedback loop open at a specified bias V. It enables faster scanning since the signal does not require integration time by the feedback and is employed for probing flat samples within smaller scan frames to prevent collisions with the sample's 3D profile. The constant height mode is sensitive to creep and drift effects caused by thermal and hysteresis of the piezo components. These effects may alter the tip's position relative to the sample over time if the feedback does not compensate for them. Therefore, constant height mode should be utilized under creep/drift-free conditions. This mode is also employed to determine the frequency shift image in non-constant AFM or the conductance image in dI/dV mapping.

1.2 Non-contact Atomic Force Microscopy (nc-AFM)

The dynamic non-contact Atomic Force Microscope (nc-AFM) relies on the force acting between the sample and the tip when brought to close proximity [2, 6–8]. In contrast to STM, nc-AFM does not require a conductive substrate, offering several advantages when probing insulators. Moreover, nc-AFM allows atomic resolution and accurate height determination of the topography.

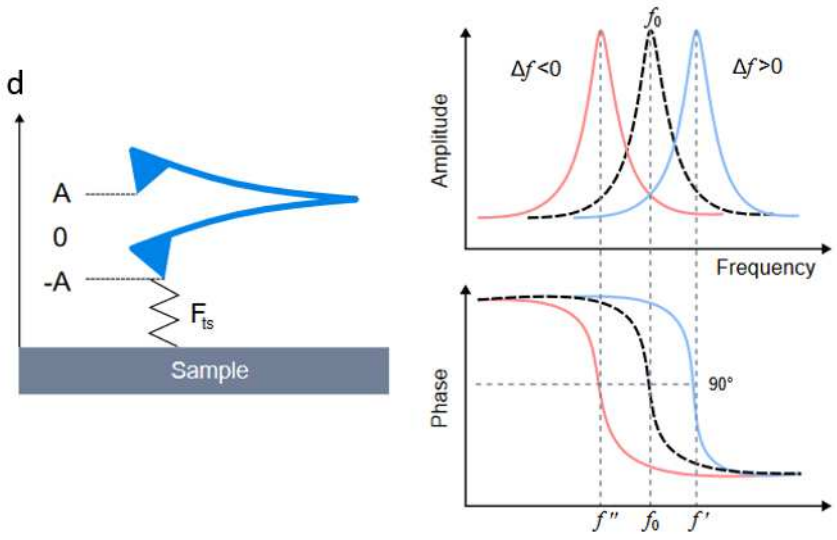

Figure 1.6: Representation of a cantilever oscillating on a force field F_{ts} created by the sample. The force effect shifts the resonant frequency and phase [9]

The most common nc-AFM sensors are atomically sharpened tips glued to a quartz resonator that can provide controlled oscillations [2, 6, 7]. The physical principle that allows nc-AFM consists of the force interaction between the tip and the sample, which has two contributions: long and short-range interactions. The long-range interactions mainly consist of van der Waals, electrostatic and magnetic forces extending up to several nanometers, and the short-range interaction correspond to the Pauli repulsion and chemical bonding, active for tip-sample distances < 1 nm. The overall force field can be described with the Lennard-Jones-like potential (Fig. 1.7), where initially, the main interaction is attractive,

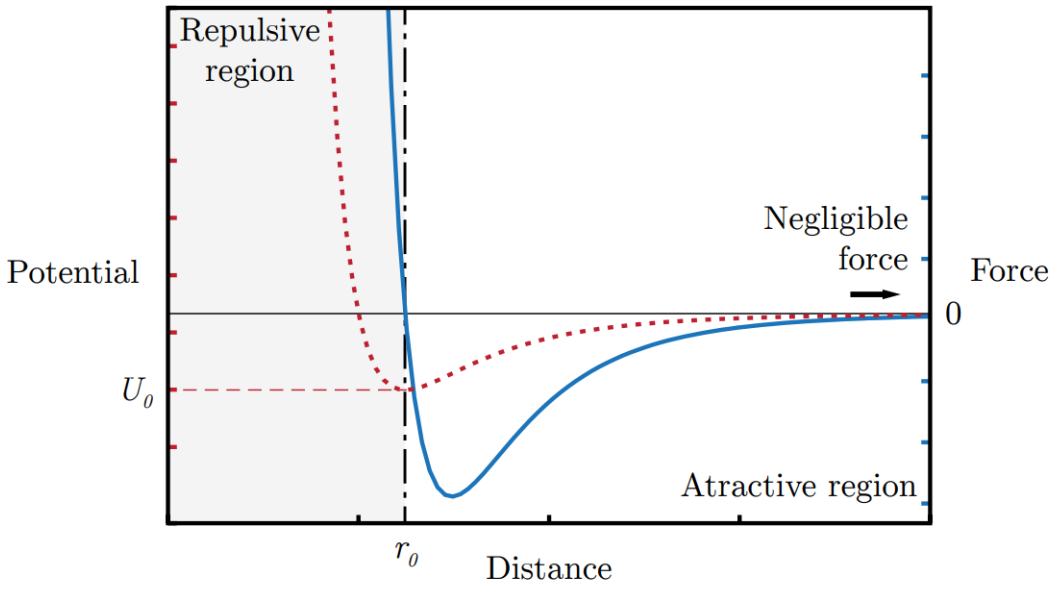

Figure 1.7: Lennard-Jones potential (red dotted line) and the result of attractive and repulsive forces on the tip (blue line) [10]. U_0 is the depth of the potential well and r_0 correspond to the tip sample separation where the force is zero.

followed by a balance between repulsive and attractive (minima), and finally, the repulsive regime is achieved at $<$ 500 pm distance.

To sense the force field, the tip is attached to an oscillator (cantilever) with an amplitude A, a resonance frequency f_0, spring constant k_0, and quality factor Q. When the tip interacts with the sample, changes in the amplitude and phase are proportional to the interaction. The force experienced by the cantilever is also proportional to the frequency shift Δf of the resonant frequency of the oscillator (Fig. 1.6). This relationship cna be better explained by looking to the dynamic equation of motion of a cantilever damped by a non-linear tip-sample force F_{ts} [2] :

$$m\ddot{z} + \frac{mf_0}{Q}\dot{z} + k(z_0 - z_{drive} - \Delta L) = F_{ts}(d + z_0). \tag{1.7}$$

The zero point (z_0) corresponds to the position where the force F_{ts} is compensated by the cantilever bending δL, with the tip-sample distance being d. The relationship between

Figure 1.8: A Kolibri (left) and qPlus sensor (right)

tip-sample forces and the frequency shift can be obtained by assuming small amplitudes over a weighted average of the tip-sample force F_{ts} over an oscillation. After this simplification, one can arrive to the expression of the frequency shift [11, 12]:

$$\Delta f = f - f_0 - \frac{f_0}{k_0 A^2} \left\langle A F_{ts}(t) \cos(2\pi f_0 t) \right\rangle \tag{1.8}$$

The oscillator must be kept at its resonant frequency f_0 and a given amplitude A with a feedback loop that continuously compares the oscillation frequency with the resonant frequency to obtain the frequency shift. To perform this operation, a phase-locked-loop (PLL) is installed[13]. It transforms the AFM signal into digital or analog as needed and keeps the oscillator at a determined frequency and amplitude of oscillation by applying a 90-degree phased signal (resonant condition of a driven harmonic oscillator). Depending on the kind of measurements to perform, the amplitude of oscillation must be set accordingly. To sense on the regime where the long range forces are prevalent over the short range forces ($d>$ 500 pm), the amplitude must be 100-200 pm to fully capture the interaction ($\Delta f \approx 10 - 100$ Hz), while for sensing short-range forces disregarding the long range forces effect ($d<$ 500 pm), the amplitude setpoint is usually 20-50 pm ($\Delta f \approx 5$ Hz).

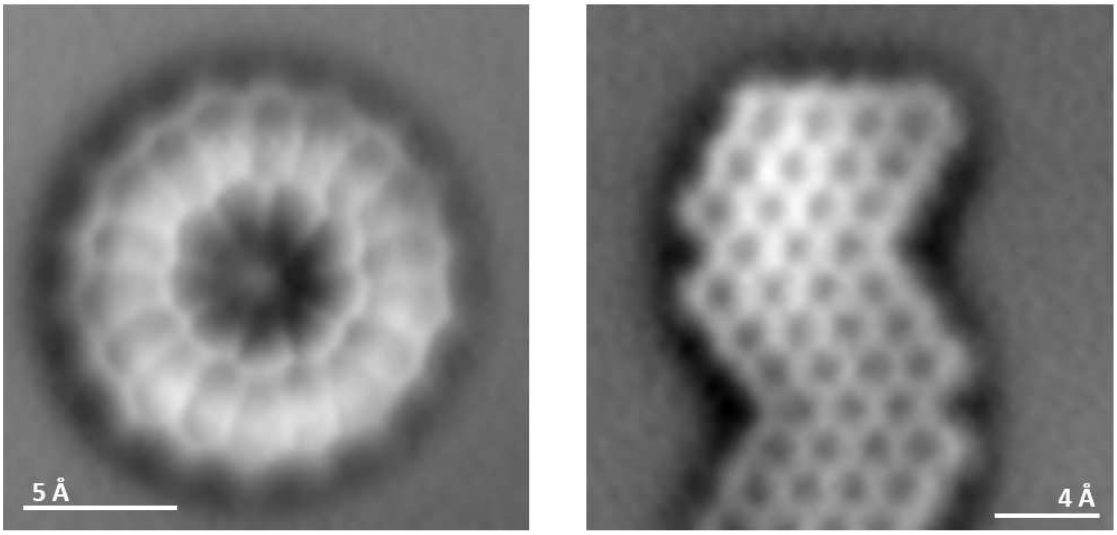

Figure 1.9: nc-AFM high resolution images with a CO functionalized tip. The left image corresponds to a polyradical hydrocarbon ring measured with a qPlus sensor, and the right side corresponds to a graphene nanoribbon measured with a Kolibri sensor.

SPM tips can be installed in quartz oscillators to enable nc-AFM measurements as well as STM measurements. The most common ones are the qPlus[12] and the Kolibri[14] sensors (Fig. 1.10). In the case of the qPlus, the quartz resonator is mounted in a tuning fork-shaped metal part where the tip is glued, having a resonant frequency $f \approx 30$ kHz. In the case of the Kolibri, the oscillation occurs in the longitudinal axis and is encapsulated by a metal cap to protect the device in case of sputtering. It usually has a resonant frequency of $f \approx 1$ MHz[15].

1.3 SPM tip preparation and functionalization

1.3.1 Tip preparation

The most common SPM tips are made of tungsten after electrochemical etching by the DC drop-off method[2][16], where a tungsten wire with a diameter of 200-500 μm is immersed in a solution containing NaOH and maintained at a positive potential relative to a stainless steel electrode until the etched material drops off the wire, creating a very sharp termination. Additionally, platinum-iridium tips are commonly fabricated. The SPM tips can be macroscopically sharpened by applying FIB etching[17].

A fresh tip needs to be poked onto a metallic substrate several times under certain bias conditions to melt atoms from the surface and get coated by them in order to acquire its final microscopic sharpness. In particular, for nc-AFM measurements, the sharpness of the tip e.g. its radius influences the long-range electrostatic interaction of the tip with the sample, so typically very sharp tips have very low frequency shift ($<$ 500 mHz) when measuring in standard scanning STM conditions (100 mV, 10 pA, 50 pm amplitude)[18]. Tip shaping generally implies approximately 1-2 nm indentations into the metallic substrate and 5-10V pulses, both positive and negative biased, depending on the desired tip shape.

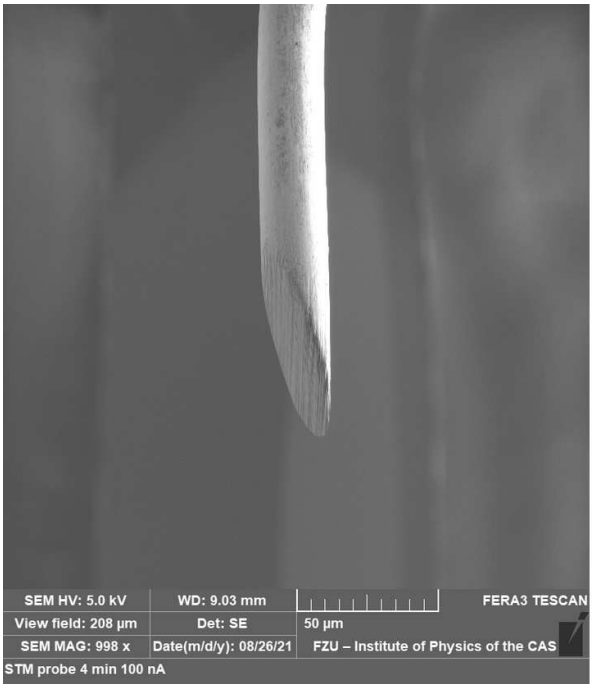

Figure 1.10: TEM image of a FIB etched QPlus Pt-Ir tip. The width is 20 μm

1.3.2 Tip functionalization

The nc-AFM can improve its resolution by attaching a carbon monoxide (CO) molecule to the sensor's tip (tip functionalization) [11, 12]. As the O atom does not possess free radicals to bond with the substrate, it is a passive apex. Subsequently, the CO-passivated tip allows close regime scanning when scanning the sample in constant height mode. The CO bends over the topography to acquire atomic resolution from the frequency shift channel (Fig. 1.11) [11, 12, 19]. Atomic resolution imaging becomes available with this kind of tip functionalization [18] (Fig. 1.9). Many other atoms and molecules have been utilized to perform nc-AFM high resolution imaging (Xe, Cl, Br, N_2O) [20, 21] or probing charged systems [22].

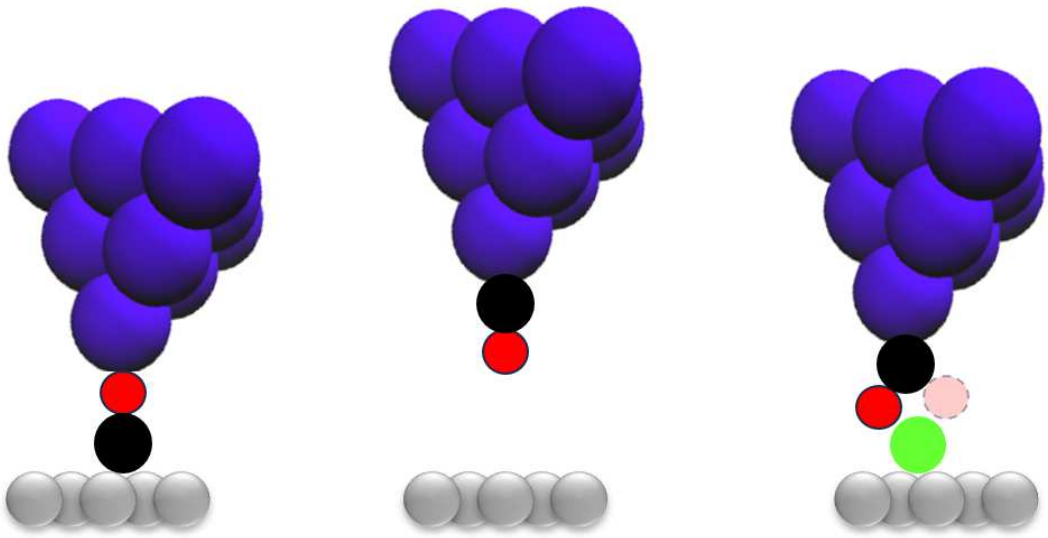

Figure 1.11: CO (black=C, red=O) functionalization and CO-tip bending when probing an adatom (green).

Tip functionalization has many uses beyond nc-AFM, such as the magnetic characterization of systems by spin-polarized tips [23–25]. When the STM tip becomes polarized, electrons with spins aligned to the orientation of the magnetized tip are significantly more likely to tunnel through the vacuum barrier. This phenomenon is known as tunnel magne-

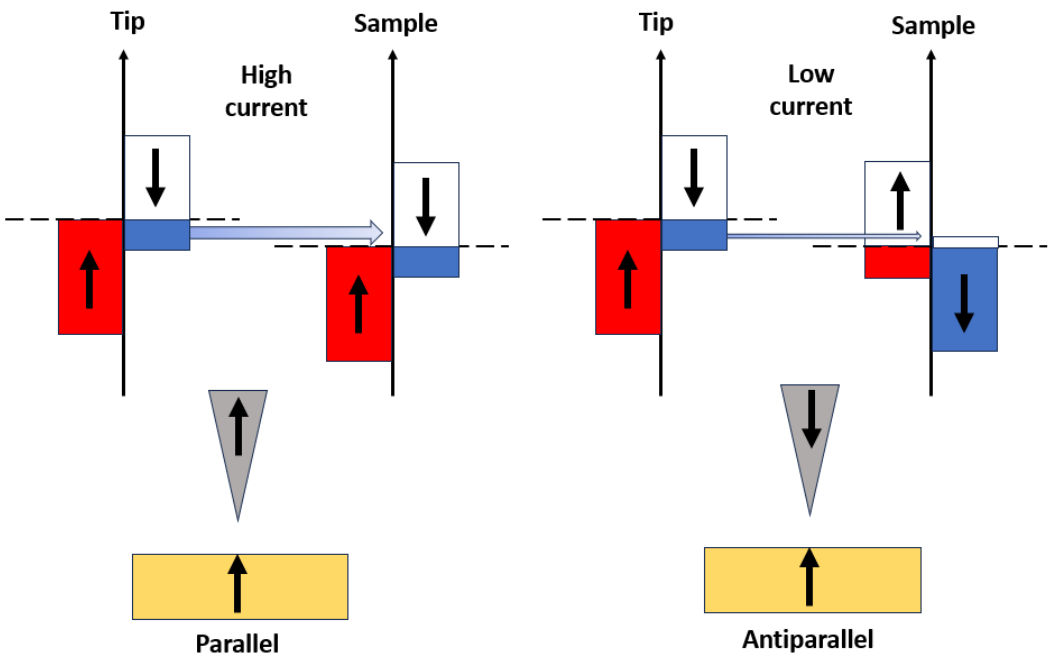

Figure 1.12: Difference in current from an STM spin-polarized tip experiment. In the parallel configuration, the density of states of the same spin is half-filled, and tunneling is favorable when there is an energy shift from the filled-up spin states to the empty-up spin states. In the antiparallel configuration, the polarity of the filled and empty states is opposite, resulting in much lower current.

toresistance [26, 27], where the tunneling current varies depending on the relative alignment of electron spins between the tip and the sample surface. In essence, this configuration transforms the tip and the surface into a functional analog of a spin valve, capable of regulating the flow of electrons with varying spin orientations (Fig. 1.12).

These tips are tailored by introducing atoms like Fe and Mn [24], as well as Cr [25], imparting a form of spin selectivity when subjected to external magnetic fields. Spin-polarized tips are fabricated by replacing the predominant metal atoms on the STM tip with the specified atomic species. Techniques such as atomic manipulation [28] or contact with clusters of magnetic atoms on the surface [29] are employed to accomplish this STM functionalization. The most commonly utilized functionalized tips nowadays are Fe, as they are used to implement Electron Spin Resonance (ESR) [30]. To prepare an Fe-polarized tip,

the most common approach is to pick up Fe atoms deposited on an MgO bilayer over an Ag(100) substrate by pulsing 600 mV and indenting 230 pm at 100 mV at 10 pA tunneling conditions. This ensures a single-atom pickup. To polarize the tip, 5-20 Fe atoms are needed, as the ESR capabilities are not easily reproducible with any polarized tip. To check the polarization, the Fe is probed on top of another Fe atom, looking for pronounced step-like asymmetries in the dI/dV in the positive and negative branches of the spectrum. Depending on the system and the setup, a significant number of tries are necessary before fabricating a spin-polarized tip, and its properties will differ from one another due to the inherent randomness of the process of picking Fe atoms and creating a magnetic cluster on the tip.

1.4 Technical requirements of the SPM

In order to perform SPM measurements, the microscope demands very particular experimental conditions and technical requirements to function, e.g. a stable and noise-free SPM junction, ultra high vacuum (UHV) or cryogenic temperatures. Together, these foundational elements enable the SPM to achieve its precision.

1.4.1 Ultra High Vacuum conditions

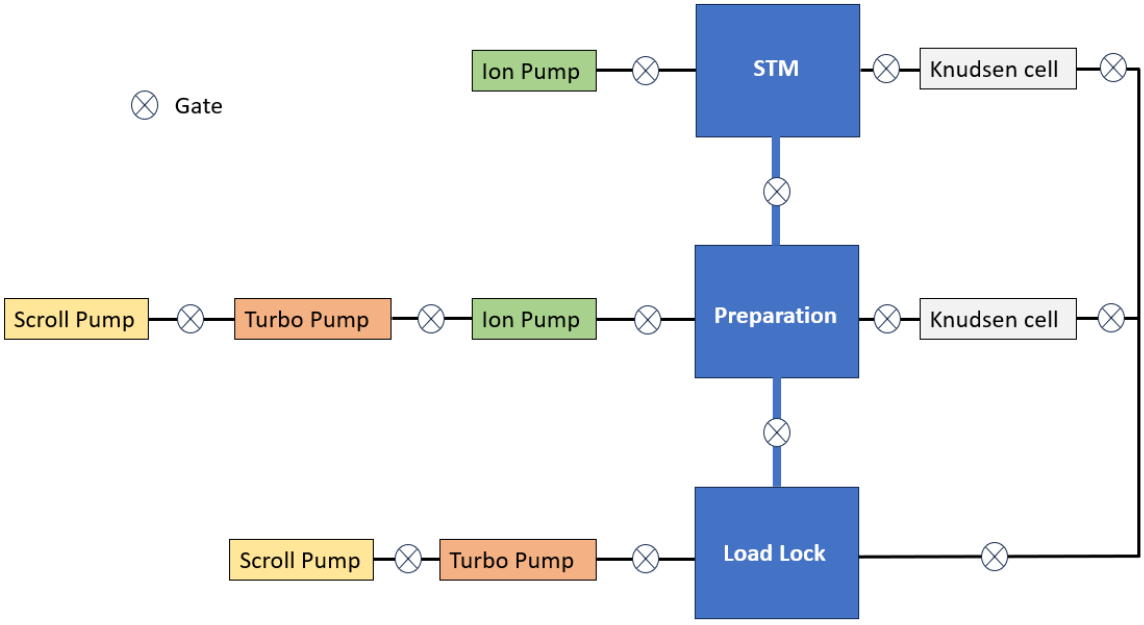

Figure 1.13: Pumping diagram of the SPM. The sample is inserted trough the load lock, pumped to reach UHV ($\approx 10^{-8} mBar$) and then transferred to the preparation chamber ($\approx 10^{-9} mBar$) to clean it and prepare the system to probe, usually by evaporating materials by Knudsen cell. Lastly, the prepared sample is transferred to the cryogenic STM chamber at $\approx 10^{-10} mBar$, where it can be further prepared by evaporating molecules on the cold sample or scanned by the STM.

The utilization of an ultra-high vacuum (UHV) environment in STM is a mandatory feature of the experimental setup. Maintaining UHV conditions within the STM chamber

is imperative for contamination control, as very small impurities can disrupt measurements. By eliminating air molecules and contaminants, UHV ensures that both the sample surface and the scanning probe remain uncontaminated. Besides, in a vacuum, there are fewer electron-scattering interactions, resulting in a tunneling current that is both stable and predictable. To effectively reach UHV conditions in the STM chamber, a series of pumps must be assambled. First, a rotary or scroll pump has to create a rough vacuum of $\approx 10^{-4}$mBar, then a turbomolecular pump improves it to $\approx 10^{-8}$mbar, and finally the ion getter pump with a titanium sublimator will bring the UHV conditions $\approx 10^{-10}$mBar.

1.4.2 Cryogenic conditions

Cryogenic temperatures are not mandatory to perform STM but are essential to achieve the most precise measurements. This thesis focuses on low temperature SPM (LT-SPM) that requires cryogenic conditions. Reducing the temperature to cryogenic levels, typically a few degrees over absolute zero, minimizes thermal vibrations and motion at the atomic and molecular scale. This reduction in thermal noise enhances the stability and precision of STM measurements, allowing for the detection of subtle surface features and atomic structures. Additionally, cryogenic conditions are often required to explore specific quantum mechanical phenomena and unique material properties that become evident only at extremely low temperatures. Cryogenic SPM setups incorporate specialized cooling systems, such as nitrogen/helium cryostats (Fig. 1.14). These cooling systems enable the precise control of temperature throughout the experiment, ensuring that the sample and the STM tip remain at the desired cryogenic conditions. The incorporation of helium and nitrogen shields holds paramount significance, especially in the context of experiments requiring cryogenic temperatures. The helium shield, central to cryogenic SPM configurations, serves the fundamental purpose of thermal isolation. Its operation hinges on the use of liquid

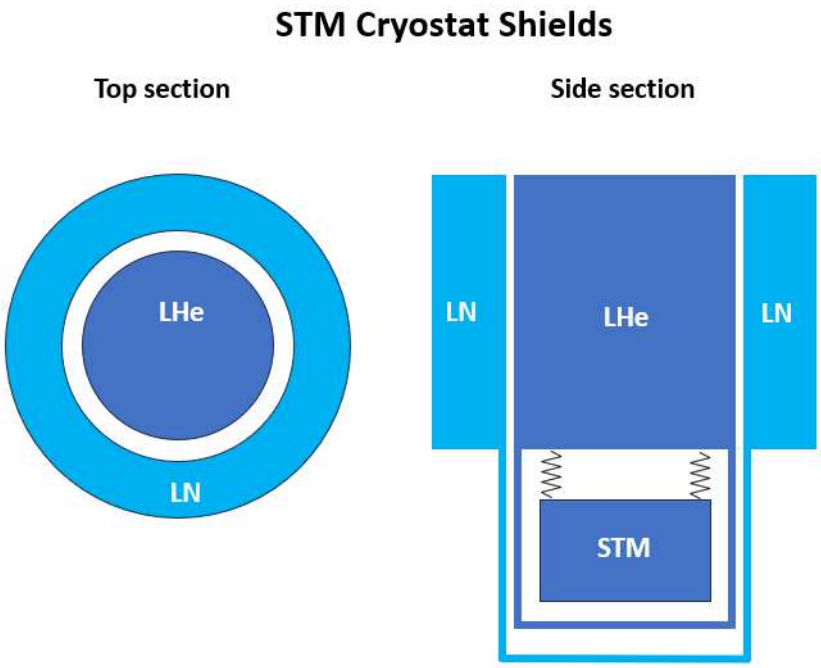

Figure 1.14: SPM Cryostat shiedls. Dark blue: Helium tank, light blue: nitrogen tank. The SPM head is hanging by springs and connected by copper wires to the helium cryostat to ensure insulation and thermal stability at liquid He temperature.

helium. The helium shield is an impervious barrier, protecting the SPM head and the sample from the influence of the external environment with higher temperatures. Nitrogen shields offer an additional layer of temperature control, typically in the vicinity of liquid nitrogen temperatures, approximately 70K. Nitrogen shields aid in mitigating thermal fluctuations and play a vital role in reducing unwanted temperature-related disturbances in the vicinity of the STM apparatus. Finally, the SPM head hangs from the He cryostat to minimize mechanical noise, and is thermally coupled with it by copper wires.

Some atomic systems require even lower temperatures to display their most interesting properties. A Joule-Thomson (JT) stage is a cryogenic device to cool the scanning probe and sample to 1.2K. It operates based on the Joule-Thomson effect, where a gas is allowed to expand adiabatically through a capillary. This expansion causes a drop in temperature,

allowing the JT stage to reach near absolute zero temperatures just above the SPM head. The JT stage is typically integrated into the system. A high-pressure gas, often ^{4}He, is supplied to the stage. The gas is forced through a small orifice or capillary, where it undergoes rapid expansion. As it expands, the gas cools down significantly due to the reduction in pressure. This cold gas is then directed towards the scanning probe and sample, effectively cooling them down to the desired ultra-low temperatures, around 1K or even in the millikelvin regime.

1.4.3 Noise management

The SPM setup is shielded from external disturbances like vibrations, temperature fluctuations, and electromagnetic interference. Such isolation is crucial for maintaining the reproducibility and reliability of the tip-sample distance allowing measurements in the nanoscale. The mechanical stabilization component is achieved through the implementation of a multi-stage damping system: a spring or eddy damping suspension and pneumatic insulators. SPM springs act as a low-pass filter for vibrations with frequencies lower than the SPM's head natural resonant frequency. By decoupling the microscope head from the rest of the equipment, the spring system prevents vibrations or sudden movements in one part of the setup from affecting the scanning probe and the sample being studied. The use of eddy current is also utilized as a low-noise filter mechanism. In this process, the Cu part moves within a magnetic field, and eddy currents generated inside the conductor produce damping forces [2]. Pneumatic legs are employed as a high-pass filter for higher frequencies. These legs consist of air-filled chambers that can absorb mechanical vibrations and suppress mechanical noise, both vertically and horizontally, by over an order of magnitude, particularly for frequencies exceeding 10 Hz. When the STM system experiences vibrations, the air in these chambers compresses, effectively dampening the oscillations and preventing them from affecting the sensitive scanning probe. Furthermore, building vibrations, primarily

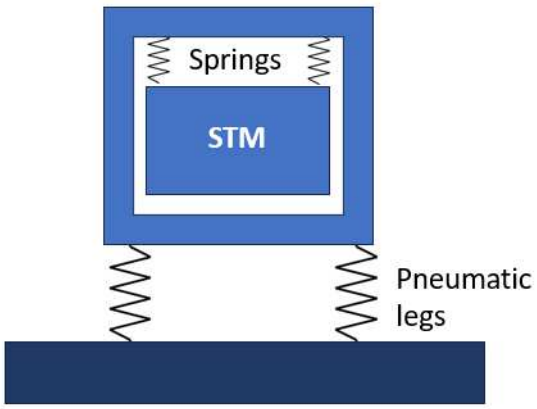

Figure 1.15: Two-stage damping of the SPM chamber. The pneumatic legs filter the high-frequency noise and the springs from where the STM hangs filter the low-frequency noise.

noticeable in the sub-10 Hz frequency range, can stem from various external sources and are less prominent in a building's basement, which is the typical location for most STM.

1.4.4 Piezoelectric components

To achieve the sub-angstrom precision of the SPM motion, piezoelectric components are employed. The tip scans on the x and y directions and approaches/retracts from the sample on the z direction by the action of the AC electric signal that triggers the piezoelectric components. The piezoelectric effect exhibited by certain materials, piezoceramics in the case of the SPM, is characterized by their non-centrally symmetric crystal lattice structure, made of polarized polycrystalline material obtained by powder sintering from crystal ferroelectrics. When subjected to mechanical stress or pressure, these materials undergo atomic rearrangements, causing a disruption in their electric charge distribution and generating an electric voltage across them. Conversely, when an electric field is applied, it induces mechanical deformation or strain in the material. This duality allows piezoelectric materials to convert mechanical energy into electrical energy and vice versa in a very

precise manner. A sudden charge of electric field on the piezo component will build strain that often translates into an extra extension of the device over time until the tension is relaxed, and is called piezoelectric creep. This must be taken into account as it will lead to spurious tip-sample distance changes and must be compensated. The piezo elements require 100-200V to get extended several micrometers. The digital voltage signal coming from the feedback, usually limited to 10V, is not enough for that, so high-voltage amplifiers are mandatory to achieve the desired piezo extension. The bandwidth of this amplifying setup is limited by the resonant frequency of the piezo element.

1.5 Electronic components of the SPM

The tunneling current flowing through the SPM junction is an analog current signal that needs to be treated in order to be electronically transformed into an amplified, noise-free digital DC signal suitable for computer software. Furthermore, besides the information provided by the current and bias signal, the study of the conductance (see section 1.6) requires the utilization of a lock-in amplifier. The electronic components needed for all of these operations play a principal role, and it is mandatory for the user to properly set them up to perform the SPM experiments.

1.5.1 RC Filters

A filter is a simple electronic component to isolate a certain frequency range of an AC voltage signal to avoid electrical noise or unwanted AC components from spikes or step-like features on the DC voltage signal that can be deconvoluted into a sum of sinusoidal waves by Fourier analysis. A filter is generally composed of a capacitor and a resistor, and depending on their configuration, the filter will be low-pass or high-pass [31]. First, let us introduce the voltage divider as a DC circuit that provides an output voltage with a fraction of the amplitude of the input voltage. By Ohm's and Kirchoff's laws, it is straightforward to calculate the input V_i and output V_o voltage from the circuit shown in Fig. 1.16 with the expression $V_o = V_i \frac{R_2}{R_1+R_2}$ [2], it is intuitive to think that depending on the value of R_1 and R_2, so if R_2 is low, more signal will flow through the R_2 branch and decrease V_i:

The same concept will be utilized to make a filter, so the voltage will be divided as a function of several parameters. In an AC circuit with a frequency f, a capacitor C in series with a resistor R will oppose a voltage change and will have an impedance of $Z = R + X = R_1 - i\frac{1}{2\pi fC}$, from here it is easy to follow that Z decreases when f increases, as a result, by swapping R_2 with C in the previous circuit, we obtain a low-pass filter. In

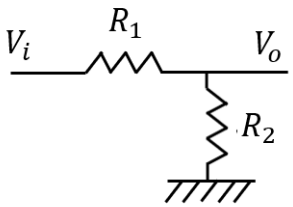

Figure 1.16: Voltage divider. The input voltage V_i can be changed by tuning the resistors R_1 and R_2

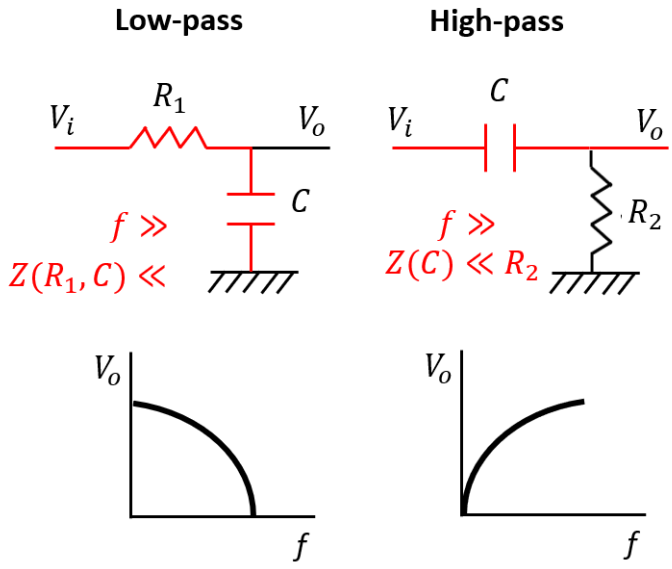

Figure 1.17: RC filters.

this case, V_o will depend on R_1, C, and f. Higher frequencies will allow more signal to go through the capacitor, draining voltage from V_i and decreasing V_o. Low f signals will go through the R_1 branch with little energy losses, ignoring the C as its impedance is high for lower f. The contrary situation will lead to a high-pass filter. By swapping the R_1 with a C, the high f signal will find it easier to travel through C, so a lesser portion of the signal will be lost through R_2 (Fig. 1.17). In the same spirit, one can play with inductors instead of capacitors as they have the inverse frequency response and will oppose a current variation instead of a bias variation.

The proportion of signal loss after the filter corresponds to the gain of the filter $G = V_o/V_i$.

For frequencies far from the cutoff f_c, $G \approx 1 \approx 0db$. When the imaginary part of the impedance (reactance X) becomes equal to R_1, the system reach the $3db$ gain and encounters the cutoff. $f_c = \frac{1}{2\pi R_1 C}$. RC filters have a characteristic time constant (TC), that represents the time for a drop of 36.79% of its original value.

1.5.2 The Femto preamplifier

A Femto preamplifier [32] is an electronic device designed to amplify currents on the order of femtoamperes (10^{-15}A) and also transform the current signal into a bias signal, both of them necessary to perform SPM measurements. To do so, it utilizes operational amplifiers (op-amp) [2] [33]. The main task for an op-amp is to amplify the difference between two input voltages V_1 and V_2 proportionally to a gain constant G, so the output voltage is $V_{out} = G(V_2 - V_1)$. An op-amp will theoretically block current flow between the inputs (very high input impedance) and will offer very little resistance to the current flowing through it (low output impedance). The op-amp is powered by an external power supply. To convert the tunneling current into a bias signal, one could just add a resistor and measure the voltage drop as a function of the current; nevertheless, this operation will affect the weak tunneling current input signal. To avoid conversion losses, an op-amp can be set to convert the current into voltage. If the input tunneling current is connected to the inverting terminal (-) and also connected to the output, the op-amp will act as a feedback loop, and the output will follow the input $V_{in} \approx V_{out}$. With this in mind, one can add a resistor R_f to measure the current and control the gain, assuming that the voltage at the inverting input (-) is a virtual ground with $V = 0$, and the output signal is $V_{out} = -IR_f$. The minus sign comes from the phase inversion of 180° that the inverting input suffers on the op-amp. This way, the relatively weak input current signal can be converted into voltage and amplified minimizing the losses.

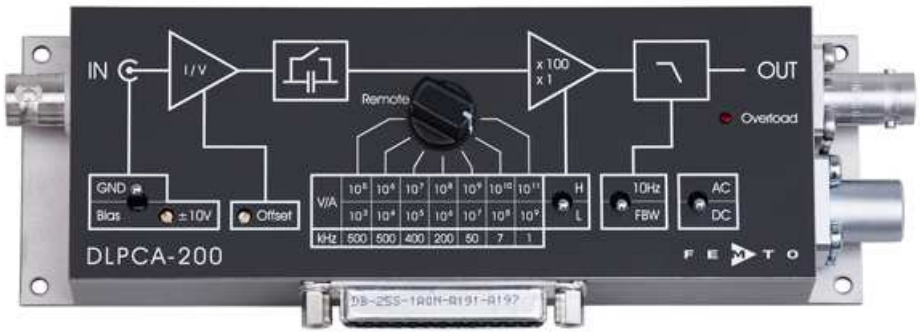

Figure 1.18: Femto DLPCA-200 preamplifier [32].

An ideal op-amp set in this negative feedback configuration will have infinite gain and zero input current, so it will apply any output voltage necessary to keep the inputs equal. In a real situation, the gain is limited to the power supply voltage, and it should be enough to guarantee that the two input voltages (ground and current signal) are similar. When more gain than the one provided by the power supply is required, the op-amp will saturate, offering as output the maximum possible voltage. In these conditions, the op-amp cannot amplify the signal properly. The input signal may have an AC component that must be taken into account setting the amplifier's bandwidth. The tunneling current can be an AC signal after modulating it with a lock-in to perform STS. Besides, while the overall signal may be DC, sharp changes in the signal (peaks, step-like features) can be viewed as a combination of sine waves at various frequencies, and the more abrupt the change, the higher the frequency components present even though the signal itself is a step change in the DC level. To deal with the amplification of AC signals, a capacitor C_{stray} must be added to obtain the current from the complex impedance. This will add another phase shift to the tunneling current signal and also some losses due to the low-pass filter action of the capacitor. To avoid this, the bandwidth of the amplifier (frequency range in which the op-amp can work without losses) must be set accordingly. If ω is the angular frequency of the AC signal, the output voltage will be: [2]

$$V_{out} = \frac{-IR_f}{\sqrt{1 + (2\pi f R_f C_{stray})^2}} \tag{1.9}$$

The frequency at which V_{out} decreases by $1/\sqrt{2}$ is $f_{cut} = 1/(2\pi R_f C_{stray})$. The bandwidth of the op-amp is the frequency range in which the current can be properly amplified without losses from 0 Hz to f_{cut}. The gain is proportional to R_f, and the bandwidth to $1/R_f$. Increasing the amplification implies decreasing the bandwidth of the op-amp. The gain bandwidth of an op-amp is interconnected with its slew rate. The slew rate represents the maximum rate at which the op-amp can respond to a substantial change in the input signal, while the bandwidth denotes the maximum rate of response to minor variations. Both factors play an important role in determining the settling time of a step response and the overall speed of the op-amp.

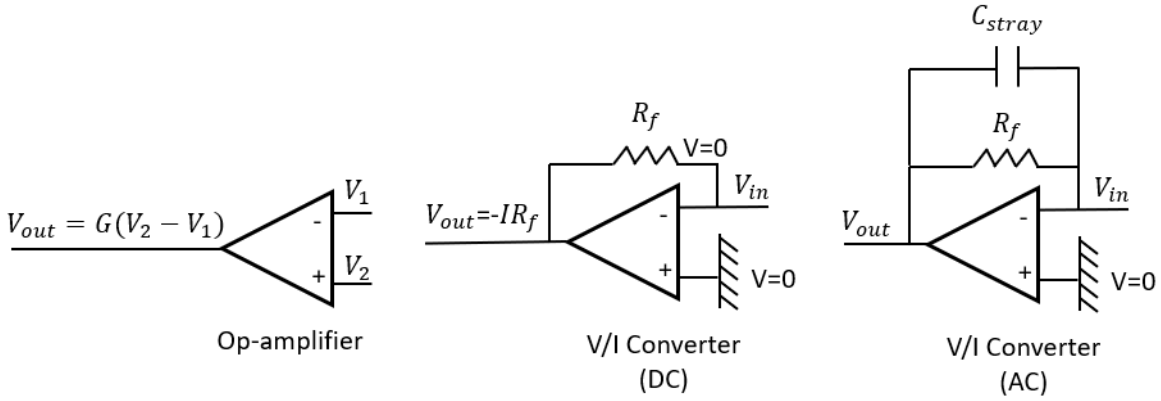

Figure 1.19: Different configurations of an op-amp. Left: voltage amplifier. Center: DC V/I converter, Right: AC V/I converter. The power supply terminals are not drawn.

For typical STM measurements, the amplifier should be capable of handling tunneling currents of 100 nA without saturation. In this case, the DLPCA-200 offers variable transimpedance gain from 10^3 to 10^{11} V/A, which should be set accordingly, with 10^9 V/A being the usual gain as it provides amplification up to 10 nA without compromising the current signal, whose setpoint will usually range between 10-100 pA. If the current goes

above the set gain, the output will saturate offering a constant value of 10 nA, so the gain must be lowered to 10^8 V/A. Any changes in gain will modify the signal's phase (due to the signal inversion and the capacitor), so the lock-in must be autophased again after it.

1.6 Scanning Tunneling Spectroscopy (STS)

1.6.1 STS Working principle

While Bardeen's theory depends on the effect of electronic and geometric properties of the biased junction in the transmission factor T, the Tersoff-Hamann approach [34] assumes the tip to be spherical with a radius r, and $T, \rho_{\text{tip}} \approx$ cte, so the current mainly depends on the sample's properties and the local density of states (LDOS) ρ_s by assuming only s-wave functions for the tip[2][35]. At the limit of low voltage bias and near absolute zero temperatures, we can obtain an approximate expression from equation 1.5:

$$\frac{dI}{dV} \approx \frac{4\pi e^2}{\hbar}\rho_t(0)\rho_s(\epsilon)T(\epsilon, V, d), \tag{1.10}$$

and therefore:

$$\frac{dI}{dV} \propto \rho_s(\epsilon). \tag{1.11}$$

Here, ρ_s corresponds to the local density of states (LDOS) of the sample near the Fermi energy. This differential expression is known as conductance. It relates the tunneling current and the applied bias and is proportional to the local density of states of the sample, which is an intrinsic physical property of the object of study and provides information about its electronic structure. By performing scanning tunneling spectroscopy (STS), one can probe and map the LDOS at a certain energy with a high lateral resolution by differentiating the current with respect to a specific bias voltage (Fig. 1.20).

The energy resolution in STS is set by the all the contributions to the tunneling current at different energies. In the case of small voltages, the energy resolution depends on two main effects: thermal broadening and the lock-in modulation amplitude (see Attachments). The energy resolution is limited due to thermal broadening as the higher the temperature,

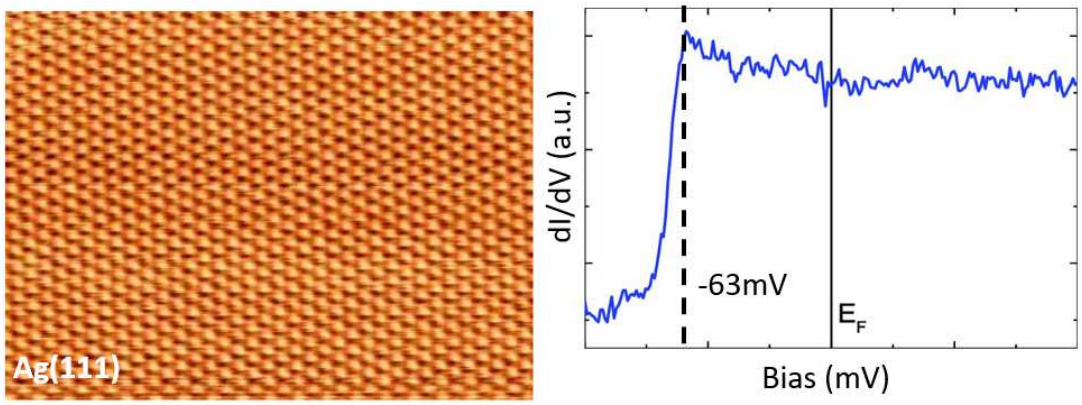

Figure 1.20: Left: Ag(111) STM image at $T = 50$ K, $V = -20$ mV, and a setpoint current $I = 1$ nA. The size is 9.5×7 nm. Right: The surface state of a Ag(111) terrace at -63 meV. The probing parameters were $T = 5$ K, $V = -100$ mV, $I = 1$ nA, and $V_{\text{mod}} = 5$ mV. [35]

the larger the broadening, and the worse the energy resolution. Abandoning the assumption we made for equation 1.5, where the Fermi distribution was approximated as a step function, we can obtain the dependence of the conductance with the temperature.

$$\frac{dI}{dV} \propto \int_{-\infty}^{\infty} \frac{\partial f(\epsilon - V)}{\partial V} \rho_s(\epsilon) d\epsilon \tag{1.12}$$

Adding this thermal broadening to the average broadening caused by the lock-in amplitude, which will oscillate in a range of $2V_{mod}$ the energy resolution (in meV) of the STS can be estimated using this expression[2]:

$$\Delta E = \sqrt{(2eV_{mod})^2 + (0.28T)^2} \tag{1.13}$$

Here, T is the temperature in Kelvin, e is the electron charge unit in meV ($e = 1$ meV), and V_{mod} is the lock-in modulation amplitude in mV. The bias offset between the tip and the sample may also have an effect on the Local Density of States (LDOS) probed, depending on its polarity, resulting in an asymmetry in the dI/dV signal. When using positive bias, electrons mainly tunnel from the last occupied state of the tip to the empty states with

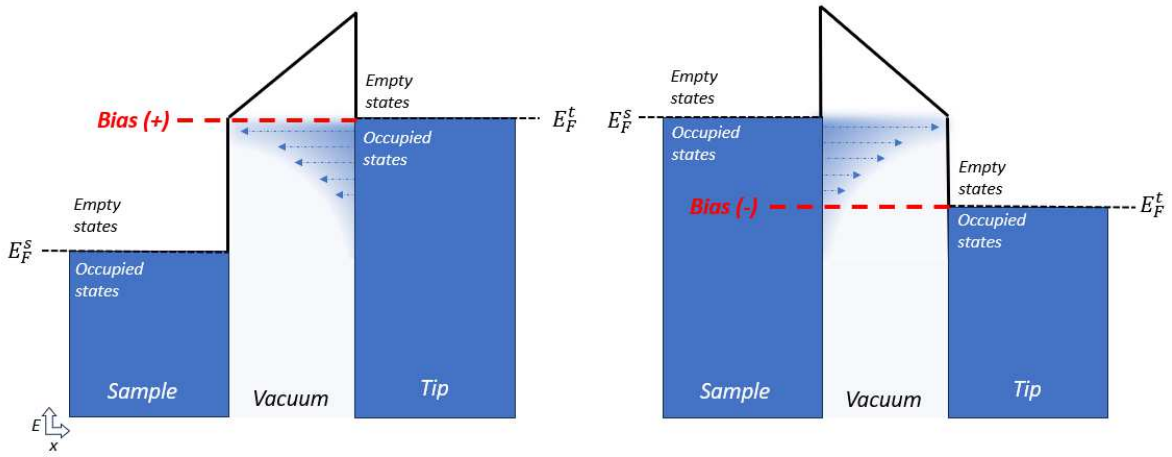

Figure 1.21: Asymmetry in the STS spectra.

similar energy on the sample. The also-accessible states contribute less to the current, providing accurate information about the conductance at the selected bias. Conversely, when using negative bias, electrons tunnel from the last occupied state of the sample to the empty states of the tip. In this case, the states that contribute the most to the tunneling current are not aligned with the selected energy but with the Fermi energy of the tip. This leads to a small contribution of the states at the desired bias and a significant contribution of the states above it, causing an increase in conductance that enhances the signal on the negative side and misleads the STS information (Fig. 1.21).

STS spectra are typically acquired in constant-height mode over a fixed position or area (dI/dV mapping) at a specific tip-sample distance. The dI/dV is recorded by incrementally varying the bias voltage to affect the current. The measured signal results from the differential variation of the current channel with respect to the bias. While this signal can be acquired by numerically differentiating the current, a lock-in amplifier is often used for greater accuracy[34][36] (see Attachments).

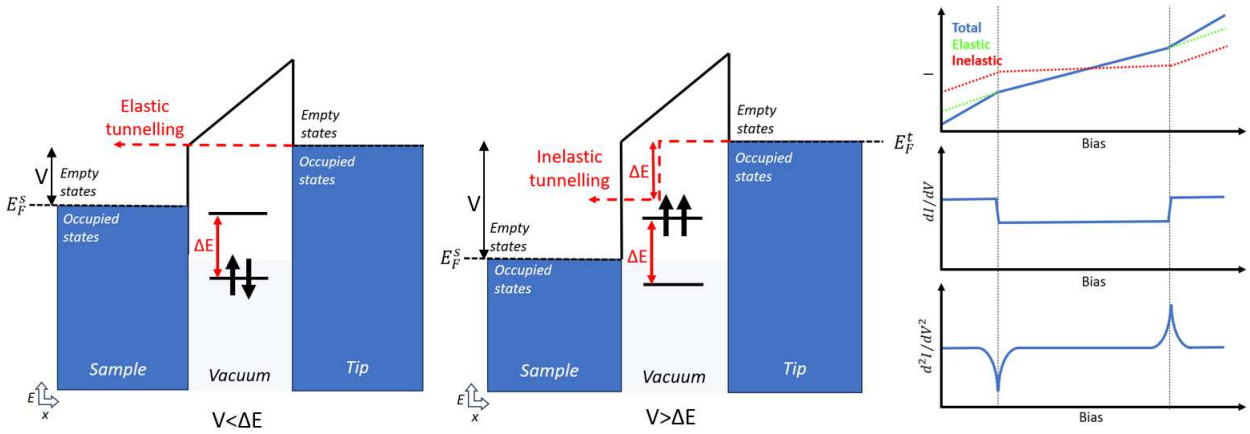

Figure 1.22: Representation of the inelastic tunneling from the biased STM junction between the tip and a two-level magnetic molecule on the sample substrate. Left: elastic tunneling. The electrons coming from the tip tunnel elastically as they do not have enough energy to excite the spin-flip from $m_s = 0$ to $m_s = \pm 1$ states of the molecule ($\Delta E > V$). Center: On the right, current, dI/dV, and d^2I/dV^2 plots as a function of the bias. The total current is composed of inelastic and elastic contributions. The spin-flip creates a dip in the dI/dV that translates to peaks in the d^2I/dV^2 at the energies of the spin-flip excitation.

1.6.2 Inelastic Electron Tunneling Spectroscopy (IETS)

Inelastic tunneling occurs when an electron loses some kinetic energy during the tunneling process, opening a new tunneling channel [2][37]. With this new pathway, the dI/dV increases due to a higher density of states available for tunneling. The current will have two contributions: elastic and inelastic, each with different percentages. This event manifests as a dip in the dI/dV. The electron can lose energy by transforming its kinetic energy into molecular vibrations, with a minimum energy amount of $\hbar\omega$. Another type of inelastic process is the spin-flip event [38] (Fig. 1.22). In this case, the electron can reach a state with a different spin elastically, which is not accessible by inelastic tunneling. This increases the overall density of states and the step-height of the spin excitation. To conserve the total spin of the system, the electron changes its spin during the tunneling event, losing some kinetic energy. The detection limit involves transitions with $\Delta m_s = 0, \pm 1$.

1.6.3 The Lock-In amplifier

A lock-in amplifier utilizes phase-sensitive detection to isolate a component of a signal at a specific reference frequency and phase. It fundamentally operates on the principle of orthogonality among sinusoidal functions. In particular, when a sinusoidal function is multiplied by another sinusoidal function with a different frequency and then integrated over a time significantly longer than the period of these two functions, the result is effectively zero. However, if the frequencies are in phase, the average value equals half of the product of their amplitudes. By taking the input signal and multiplying it with a reference sinusoidal signal (which can originate from either the internal oscillator or an external source) and integrating over a specific time (from milliseconds to several seconds), the output signal becomes a DC signal. The process attenuates any component of the signal that doesn't share the same frequency as the reference signal and the out-of-phase part of the signal and add an extra phase ϕ to the in-phase component which is the main contributor to the amplitude on the lock-in signal. This makes the lock-in amplifier phase-sensitive[39]. If the integration time is large enough, the output V_{lockin} is:

$$V_{lockin} = \frac{1}{2} V_{input} cos(\phi) \tag{1.14}$$

Modern lock-in amplifiers add a 90^o phase shift (two-phase lock-in[40]) to an extra output signal in order to remove the phase dependency. The procedure is the same as for the original lock-in, but with two output components, X, Y. This two magnitudes represent the output signal as a vector relative to the reference:

$$X = \frac{1}{2} V_{input} cos(\phi) \quad Y = \frac{1}{2} V_{input} sin(\phi), \tag{1.15}$$

$$R = \sqrt{X^2 + Y^2} \quad \phi = arctan(X/Y). \tag{1.16}$$

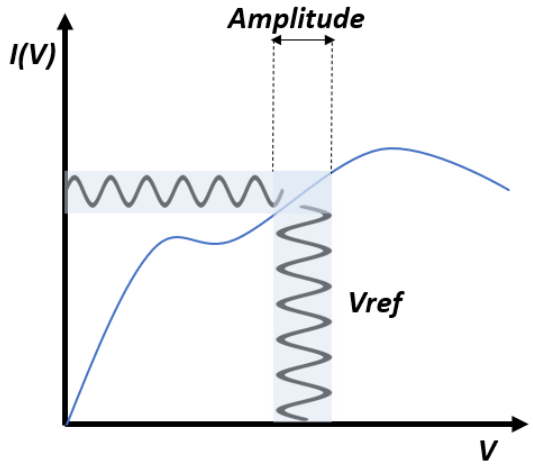

Figure 1.23: Principle of the lock-in technique. The current is influence by a bias modulation from a reference AC signal to extract the conductance.

The magnitude R corresponds with the output signal and ϕ is the phase shift between the modulated signal and the reference signal, as before. The magnitude ϕ will dictate how much of X and Y compose the final output signal. A phase closer to X will originate an output signal with more weight on X (and subsequently the components of the modulated signal whose phase is also closer to X) and less from Y, and viceversa.(Fig. 1.24). Most of modern lock-in amplifiers have an autophase command that will sweep ϕ to find the phase that provides the most amplitude.

The general principle to obtain the derivative of a signal using a lock-in consist on adding an AC modulation reference signal $V_{ref}(t) = V_{mod}cos(f_0t + \varphi)$ to the STM DC bias signal $V(t)$ to modulate as well the tunneling current $I(V) = I(V_{DC}) + I(V_{ref})$ obtaining the dI/dV[41]. By making $V_{mod} << |V|$ so the oscillation becomes a perturbation around V_{DC}, a Taylor expansion can be performed so the modulated AC current signal can be approximate to:

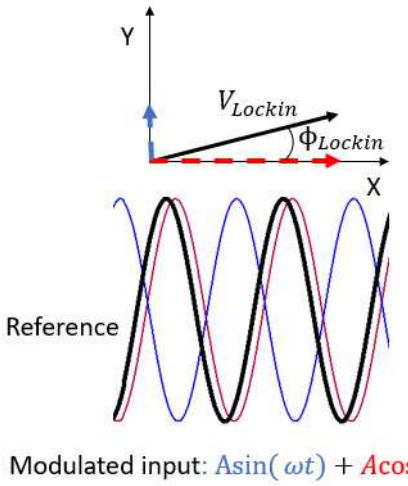

Figure 1.24: The output signal depends on the phase of the reference signal respect to the input signal. As the input signal will have several out of phase components, the lock-in will be more sensitive to the ones closer to the reference. To avoid this phase sensitivity, the input signal is modulated and split in two signals X, Y separated by a 90^o phase shift. The input signal components contribution is weighted by controlling the lock-in phase ϕ. $|V_{lockin}| = R$

$$I(t) = \underbrace{I(V_{DC})}_{\text{DC component}} + \underbrace{\underbrace{\frac{dI(V)}{dV} V_{mod} A_1 cos(f_0 t + \varphi)}_{\text{First harmonic}} + \underbrace{\frac{d^2 I(V)}{dV^2} V_{mod}^2 A_2 cos(2 f_0 t + \varphi)}_{\text{Second harmonic}}}_{\text{AC component}}. \quad (1.17)$$

The lock-in amplifier will multiply $I(t)$ by the reference signal V_{ref}, that will add up another phase therm ϕ:

$$I_{lockin}(V) = I(t) * V_{mod} cos(f_0 t + \phi). \quad (1.18)$$

From here we can observe that the lock-in signal after demodulation is proportional to the modulation amplitude V_{mod} and the dI/dV (fig. 1.23). The smaller V_{mod} is, the better resolution the signal has, as it oscillates in a smaller range and averages the signal between a narrower ΔV, nevertheless, it will also increase the noise and slow down the

acquisition, so in order to obtain the best resolution one has to find a compromise between integration time and the lock-in amplitude. Eq. 1.17 also provides information about the second harmonics, which are linked to the derivative of the conductance d^2I/dV^2. By controlling the phase ϕ is possible to maximize the output lock-in signal. To access the second harmonics, the frequency has to be $2f$. In general, following the same principle nV_{mod} amplitude at nf is proportional to d^nI/dV^n [2].

In general, if one desires to measure a signal that is closely phase shifted to 0^o or 90^o respect to the reference signal phase ϕ, is better to phase the lock-in to read 100% of the signal in one channel X and 0% in the other channel Y (or viceversa) to easily spot signal losses[40]. Under applied bias, the STM junction acts as a capacitor, and the AC modulated input signal gets another contribution proportional to the capacity of the junction V_C that is 90^o shifted respect of the reference signal (Fig. 1.25). The tunneling current will have then another out of phase AC component $I(V) = I(V_{DC}) + I(V_{ref})$. The AC contributions can be assigned to the X, Y channels of the lock-in so one can select their weight on the output signal by adjusting the phase ϕ. To isolate the dI/dV part of the signal from the capacitance when performing STS, the tip must be retracted from the sample to avoid any tunneling current contribution. The signal will come from the capacitance component only, so the lock-in phase can be set to maximize this signal and then manually rotated by 90^o to obtain the pure dI/dV (Fig. 1.26). The d^2I/dI^2 has its maxima out of any phase described before, so the lock-in phase must be set in contact at the tunneling bias that offers the most signal (R) and optimized by the lock-in itself by auto-phasing. For example, dI/dV measured at different tip-sample distances d will provide a signal that weakens as the tip retracts, while keeping a strong contribution from the capacitance. In this case, as for measuring the first derivative, is better to use a single channel 90^o shifted respect to the conductance, instead of the magnitude R, that adds up all the different phased components of the signal regardless the relative phase ϕ. The capacitance component can

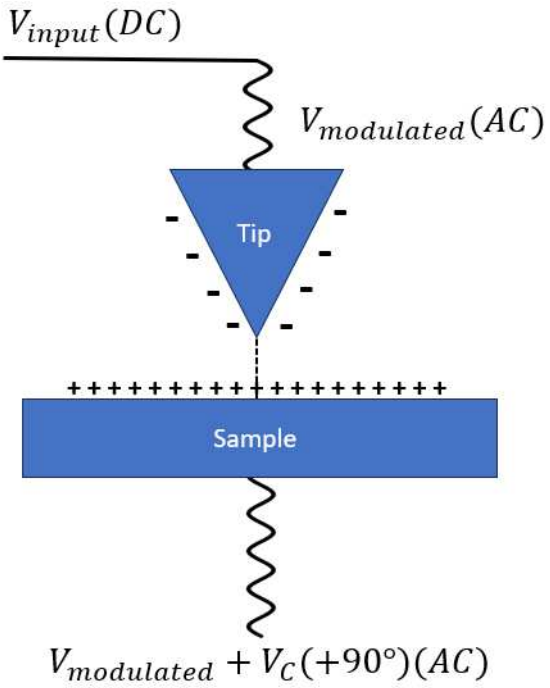

Figure 1.25: Biased STM junction acting as a capacitor and adding a capacitance term V_C with a 90^o phase shift to the modulated input signal $V_{modulated}$.

be useful to obtain a reference value when coarse approaching the tip. By setting a large V_{mod} amplitude (e.g. 500 mV) and a moderate frequency (e.g. 531Hz) the lock-in will assign one channel from X, Y to match its phase, and the readout from this channel will display a value related to the capacitance measured between the sensor and the sample. This value will increase as the tip gets closer to the sample, and a reference value can be found to stop the coarse approach as close as possible before starting the auto-approach function. This method can only be performed when the sensor has enough metallic surface to get charged by the modulated bias. The protective metallic cup from the Kolibri sensor allows to measure capacitance, while the narrow cantilever from the QPlus sensor has not enough surface to drive this phenomenon. More details about the lock-in setup can be found in the Attachments.

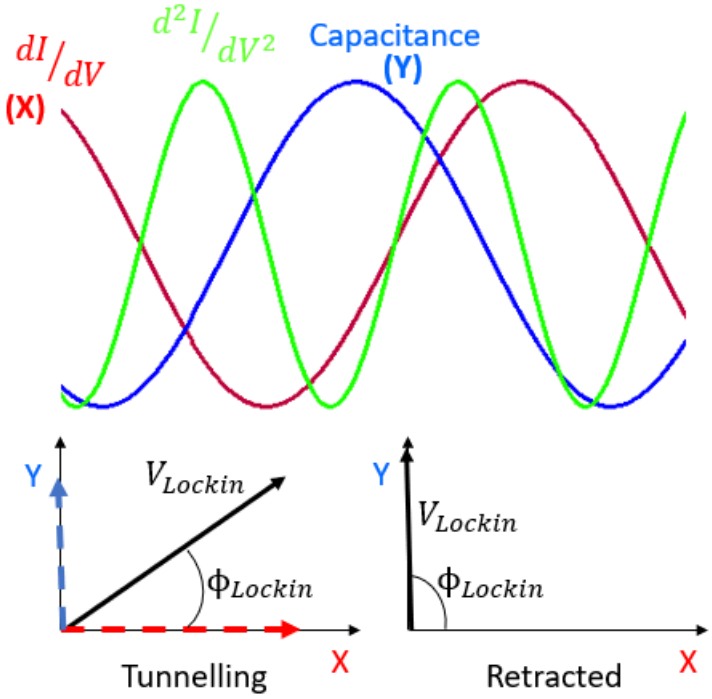

Figure 1.26: The first (red) and second (blue) derivatives of the current and the capacitance signal (green) have different phases. The dI/dV and the capacitance signal can be isolated form each other by retracting the tip as they are shifted by 90^o. The second derivative must be set in contact to maximize its value, as it maxima does not share this phase shift.

Chapter 2

Metallocenes as STM magnetic sensors

This chapter is devoted to the metallocenes, with a focus on nickelocene and a presentation of some properties of cobaltocene. After their introduction, the chapter reviews the state of the art in previous works that have utilized nickelocene as a magnetic sensor. Furthermore, these studies are further analyzed with the theoretical tools described in Section 2.2 (Theoretical Framework), developed by Diego Soler Polo and Manish Kumar.

2.1 The Nickelocene molecule

The metallocenes [42, 43], also known as metal-sandwich complexes, have held significant importance since the synthesis of ferrocene ($FeCp_2$) in 1951 by Keally and Paulson, followed by its structural characterization by Wilkinson and Fischer, which led to the Nobel Prize in 1973. Metallocenes are compounds composed of two cyclopentadienyl anions ($C_5H_5^-$ or Cp) and a transition metal (ranging from Ti to Ni) in a +2 oxidation state, forming a sandwich structure. They exhibit two isoenergetic configurations: staggered and eclipsed, with D_{5d} and D_{5h} symmetry, respectively [44]. The magnetic moment in metallocenes arises from the oxidation state of the metal center, localized in the $3d$ shell after sharing two $4s$ electrons

with the Cp rings. The molecular orbital diagram of ferrocene (Fig. 2.1) illustrates the subsequent filling of orbitals between a'_{1g} and e^*_{1g} orbitals for other metallocene molecules.

This thesis focuses on nickelocene, a metallocene with a Ni atom at its core. Despite its 20 electrons, violating the qualitative $18e^-$ rule for metal complex stability, $NiCp_2$ exhibits remarkable magnetic robustness. The energy gap between the ground state a'_{1g} and the excited state e_{2u} is comparatively higher than in other metallocenes with different metallic centers, preventing unpaired electrons from being promoted to higher energy orbitals. This makes nickelocene an excellent candidate for deposition on various substrates and STM-tip manipulation while preserving its magnetic stability and properties from the gas phase [45]. The unpaired electrons on the e^*_{1g} orbitals, separated by Pauli repulsion, provide a magnetic moment of $2\mu_B$ ($S = 1$), which remains perfectly isolated. This allows for the study of nickelocene's singlet and triplet states, which are closer in energy than the higher spin configurations. The $S = 1$ nickelocene energy diagram at low energies can be rationalized by considering the singlet-triplet degeneracy-breaking by the crystal field [27, 46, 47], along with further zero-field splitting between the $m_s = 0$ (in-plane magnetization) and $m_s = \pm 1$ (out-of-plane magnetization) states due to the characteristic magnetic anisotropy of nickelocene. These high-spin states can be further separated by applying a magnetic field parallel to nickelocene's long axis to induce Zeeman splitting or by bringing another molecule into proximity to exchange-couple with nickelocene's unpaired electrons (Fig. 2.2).

STM images of single atoms probed with a nickelocene tip [48] and DFT calculations modeling the functionalized tip [49] agree on assigning a 15^o tilt to the nickelocene with respect to the z-axis perpendicular to the surface. It is worth mentioning that other metallocenes, such as ferrocene ($FeCp_2$) [50–52] or cobaltocene ($CoCp_2$), have also found use in STM. The latter, in particular, is a $S = 1/2$ molecule exhibiting a characteristic Kondo feature in its Inelastic Electron Tunneling Spectroscopy (IETS) and has been utilized as an STM spin sensor [53].

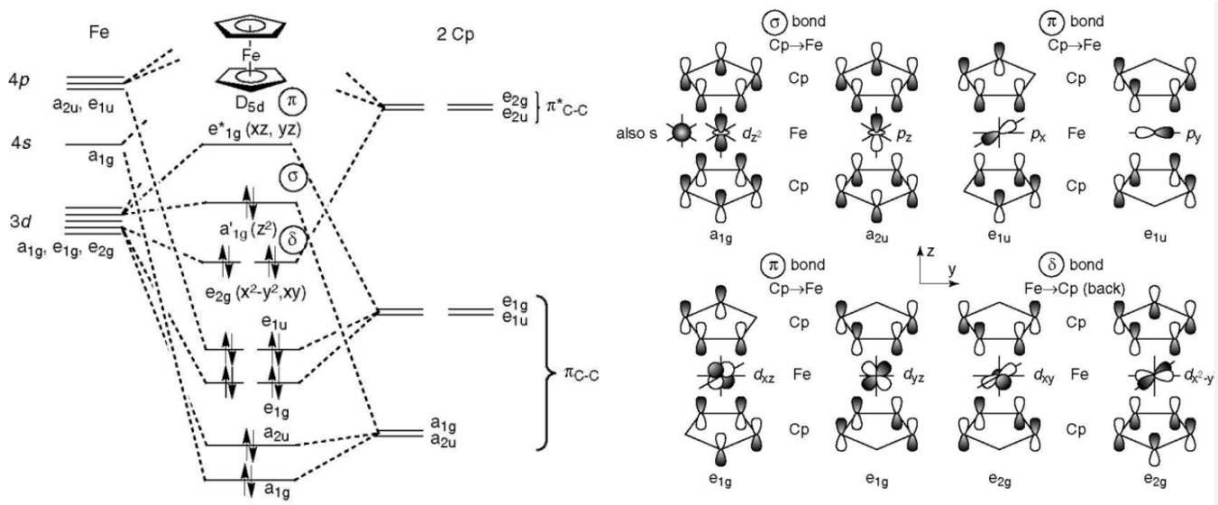

Figure 2.1: Molecular orbital diagram for ferrocene (D_{5d})[44].

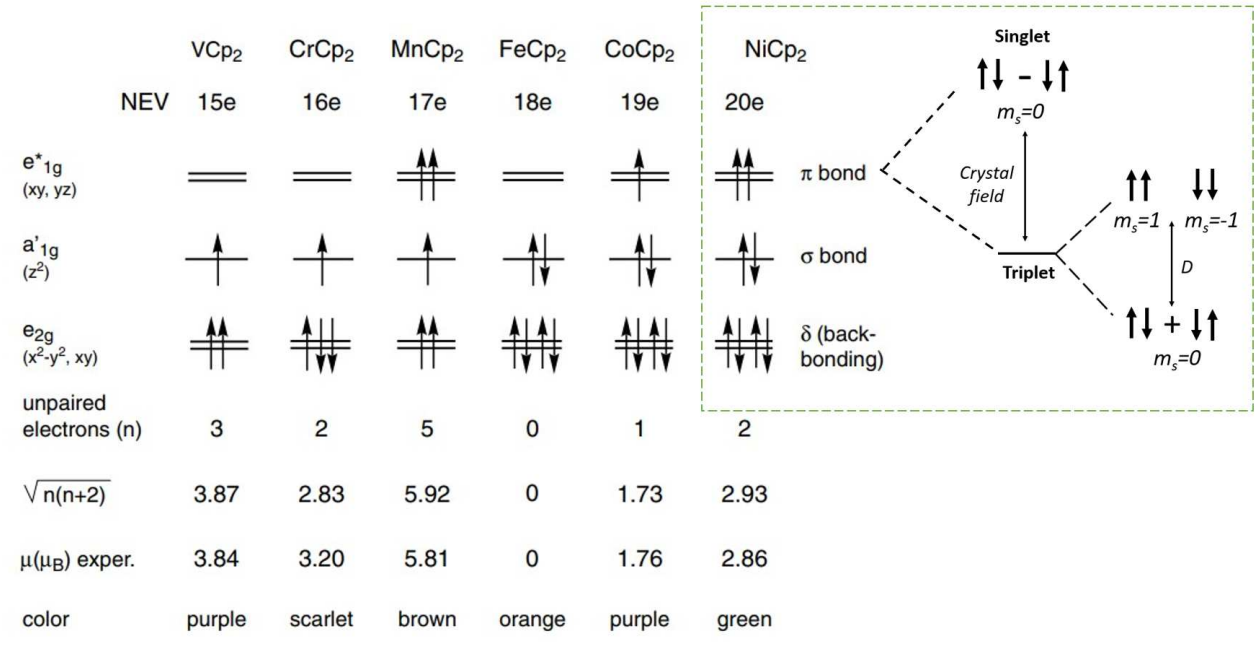

Figure 2.2: Electronic and magnetic properties of the different metallocenes[44]. On the right, nickelocene's energy diagram ($S = 1$). The singlet and triplet state are separated by the crystal field, and the magnetic anisotropy D causes a zero field splitting between the triplet $m_{Nc} = 0$ and $m_{Nc} = \pm 1$.

2.1.1 STM characterization of the Nickelocene

The nickelocene has been extensively studied by STM to unveil its chemical and electronic properties on a metallic substrate at low temperatures [46, 48, 54–58]. To understand the chemisorption of nickelocene after deposition in Ultra-High Vacuum (UHV) and cryogenic temperatures, Bachellier *et.al.* [55] deposited nickelocene in UHV on a Cu(100) surface at 4.4K to find isolated molecules as well as ordered self-assembly islands creating a submonolayer on top of the crystal. This result agrees with previous experiments on the less reactive Ag(100)[59]. They observed the ability to desorb or decompose $NiCp_2$ after 230K annealing. The existence of single nickelocene molecules suggests that it is more surface-reactive than ferrocene, as $FeCp_2$ exclusively physisorbs by van der Waals interaction in self-assembly conglomerates under similar conditions[51].

STM images of an isolated nickelocene on a metallic surface (fig. 2.4) show a ring-like shape in constant current contrast. This implies that $NiCp_2$ is adsorbed in a standing configuration with a Cp ring bonded to the hollow site and the long axis perpendicular to the surface. The apparent STM height measured by Ormaza *et.al.* with the STM at 20 mV and 5 pA current setpoint are 3.5 Å. A more accurate height measurement can be performed by means of nc-AFM with a functionalized tip. We took advantage of the Kolibri STM/AFM tip to measure the adsorbed height of a nickelocene on an Au(111) sample. It was obtained by functionalizing the tip with another nickelocene, pressing it against the target, and recording the frequency shift from the AFM as the tip retracts (Z-spectroscopy Fig. 2.3), yielding an 8.1 Å height difference between Au(111) and the adsorbed nickelocene Z-curve's Gaussian-fitted minima, which delimits the beginning of the repulsion regime, as described by Gross *et.al.* [18].

The nickelocene showcases remarkable endurance when pressing/retracting it from the surface or on top of other molecules, preserving its structure and adsorption configuration on the tip even 200 pm past the Z-spectroscopy minima. This allows obtaining nc-AFM

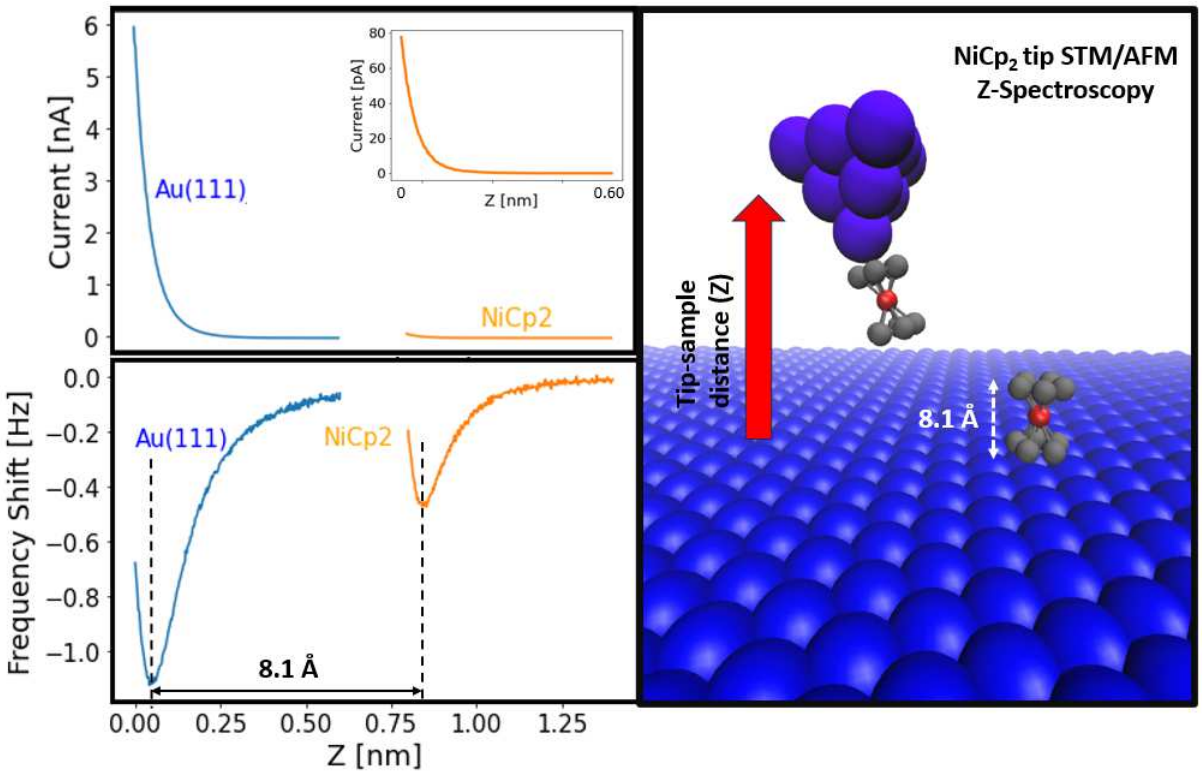

Figure 2.3: STM/AFM Z-spectroscopy of a $NiCp_2$ on Au(111) measured with a nickelocene-functionalized tip at 10 mV. The blue curve corresponds to the measurement on Au(111), pressing the $NiCp_2$ tip 50 pm past the minima and retracting the tip 600 pm, recording the frequency shift and current. The orange curve corresponds to the same procedure performed on top of the adsorbed nickelocene. Top: Current recorded while lifting the tip. The current rises substantially faster when measuring on bare Au(111). Inset: Zoom to resolve the rise of the current on top of the nickelocene. Bottom: Frequency shift from the AFM. After fitting the curves to obtain their minima, the height difference is 8.1 Å. Right: Representation of a nickelocene tip lift performing a Z-spectroscopy on Au(111) and on another nickelocene. Blue=Au, Black=C, Red=nickel.

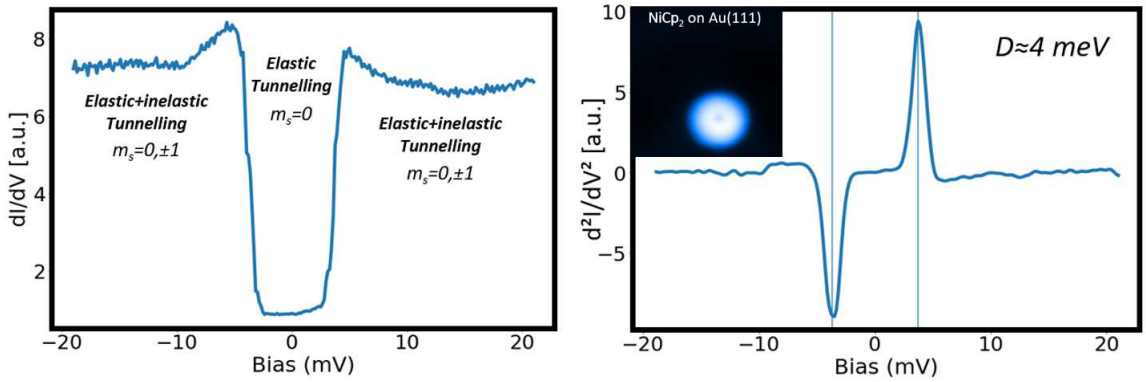

Figure 2.4: IETS of an STM functionalized nickelocene tip on Au(111) taken at 1.2K with a 0.5mV lock-in amplitude. Left: dI/dV spectrum showing a $\sim$ 750% increment of conductance between the elastic ($ms = 0$) and the inelastic ($ms = \pm 1$) region. Right: d^2I/dV^2 spectrum. The peaks show the energy of the spin-flip step feature at ± 4 meV. Inset: 5 x 5 nm^2 STM constant current image of a nickelocene on an Au(111) substrate taken at 100 mV 10 pA.

high-resolution images to atomically resolve molecular structures while simultaneously recording Scanning Tunneling Microscopy (STM) images or dI/dV maps. For these last two techniques, the bias must be set, considering the exponential rise of the current.

As depicted in Fig. 2.3, the current reaches almost 6 nA when measuring on top of bare Au(111) and just 80 pA on top of the less conductive adsorbed nickelocene when approaching/retracting the same Z distance at 10 mV. Further pressing onto the surface can lead to instability or rearrangements of the nickelocene on the tip, compromising the reproducibility and hysteric behavior of the Z-spectroscopy, as shown by an asymmetry in the retract/approach curves. In this unstable regime, the nickelocene can even change its spin state, as reported by Ormaza *et. al.*[45], where a transition from $S = 1$ to $S = 1/2$ is described as the nickelocene is pressed 500 pm onto Cu(100).

The nickelocene has been extensively studied by STM to unveil its chemical and electronic properties on a metallic substrate at low temperatures [46, 48, 54–58]. To understand the chemisorption of the nickelocene after deposition in UHV and cryogenic temperatures, Bachellier *et.al.* [55] deposited nickelocene in UHV on a Cu(100) surface at 4.4 K to find

isolated molecules as well as ordered self-assembly islands creating a submonolayer on top of the crystal, agreeing with previous experiments on the less reactive Ag(100) [59]. They were able to desorb or decompose the $NiCp_2$ after 230 K annealing.

The existence of single nickelocene molecules suggests that it is more surface-reactive than ferrocene, as $FeCp_2$ exclusively physisorbs by van der Waals interaction in self-assembly conglomerates under similar conditions [51]. STM images of an isolated nickelocene on a metallic surface show a ring-like shape in the constant current contrast. This implies that the $NiCp_2$ is adsorbed in a standing configuration with a Cp ring bonded to the hollow site and the long axis perpendicular to the surface. The apparent STM height measured by Ormaza *et.al.* with the STM at 20 mV and 5 pA current setpoint is 3.5 Å.

A more accurate height measurement can be performed by means of the AFM with a passivated tip. We took advantage of the Kolibri STM/AFM tip to measure the adsorbed height of a nickelocene on an Au(111) sample. It was obtained by functionalizing the tip with another nickelocene, pressing it against the target, and recording the frequency shift from the AFM as the tip retracts (Z-spectroscopy Fig. 2.3), yielding an 8.1 Å height difference between the Au(111) and the adsorbed nickelocene Z-curve's Gaussian-fitted minima, which delimits the beginning of the repulsion regime, as described by Gross *et.al.* [18].

The nickelocene showcases remarkable endurance when pressing/retracting it from the surface or on top of other molecules, preserving its structure and adsorption configuration on the tip even 200 pm past the Z-spectroscopy minima. This allows tracking the forces experienced in an approach-retract event and obtaining nc-AFM high-resolution images to atomically resolve molecular structures while simultaneously recording STM images or dI/dV maps. For these last two techniques, the bias must be set, considering the exponential rise of the current. As depicted in Fig. 2.3, the current reaches almost 6 nA when measuring on top of the bare Au(111) and just 80 pA on top of the less conductive

adsorbed nickelocene when approaching/retracting the same Z distance at 10 mV. Further pressing onto the surface can lead to instability or rearrangements of the nickelocene on the tip, compromising the reproducibility and hysteric behavior of the Z-spectroscopy, as shown by an asymmetry in the retract/approach curves. In this unstable regime, the nickelocene can even change its spin state, as reported by Ormaza *et. al.* [45], where a transition from $S = 1$ to $S = 1/2$ is described as the nickelocene is pressed 500 pm onto Cu(100).

The spin states of the nickelocene on Cu(100) were first characterized utilizing IETS and X-ray magnetic circular dichroism (XMCD)[60] by Ormaza *et. al.*[45] (Fig. 2.4). In this work, a single nickelocene adsorbed in a Cu(100) hollow site in eclipse configuration was measured by positioning the STM tip on top of the molecule. IETS yields a step with a conductance increment of five times the dI/dV value around 0 V at 3.2 meV. After discarding this feature to be a vibrational state [59], it was categorized as a spin-flip event from the $S = 1 \quad m_s = 0$ ground state to the degenerated $m_s = \pm 1$ excited states of the nickelocene. This IETS spectrum is a direct measurement of its positive magnetic anisotropy energy ($D \approx 3.2meV$) as the in-plane anisotropy E is negligible by symmetry[61] (see Theoretical Framework). This result is in agreement with their XMCD data. The D value can slightly vary between ∼3-4 meV depending on the tip conformation, being 5 meV the computed value for a nickelocene in the gas phase[62]. This result also confirms the magnetic robustness of the nickelocene as the spin remains $S = 1$ from the gas phase to the adsorbed state. The measurements were repeated with the nickelocene attached to the tip (tip functionalization). While the D remained similar, the increment in IETS conductance was nine times the value around 0 V, comparably higher than the previous non-functionalized case. This result agrees with our IETS spectra obtained after measuring in Au(111) with a nickelocene functionalized tip (Fig. 2.4).

Single nickelocene molecules deposited on a <10 K metal monocrystal is an instructive system to understand how the tunneling process works when using a nickelocene tip. The

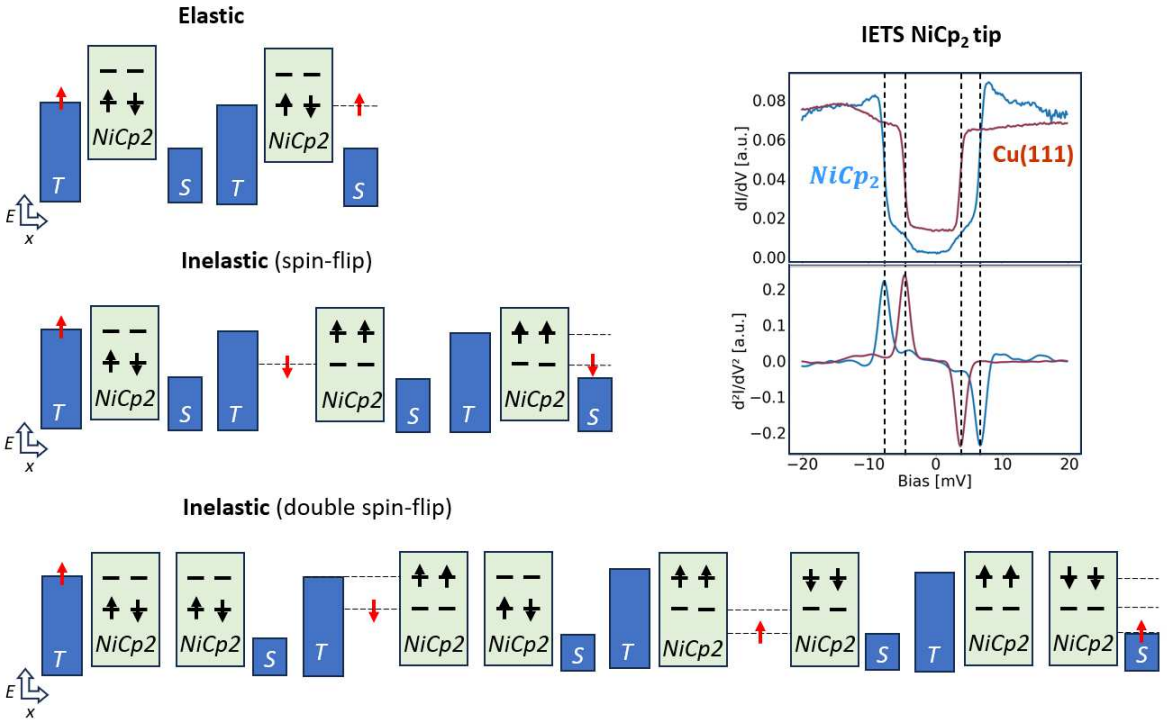

Figure 2.5: Top: elastic tunneling without nickelocene interaction. The electrons depart and arrive with the same energy and spin orientation as the energy. Center: inelastic tunneling. The tunneling electrons scatter with the nickelocene's $m_s + 0$ state electrons and briefly couple by exchange interaction. During this scattering event, the incoming electron loses some energy and flips its spin to satisfy the lower energy configuration from the exchange coupling. This energy will promote the nickelocene to its high spin states $m_s = \pm 1$. The electron arrives at the sample with less energy (exactly the amount required for the spin-flip $D_{Nc} m_s^2$). Bottom: double inelastic spin-flip where the electron undergoes two consecutive inelastic transitions spending two times the spin-flip required energy to excite two $NiCp_2$ to the high spin states. Right: IETS of a nickelocene tip on Cu(111) and on another nickelocene. While the spectrum on bare Cu(111) only shows one dip corresponding to the spin excitation, the spectrum taken over another nickelocene has two steps caused by the double spin-flip. The d^2I/dV^2 shows four peaks separated by 4 meV corresponding to the consecutive excitation.

experiment consists of measuring a nickelocene adsorbed on the metal surface with a $NiCp_2$ functionalized tip. The IETS curves from Fig. 2.5 show the dI/dV and d^2I/dV^2 spectra of a nickelocene tip on Cu(111) and on a nickelocene adsorbed on the surface. From this experiment, along the dI/dV steps at ∼4 meV, another set of steps emerges at ∼8 meV, identified as a double spin-flip, reproducing the results from Ormaza *et.al*[56] on Cu(100) and from Czap *et.al.*[49] on Ag(110). The rationalization goes as follows: a tunneling electron can inelastically excite one molecule (tip or sample nickelocene) and pass by the other without spin-flipping again (first energy step), or undergo a double spin-flip (second energy step) if it has enough energy to excite both molecules to the $ms = \pm 1$ states. Both spin-flip events are a priori isolated, and no further magnetic effects (exchange-coupling, etc.) were described, as the energy of the first step is approximately double the second.

Another STM experiment to test the nickelocene functionalized tip magnetic properties consists of performing IETS with it on a metal substrate under a magnetic field perpendicular to the sample (B_z) to induce a Zeeman splitting of the d^2I/dV^2 peaks. However, our built-in magnet only provides a maximum field of B_z=3 T, meaning 0.7 meV peak-to-peak splitting ($E_{\text{split}} = 2g\mu_B S_{\text{Nc}} B_z$). As the experiments are usually conducted at $T = 1.2$ K and 0.5 mV lock-in amplitude of modulation, the STS broadening in our experiments is 1.3 meV2.2, which does not allow us to resolve the peak splitting on the IETS. The picture completely changes when the magnetic field is strong enough, and the temperature is below 1 K to generate noticeable splitting, as demonstrated by Czap *et.al*[49]. This experiment was conducted on Ag(110) at 0.6 K and

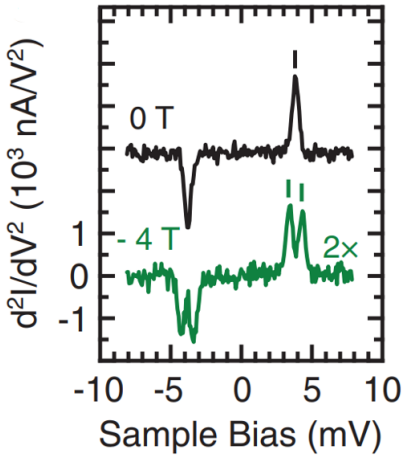

Figure 2.6: Zeeman splitting of the d^2I/dV^2 peaks from a nickelocene functionalized tip on Ag(110) under B_z= 4 T at 0.6 K and 0.2 mV lock-in amplitude[49].

a lock-in modulation of 0.2 mV under a 4 T magnetic field in the z direction. Under these conditions, the peak-to-peak splitting is 0.92 meV, smaller than the 0.43 meV experimental broadening (Fig. 2.6).

2.1.2 Theoretical framework

Although the nickelocene functionalized tip provides more information from a magnetic molecule compared to a metallic or spin-polarized STM tip, extracting this information from the spectroscopic data is far from trivial. All the features induced by approaching a nickelocene tip to a magnetic sample can be produced by several quantum phenomena (dipolar interactions, exchange coupling, Kondo effect, external magnetic fields, transport effects, etc.) impossible to catalog or recognize only by plotting the $\mathrm{d^2I/dV^2}$ versus the bias while retracting the tip. The interaction that decays with tip-sample distance can only be fitted to a model particularly tuned for each molecular system. This requires a solid theoretical background that provides the necessary tools to unveil the information from the nickelocene tip's spectrum. Previous works [49, 56, 58, 63] utilize almost exclusively the Heisenberg Hamiltonian for a two-site model consisting of a partially-filled $3d^8$ shell of the nickelocene and another orbital with the sample's spin. This is a simplification of the more general Hubbard model[27, 64, 65] when the charge transfer between sites is negligible, as it is in most cases for the nickelocene. Charge transfer is then disregarded, and there is an inter-site hopping $t(z)$ and an exchange coupling parameter $J \approx t^2/U$ with U being the electrostatic Coulomb repulsion. Since U decays exponentially with the tip-sample distance z, the dependence of J with z goes as follows:

$$J(z) = J_0 \mathrm{e}^{-az} \tag{2.1}$$

With a being a decay constant and J_0 the exchange coupling at the closest distance

(maximum exchange). Note that $J > 0$ will favor an antiferromagnetic configuration between the nickelocene and the sample's spin (lower $m_{Nc} + m_{mol} = m_{total}$). The Heisneberg Hamiltonian is then:

$$\hat{H} = g\mu(\hat{S}_{Nc,z} + \hat{S}_{M,z})B_z + D_{Ni}\hat{S}^2_{Ni,z} + D_M\hat{S}^2_{M,z} + E_M(\hat{S}^2_{M,x} - \hat{S}^2_{M,y}) + J\vec{\hat{S}}_{Nc} \cdot \vec{\hat{S}}_M \quad (2.2)$$

Where the sub index M refers to the magnetic molecule, Nc for nickelocene, and the spin operators for nickelocene $\vec{\hat{S}}_{Nc}$ and the molecule $\vec{\hat{S}}_M$ are:

$$\vec{\hat{S}}_{Nc} = \hbar(\hat{\sigma}^1_x \otimes I_n, \hat{\sigma}^1_y \otimes I_n, \hat{\sigma}^1_z \otimes I_n) = (\hat{S}_{Nc,x}, \hat{S}_{Nc,y}, \hat{S}_{Nc,z}) \quad (2.3)$$

$$\vec{\hat{S}}_M = \hbar(I_3 \otimes \hat{\sigma}^n_x, I_3 \otimes \hat{\sigma}^n_y, I_3 \otimes \hat{\sigma}^n_z) = (\hat{S}_{M,x}, \hat{S}_{M,y}, \hat{S}_{M,z}) \quad (2.4)$$

The first term in Eq. 2.2 accounts for the Zeeman splitting, with g as the gyromagnetic factor, μ the magnetic permeability, and B_z as an external magnetic field perpendicular to the sample. I_3, I_n represent the identity matrices for spin dimensions 3 ($NiCp_2$) and n (molecule), and $\hat{\sigma}^1_{x,y,z}, \hat{\sigma}^n_{x,y,z}$ are the Pauli matrices for $S_{Nc} = 1, S_M$. $\hat{H}$ and each spin operator $\hat{S}_{x,y,z}$ has a dimension of $dim(\hat{\sigma}^3) \cdot dim(\hat{\sigma}^n)$. D_{Ni} is the nickelocene's $S = 1$ out-of-plane magnetic anisotropy, and D_M, E_M are the molecule's out-of-plane and in-plane magnetic anisotropy terms. The procedure involves diagonalization of the Heisenberg Hamiltonian to obtain the energy eigenvalues as a function of J. The exchange coupling parameter is directly linked with the inter-site hopping t. It is directly related to the distance between orbitals, so the tip-sample distance and the decay a play a key role when probing with a nickelocene tip, affecting the mixing of nickelocene and molecule states and altering the appearance of the d^2I/dV^2 peaks. A single spectroscopy does not provide

enough information to fit the exchange coupling. To model its decay, several d^2I/dV^2 curves must be taken at different heights to extract the height dependence and finally fit the eigenvalue evolution with the tip-sample distance. A more detailed explanation of the Heisenberg model and the exchange coupling can be found in the Attachments. In the following sections, the key concept of magnetic anisotropy is detailed, as well as the cotunneling theory that complements the Heisenberg model with the transport effects that it does not take into consideration.

Magnetic anisotropy

A material is magnetically anisotropic if it presents different magnetic properties depending on the spatial direction. On the molecular scale, magnetic anisotropy manifests itself as the energy required to transition from different spin states due to the molecule's geometry and environment. The perfect example is the nickelocene's triplet state. While those different spin states $m_s = 0, \pm 1$ are degenerated in a spherical environment, the nickelocene z-stacked geometry induces a zero-field splitting between low $m_s = 0$ and high $m_s = \pm 1$ spin states (Fig. 2.7). This energy separation breaks the degeneracy and allows defining high and low spin states with a different magnetic moment (hard axis and easy axis). The amount of energy required for this transition is related to the spin-orbit coupling [27][46]. For $3d$ systems, this coupling is negligible compared to the crystal field, which is much stronger than the orbital spin[47], and the magnetic anisotropy can be related to the spin by $\hat{H} = D\hat{S}_z^2$. The D parameter accounts for the out-of-plane magnetic anisotropy, and $D > 0$ will favor low spin configurations of the molecule's electrons. It is a proportionality constant that links the energy required to change from one spin state to another with the m_s of those levels. For example, a $S = 2$ molecule has $m_s = 2, 1, 0, -1, -2$, and the out-of-plane magnetic anisotropy is tailored by this number with D as a proportionality constant, being the transition energies $\epsilon = 4D, D, 0$. Another term E can be added to describe the in-plane

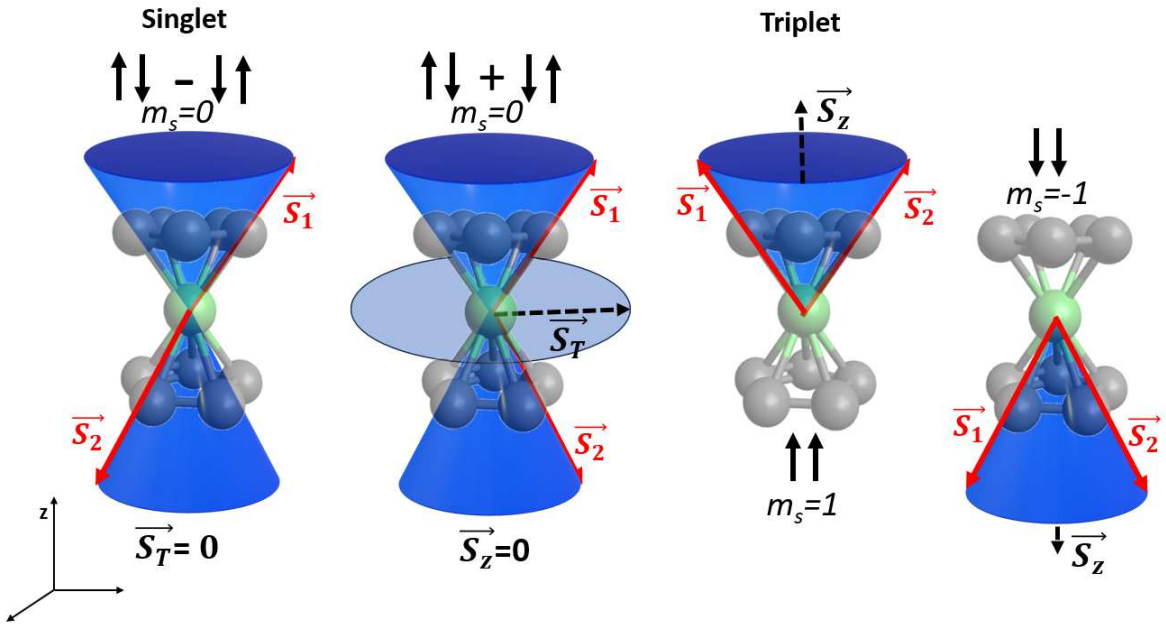

Figure 2.7: Spatial orientation of the low spin (in-plane) versus the high spin (out-of-plane) in the $NiCp_2$ with respect to the z-axis (hard axis). The red arrows $\vec{S}_1, \vec{S}_2$ represent the total spin operator of each one of the nickelocene's single electrons maintaining $\vec{S}_z = \vec{S}_{z1} + \vec{S}_{z2}$ fixed. The nickelocene's total spin is $\vec{S}_T = \vec{S}_1 + \vec{S}_1$. The singlet state shows the electron's spin coupled antiferromagnetically and in contra-phase, so $\vec{S}_T = 0$, $m_s = 0$. The triplet state presents three possibilities, one with an antiferromagnetic and in-phase configuration $m_s = 0$ and two in a ferromagnetic and in-phase configurations $m_s \pm 1$. The term $D\hat{S}_z^2$ is the energy corresponding to a spin flip from $m_s = 0$ to $m_s = \pm 1$. The spin-orbit coupling is not taken into account.

magnetic anisotropy, ending up with a spin Hamiltonian that describes the phenomenon:

$$\hat{H} = D\hat{S}_z^2 + E(\hat{S}_x^2 - \hat{S}_y^2) \tag{2.5}$$

Where $\vec{\hat{S}} = (\hat{S}_x, \hat{S}_y, \hat{S}_z)$ is the spin operator of the molecule in consideration. A worked-out example to obtain the energies and eigenfunctions of an $S = 1$ molecule can be found in the Attachments. Magnetic anisotropy is especially relevant for single atoms deposited on a surface. Due to the spherical symmetry of the orbitals (degeneration of the orbital quantum number m_l), the net magnetic moment of a free single atom of any spin is zero. If this atom is allocated under a magnetic field, m_s will break the degeneracy on the direction

of the magnetic field independently of the spatial orientation, i.e. there is no magnetic anisotropy. The picture dramatically changes when the atom is adsorbed on a surface. This allows the atom to bond[66], alter its spin due to scattering with the substrate electrons[67], experience exchange coupling with neighboring atoms[68, 69], and many other interactions that will change its nature[26]. Under these conditions, and if $S > 1/2$ to have different spin states, the atom's spin may have an easy axis and hard axis direction. This implies that the atom will need a certain amount of energy to transition from the low spin to the high spin configuration by a spin-flip event, measurable by IETS as steps in the dI/dV. Note that only transitions that fulfill the selection rules $\Delta m_s = 0, \pm 1$ are allowed and therefore visible in IETS. In the case of out-of-plane magnetic anisotropy, the $\hat{S}_z$ component of the spin will be fixed in a perpendicular direction from the surface with a permanent magnetic moment.

Model for the inelastic tunneling current

The Heisenberg Hamiltonian provides the eigenvalues of the energy, but the IETS measures the inelastic transitions between the different energy states, and transitions are limited by the selection rules $\Delta m_s = 0, \pm 1$. This will forbid certain transitions that would not be visible as $\mathrm{d^2I/dV^2}$ peaks, so a particular energy state will not have a fingerprint of a transition in the IETS. The Heisenberg model does not provide a prediction of the intensity of the conductance either, which can overshadow some energy branches when the transition rates between different energies are significantly different. An attempt to describe the intensity of the transition was carried out by Hirjibehedin *et.al.*[61]. They propose the following equation to rationalize the height of the dI/dV peaks from an IETS spectrum of Fe in a Cu_2N/Cu(100) substrate:

$$I_{i,j} = |\langle \Psi_j | \hat{S}_x | \Psi_i \rangle|^2 + |\langle \Psi_j | \hat{S}_y | \Psi_i \rangle|^2 + |\langle \Psi_j | \hat{S}_z | \Psi_i \rangle|^2 \tag{2.6}$$

Where Ψ_i, j are the initial and final states. This model is in agreement with the experiment and predicts the increase of conductance of the steps at the obtained energies from the magnetic anisotropy Hamiltonian; nevertheless, it fails to predict the step height in other systems, like the double spin flip of the nickelocene over another nickelocene [45][46]. This substantial increment of conductance cannot be rationalized by means of the Heisenberg Hamiltonian. As it is not a model of the tunneling current, it does not include its electronic transport effects. Bachellier[46] suggests the utilization of a strong coupling theory described by Lorente and Gauyacq[70]. In this model for a single adatom, the spin of the incoming electron becomes entangled with that of the adsorbate, causing the original spin state to dissipate, resulting in an enhancement of conductance. A more general solution to properly model the tunneling current consists of implementing the cotunneling theory[71, 72]. To estimate the inelastic current I_{inel} for a certain bias V via cotunneling the second quantization formalism is needed as it is a many-body problem[64]. After obtaining the corresponding eigenstates $|\alpha\rangle$ and energies E_α as a function of the tip-sample distance z, this equation is employed[72]:

$$I_{inel}(V) = \sum_{\alpha,\alpha',i} P_\alpha |\langle\alpha| c_{\mathrm{Ni}} \hat{S}^\dagger_{\mathrm{Ni},i} + c_{\mathrm{M}} \hat{S}^\dagger_{\mathrm{M},i} |\alpha'\rangle|^2 F_{\alpha,\alpha'}(V), \tag{2.7}$$

Where $F_{\alpha,\beta}(V)$ stands for:

$$F_{\alpha,\beta}(V) = \left(\frac{V - E_\alpha + E_{\alpha'}}{1 - \exp\left(-\beta(V - E_\alpha + E'_\alpha)\right)} + \frac{V + E_\alpha - E'_\alpha}{1 - \exp\left(\beta(V + E_\alpha - E'_\alpha)\right)} \right) \tag{2.8}$$

P_α are the populations of the eigenstates $|\alpha\rangle$ at thermal equilibrium, $P_\alpha = \exp\left(-\beta E_\alpha\right)$ with $\beta = 1/K_b T$. Out of equilibrium perturbations are assumed to be negligible at the low bias conditions of the experiment. The coefficients c_{Ni} and c_M represent a relative coupling strength of the nickelocene's spin to the metallic tip and the sample's spin to the substrate. This offers the possibility to vary the coupling strength of the molecule with the

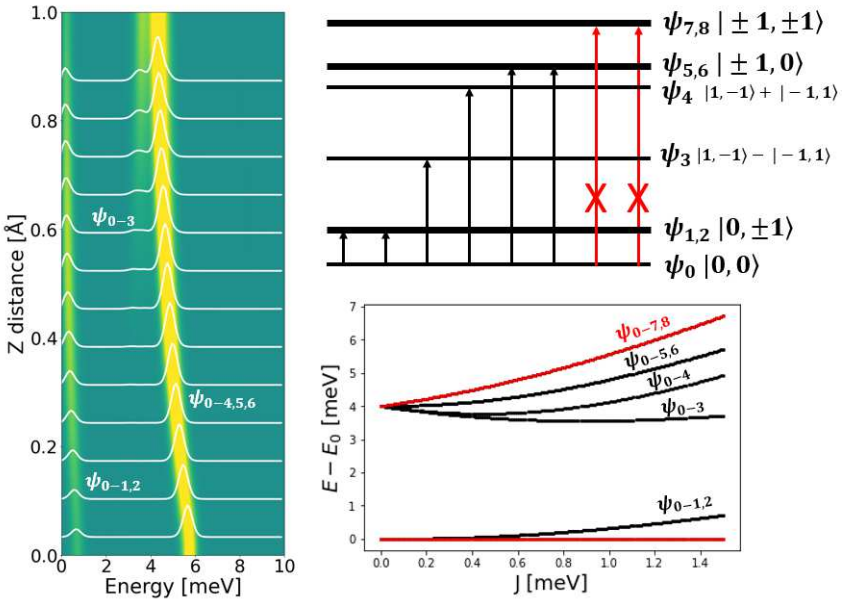

Figure 2.8: Example of a simulation employing the Heisenberg model plus the cotunneling theory with a nickelocene tip on a $S = 1$ molecule without anisotropy. Left: $\mathrm{d^2I/dV^2(z)}$ simulation curves at different Z (white) and color map (yellow=higher positive values of $\mathrm{d^2I/dV^2}$). The exchange coupling at the minimum tip-sample distance is $J = 1$ meV (antiferromagnetic) and decays with height at a $a = 1$ rate. Parameters: 1 K, 100 pm tip retraction, $D_{Nc} = 4$ meV and the coupling strength was 1:3 favoring the sample. Upper-right: Energy diagram. The $\Psi_{0-7,8}$ transitions are forbidden by selection rules. Lower-right: Energy eigenvalues respect to the exchange coupling $J(z)$. The forbidden energy branch (red) is not visible in a). The lower red line represents the ground state energy. The simulation effectively disregard the forbidden transitions and assigns different weight to the energy branches.

substrate and the nickelocene with the metallic tip, so the simulated current plots can show differences in intensity and contrast to better reproduce unequal peaks in the $\mathrm{d^2I/dV^2}$ or enhance spectral features hidden by the differences in contrast.

Dipolar field

Some systems may have extra contributions to the magnetism apart from the Heisenberg model's exchange coupling and Zeeman splitting. In some cases it can be modeled as an effective dipolar field emerging from the magnetic sample that affects the nickelocene differently as a function of the distance:

$$\vec{B}_i(\vec{r}) = \mu_0 \frac{(\vec{m} \cdot \hat{u}_r)\hat{u}_r - \vec{m}}{|\vec{r} - \vec{r}_i|^3} \tag{2.9}$$

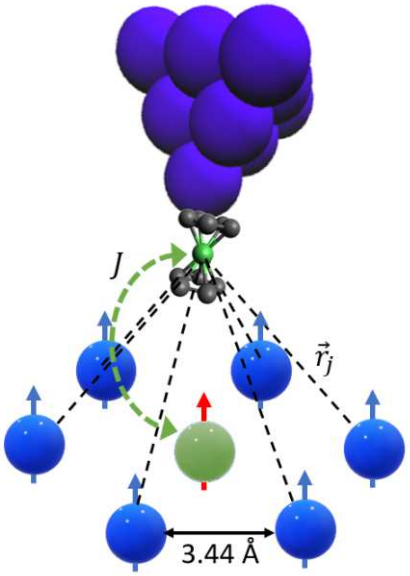

Figure 2.9: Schematic representation of the two-site spin model with an antiferromagnetic exchange interaction J acting between the center atom (green) and the nickelocene on the tip. The dipolar field emerges from the neighboring atoms (blue) conforming a regular hexagon.

Where $\vec{m}$ is the magnetic dipole, $\vec{r}_i$ is the position of atom i and $\hat{u}_r$ is the unit vector $\hat{u}_r = (\vec{r} - \vec{r}_i)/|\vec{r} - \vec{r}_i|$.. This contribution was utilized to model the contribution form the 2D $NiCl_2$ lattice (see Chapter 3 "2D magnetic materials"). the dipolar field is created by the $NiCl_2$ hexagonal lattice and splits the nickelocene's d^2I/dV^2 peaks as it gets closer to the surface. This contribution was conceived after considering an hexagonal distribution of

six magnetic dipoles separated by 3.4 as in the MCl_2 lattices, while the exchange coupling only takes part on the center Ni atom, not involved in the dipolar field (Fig. 2.9). The dipolar contribution added to the Heisenberg Hamiltonian is $\mu_B \vec{B}_{\text{ext}} \cdot \hat{\vec{S}}$, with $\hat{\vec{S}}$ the total spin operator of the two-site model:

$$\hat{H}_{\text{dipole}} = \mu_B \mu \sum_i \frac{(\vec{m} \cdot \hat{u}_r)\hat{u}_r \cdot \hat{\vec{S}}_{\text{Ni}} - m_z \hat{S}_{\text{Ni},z}}{\left(x_i^2 + y_i^2 + z^2\right)^{3/2}} \tag{2.10}$$

2.1.3 Atomic-scale Spin Sensing with a Nickelocene STM tip

In this section, the state of the art concerning the usage of nickelocene as a spin sensor is presented based on previous publications. Some cases are further theoretically analyzed for a more in-depth understanding of the results.

Atomic-scale Spin Sensing with a Single Molecule at the Apex of a Scanning Tunneling Microscope

Due to the general interest in storing information at the single-atom scale using spin as a degree of freedom, numerous STM studies exist involving the magnetic characterization of single atoms. The main disadvantage of using single atoms as qubits is their low relaxation time, leading to perturbations in their spin and compromising the stored information. This problem can be partially overcome by depositing the magnetic atoms on a decoupling layer[38]. However, certain species maintain their magnetic character even when deposited on a bare metal substrate [26, 73, 74]. One of those well-known magnetic systems is composed of Fe single atoms deposited on a Cu(111) surface[75], where Khajetoorians et al. achieved a magnetic moment of $3.5\mu_B$. To further investigate the magnetic properties of Fe, Verlhac et al. probed a Fe single atom adsorbed on Cu(100) with a nickelocene-functionalized tip. They brought the tip close to the Fe atom and then retracted it along the Z-direction while performing d^2I/dV^2 at different heights (Fig. 2.10). It's worth mentioning that the minimum tip-sample distance was 80 pm, as smaller distances led to an abrupt transfer of the nickelocene from the tip to the Fe, forming a different compound. While there were no changes in the d^2I/dV^2 when probing the bare Cu(100) substrate at different heights, the spectrum renormalized when probing with the nickelocene on top of the Fe atom as it sensed its out-of-plane magnetism. The spectral features not only showed peak splitting but also some differences in the heights of the split peaks. Verlhac et al. utilized a Heisenberg-like Hamiltonian to rationalize the obtained spectrum, as in this case, the Fe's

spin is not fixed and can interact with the nickelocene's spin:

$$\hat{H} = D_{Nc}\hat{S}^2_{z,Nc} + D_{Fe}\hat{S}^2_{Fe} - J\vec{\hat{S}}_{Nc} \cdot \vec{\hat{S}}_{Fe} \tag{2.11}$$

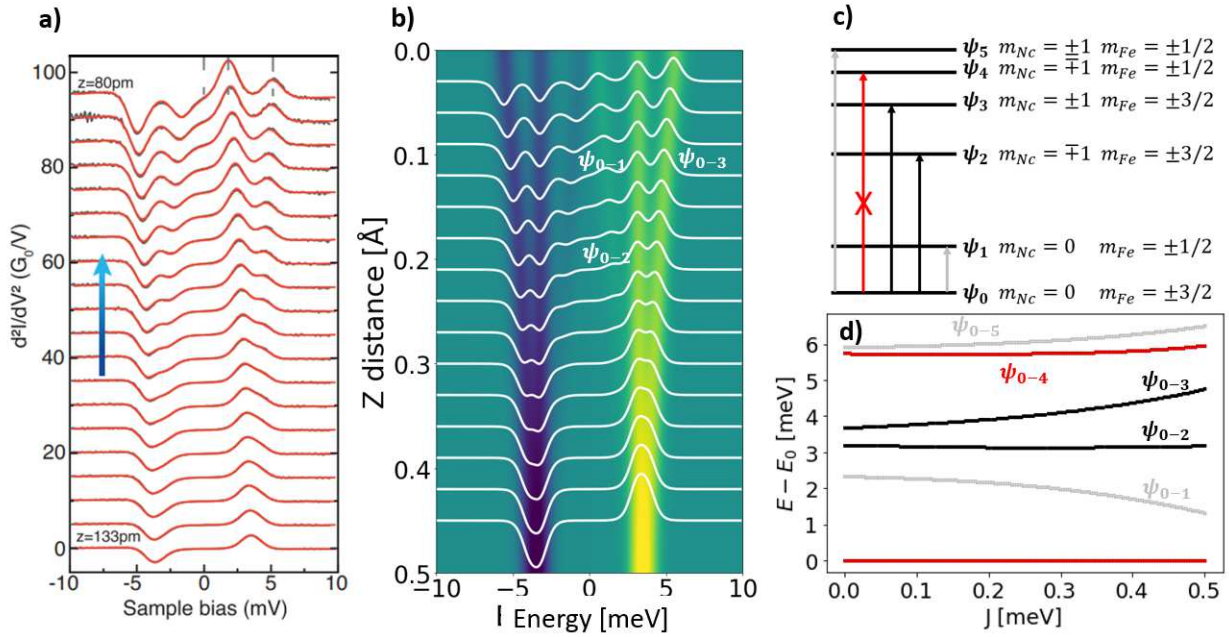

Figure 2.10: a) $d^2I/dV^2(z)$ spectrum at different heights with a $NiCp_2$ tip over a Fe atom on Cu(100) (Verlhac *et.al.*[63]) b,c,d Simulations from the Heisenberg/cotunneling Python script[76]) b) $d^2I/dV^2(z)$ simulation curves at different Z (white) and color map (yellow=higher positive values of d^2I/dV^2). The exchange coupling at the minimum tip-sample distance is $J = 0.8$ meV (antiferromagnetic) and decays with height at a $a = 3$ rate. Parameters: 2.4 K, 50 pm tip retraction, $D_{Nc} = 3.4$ meV, $D_{Fe} = -1.2$ meV, $S_{Fe} = 3/2$ and the coupling strength was 1:3 favoring the Fe atom. . c) Energy diagram of the $NiCp_2$/Fe. The $\Psi_{0-1,5}$ transitions are barely visible (Ψ_{0-1}, Ψ_{0_5} were not experimentally observed), and Ψ_{0-4} is forbidden. d) Energy eigenvalues respect to the exchange coupling $J(z)$.

The term $\vec{\hat{S}}_{Fe}$ accounts for the spin vector of the $S = 3/2$ Fe atom on Cu(100), D_{Nc} and $\vec{\hat{S}}_{nc}$ represent nickelocene's $S = 1$ magnetic anisotropy and spin vector, and J is an exchange-coupling parameter. The adsorbed Fe atom did not exhibit any IETS feature in the probed bias range at 2.4 K. For extracting the magnetic anisotropy, DFT calculations were performed for a Fe atom adsorbed in the hollow site of Cu(100) (with C_{4v} symmetry). These calculations provided a magnetic moment of $< m_s >= 3.4\mu_B$ and an effective spin of

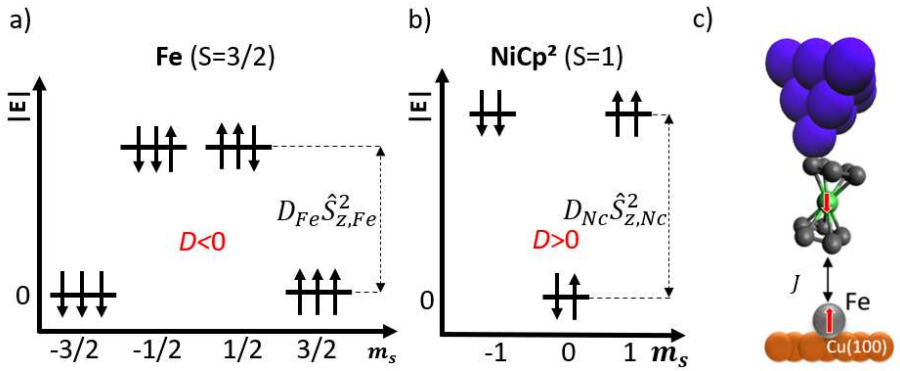

Figure 2.11: a), b) Energy diagrams representing the spin states of the Fe on Cu(100) and the nickelocene functionalized tip respectively according to their magnetic anisotropy sign ($D_{Ni} > 0, D_{Fe} < 0$). c) Representation of a nickelocene tip and a Fe atom on Cu, correlated by the exchange-coupling constant J which is a function of the tip-sample distance.

$S_{Fe} \approx 3/2$, determined by $< m_s >= g\sqrt{S(S+1)}\mu_B$ assuming $g \approx 2$ and an out-of-plane magnetic anisotropy of unknown sign and magnitude. It's worth noting that the magnetic anisotropy for a Fe atom on Cu(111), as obtained by Kajetoorians *et al.* [75], is $D_{Fe} \approx -0.85$ meV. The sign of the magnetic anisotropy, D, determines which spin configuration is lower in energy (in absolute value): $D < 0$ favors the high spin states ($m_{Fe} = \pm 3/2$), while $D > 0$ favors the low spin states ($m_{Nc} = 0$) (Fig. 2.11).

Transitions from nickelocene's ground state $m_{Nc} = 0$ to the excited states $m_{Nc} = \pm 1$ require a change in the total spin of $\Delta m_s = 1$. As the total spin must be conserved, the allowed transitions must involve spin-flip events that do not change the total spin. Among the possible transitions, Ψ_{0-4} (Fig. 2.10) does not conserve the total spin. Some allowed transitions are disregarded as they are not noticeable in the spectroscopy as spin-flip events between two spin states of the Fe.

The simulated evolution of the energy eigenvalues with J for the transitions Ψ_{0-2} and Ψ_{0-3} is similar to the splitting of the d^2I/dV^2 seen in the experiment, providing a rationalization of the spectrum (Fig. 2.10). Upon closer inspection of the experiment, as there is no spectroscopic evidence of a spin-flip transition Ψ_{0-1}, the authors suggest that

the thermal energy $k_bT \approx 0.2$ meV is greater than $|D_{Fe}|$, so Fe is always at $m_{Fe} = \pm 1/2$ on the bare Cu(100) (high spin). For this reason, the authors justify reformulating the Hamiltonian exchange-coupling term as an effective Zeeman splitting by disregarding D_{Fe}: $J\hat{S}_{z,Fe}\hat{S}_{z,Nc} = g\mu_B B_Z \hat{S}_{z,Nc}$. This Zeeman splitting on the $m_{Nc} = \pm 1$ peaks has an exponential decay with the tip-sample distance Z of $e^{-Z/a}$, where $a \approx 34$ pm, to explain the decreasing splitting with the tip-sample distance. Using a DFT-calculated effective spin of $< S_{Fe} > \approx 1.7$, the obtained exchange coupling is $|J| \approx 1.7$ meV at the shortest Z. According to their hypothesis, as $|D_{Fe}| >> |J|$, the Heisenberg interaction is indistinguishable from an Ising interaction, making it impossible to assign J a ferro or antiferromagnetic character.

Departing from here, I utilized these results to run the simulation based on the Heisenberg Hamiltonian complemented with the cotunneling theory described in the Theoretical Methods part. This simulation (Fig. 2.10), obtained with $D_{Fe} = -1.2$ meV and $J(Z) = 0.8$ meV with a Z decay of $a = 3$ Å, shows the mildness of the Ψ_{0-1} transition, easy to overlook in their experiment, after assuming a coupling strength of 1:3 favoring the Fe atom. This implies that the Ψ_{0-1} transition may have been present in Verlhac's work but disregarded. Their assumption about the anisotropy being lower than the thermal broadening may not be correct, looking at the information about the current that the cotunneling provides. This ultimately implies that the system cannot be simplified as an effective magnetic field, as the exchange coupling and the coupling strength play a significant role. As a final remark, note that while transition Ψ_{0-4} is forbidden, Ψ_{0-5} is not, but it is invisible in the experiments and our simulation. As transition Ψ_{0-5} implies going from $m_s = \pm 3/2$ to $m_s = \pm 5/2$, and the selection rules only allow $\Delta m_s = 0, \pm 1$, only half of the possible transitions are allowed. This causes a dramatic reduction of tunneling current compared to the other allowed transitions, and the Ψ_{0-5} feature becomes invisible in the conductance plot.

Although our model seems to provide more information about the current, it does not

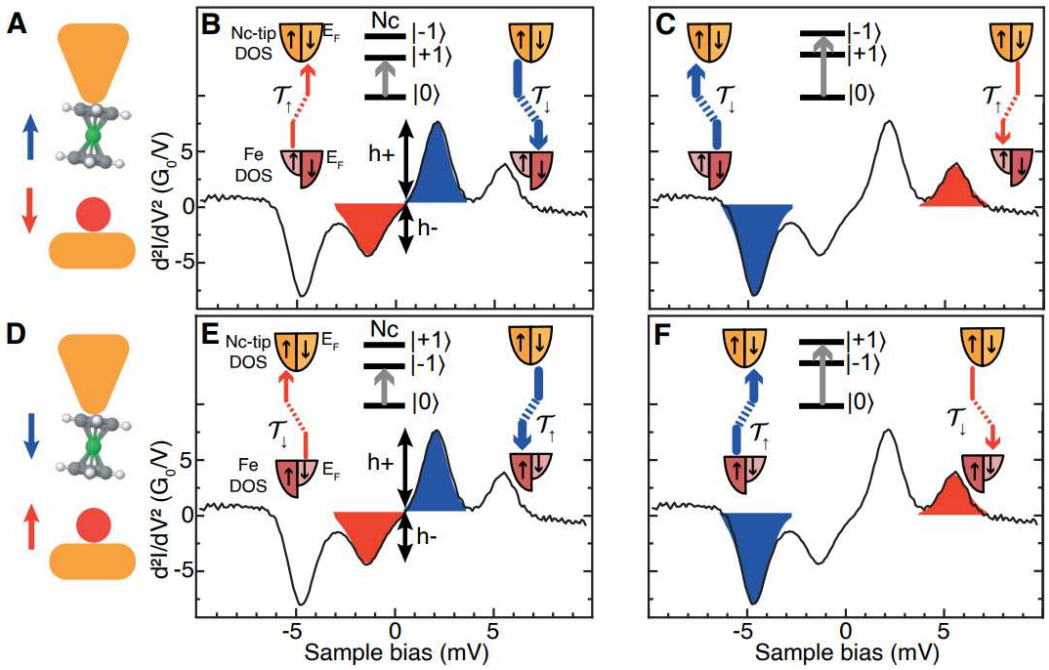

Figure 2.12: Asymmetries on the IETS of the nickelocene-Fe system.[63] a) Fe atom (red) and nickelocene functionalized tip (Fe atom $m_{Fe} = -3/2$ spin point downwards). b),c) Spin-dependent transmission T from $|0; \pm 3/2\rangle$ to $|1; -3/2\rangle$ (antiparallel) and $|-1; -3/2\rangle$ (parallel) (Ψ_{0-3},Ψ_{0-2}). e),f) Opposite configuration with $m_{Fe} = -3/2$ depicting the transitions from $|0; \pm 3/2\rangle$ to $|-1; 3/2\rangle$ (antiparallel) and $|1; 3/2\rangle$ (parallel) (Ψ_{0-2},Ψ_{0-3}).

offer any insight into the peak's asymmetry. Verlhac *et.al.* explained this as a tunneling magnetoresistance effect[23] that polarizes the current depending on the states the electrons are tunneling from. As the Fe on Cu(100) possesses out-of-plane magnetic anisotropy and there is no external magnetic field affecting the system, the $m_{Fe} = \pm 3/2$ is parallel to the perpendicular axis (Z), pointing up or down, respectively. This leads to an asymmetry in the Fe ground state, as the density of states has a spin imbalance favoring the electrons whose spin has the same orientation as $m_{Fe} = \pm 3/2$. As the polarized electrons from the Fe atom tunnel to the nickelocene's $m_{Nc} = \pm 1$, the transmission is lower for antiparallel spin configurations. This translates into different transmission factors T for each spin configuration in Ψ_{0-2} and Ψ_{0-3} transitions (Fig. 2.12), averaging a spin asymmetry of $\eta = 23\%$, explaining the peak asymmetry in the IETS.

Probing and imaging spin interactions with a magnetic single-molecule sensor

In the same spirit, Czap *et.al*[49] performed another height dependence measurement with a nickelocene functionalized tip on a nickelocene adsorbed on an Ag(110) surface under a magnetic field of 1 T oriented in the out-of-plane direction, proposing a very similar Heisenberg Hamiltonian to interpret the coupling between both $NiCp_2$:

$$\hat{H} = g\mu_B B_z(\hat{S}_{z1} + \hat{S}_{z2}) + D_1\hat{S}_{z1}^2 + D_2\hat{S}_{z2}^2 + J\vec{\hat{S}}_1 \cdot \vec{\hat{S}}_2 \tag{2.12}$$

The $dim = 9$ spin operators for both $\vec{\hat{S}}_{1,2}$ nickelocene molecules are:

$$\vec{\hat{S}}_1 = \hbar(\hat{\sigma}_x^1 \otimes I_3, \hat{\sigma}_y^1 \otimes I_3, \hat{\sigma}_z^1 \otimes I_3) = (\hat{S}_{1,x}, \hat{S}_{1,y}, \hat{S}_{1,z}) \tag{2.13}$$

$$\vec{\hat{S}}_2 = \hbar(I_3 \otimes \hat{\sigma}_x^1, I_3 \otimes \hat{\sigma}_y^1, I_3 \otimes \hat{\sigma}_z^1) = (\hat{S}_{2,x}, \hat{S}_{2,y}, \hat{S}_{2,z}) \tag{2.14}$$

Where $I_3, \hat{\sigma}_{x,y,z}^1$ are the $dim = 3$ identity and $S = 1$ Pauli matrices respectively. $J > 0$

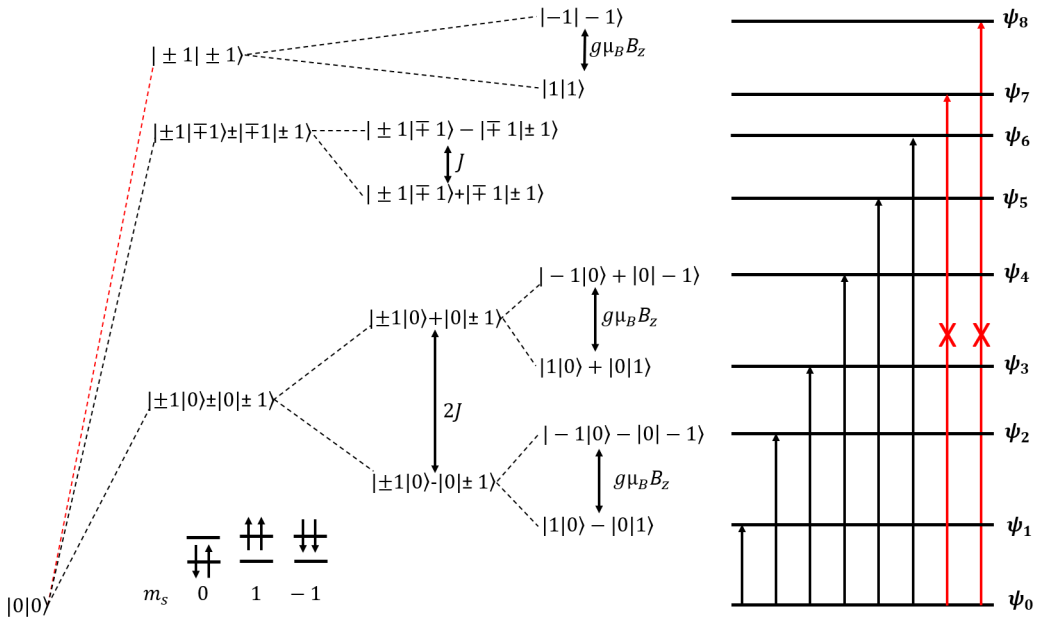

Figure 2.13: Energy levels and transitions between the eigenstates $\Psi : |m_1|m_2\rangle$ that account for the splitting in the d^2I/dV^2 from the two nickelocene system[49]. Ψ_{0-7}, Ψ_{0-8} transitions are forbidden by selection rules. The $1/\sqrt{2}$ normalization in the mixed states is obviated.

(antiferromagnetic) and $D_1 = D_2 \approx 4$ meV are the magnetic anisotropies also for both $NiCp_2$. We performed a simulation based on their parameters using the described hamiltonian plus the cotunneling theory to simulate the actual current, obtaining a good agreement with their experimental data (Fig. 2.14). As detailed before (See section 2.2), the electronic structure of this system in the absence of a magnetic field or exchange coupling presents a single spin-flip at 4 meV and a double spin-flip at 8 meV. As depicted in Fig. 2.13, the ground state corresponds to $|0|0\rangle$ which will derive in mixed states as the tip gets closer. The exchange coupling will split the double spin-flip state into $\frac{1}{\sqrt{2}}(|\pm 1|\mp 1\rangle + |\mp 1|\pm 1\rangle)$ states. The single spin-flip state $\frac{1}{\sqrt{2}}(|\pm 1|0\rangle + |0|\pm 1\rangle)$ will also be affected by the exchange coupling and get further degenerated by the magnetic field. The authors remark the impossibility of $|0|0\rangle$ to $|\pm 1|\pm 1\rangle$ ($\Delta m_s = \pm 2$) transitions as they imply breaking the $\Delta m_s = 0, \pm 1$ spin selection rule, and as a result, this excitation is not seen in the d^2I/dV^2(z) from Fig. 2.14 as another branch with $E > 9$ meV.

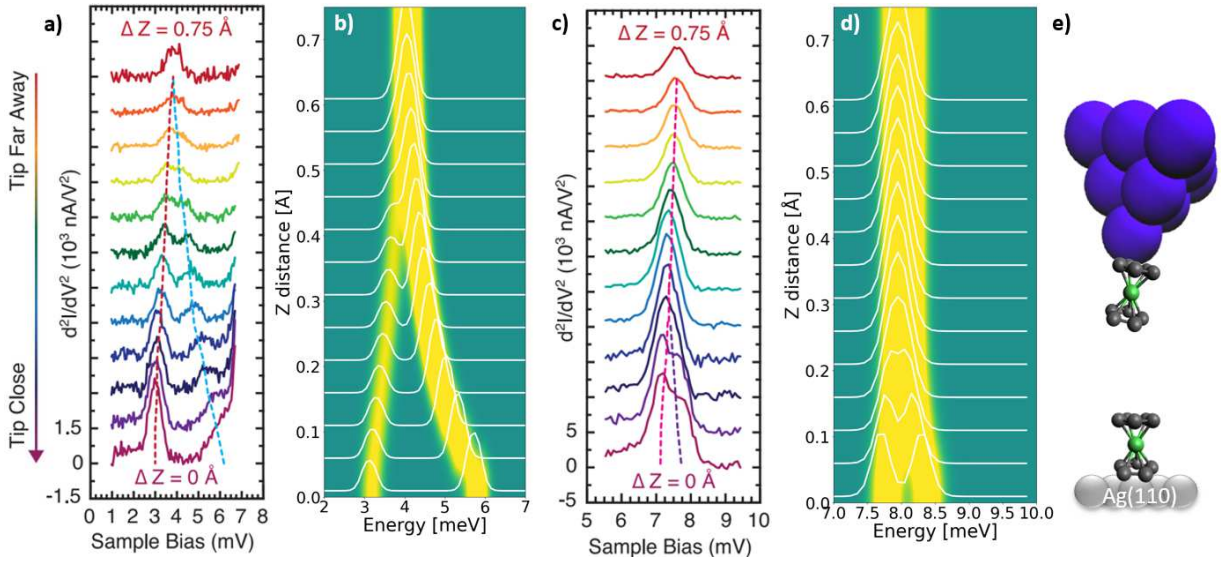

Figure 2.14: a,c) $d^2I/dV^2(z)$ spectrum of a nickelocene tip over a nickelocene adsorbed on Ag(110) at 1 T, 0.6 K and different tip-sample distances (Czap *et.al.*[49]). a) Splitting of the single spin-flip energy peak $\frac{1}{\sqrt{2}}(|\pm 1|0\rangle \pm |0|\pm 1\rangle)$. The exchange coupling beaks the degeneracy by a factor of J that scales with Z. b) Splitting of the double spin-flip energy peak $\frac{1}{\sqrt{2}}(|\pm 1|\mp 1\rangle \pm |\mp 1|\pm 1\rangle)$ the exchange coupling breaks the degeneracy by lowering the energy only from the (+) state. The (-) state stays unaltered. b,d) $d^2I/dV^2(z)$ simulations. The exchange coupling at the minimum tip-sample distance is $J = 1.3$ meV and decays with height at a $a = 1$ Å rate. Parameters: 0.6 K, 1 T, 750 pm tip retraction, $D_{Nc} = 4$ meV and the coupling strength was 1:3 favoring the surface nickelocene. e) Representation of a nickelocene functionalized tip approaching another nickelocene molecule on Ag(110) surface.

2.2 The Cobaltocene molecule

Although this thesis mainly focuses on the utilization of the nickelocene as a magnetic sensor, the cobaltocene ($CoCp_2$) has been studied by means of STM[46] and employed for magnetic sensing as well[53]. It has metallocene structure and a Co metal center with only one unpaired electron shared by two e^*_{1g} orbitals (Fig. 2.1) making the $CoCp_2$ a $S = 1/2$ molecule. dI/dV spectrum on a cobaltocene over a Cu substrate yields a strong peak around the Fermi energy that is the fingerprint of a Kondo resonance between the unpaired electron and the singly occupied orbital of the cobaltocene with $T_K = 4.3$ K, as detailed in [46, 53] and shown in Fig. 2.15.

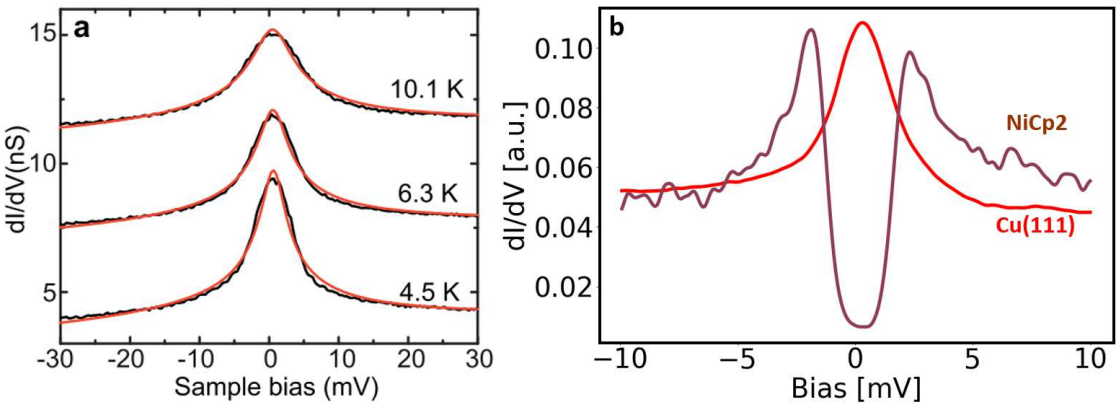

Figure 2.15: a) dI/dV from a $CoCp_2$ on Cu(100) at different temperatures to prove the Kondo character of the peak[53]. b) dI/dV with a cobaltocene tip over Cu(111) (red) and a nickelocene deposited on Cu(111) (brown) measured at 1.2 K. The nickelocene's square ±4 meV dip gets 'pointy' under the cobaltocene's influence.

It is possible to functionalize an STM tip with a cobaltocene and perform STS to exchange-couple its single electron with the sample's electrons and evaluate the decay of this exchange with the tip-sample distance variation in the same manner as with the nickelocene. The main difference, apart from the electronic structure, is the aggressive response of the cobaltocene to Au or Ag substrates. The cobaltocene gets decomposed when deposited on these substrates, and even the thin Au or Ag coating of the tip may influence cobaltocene

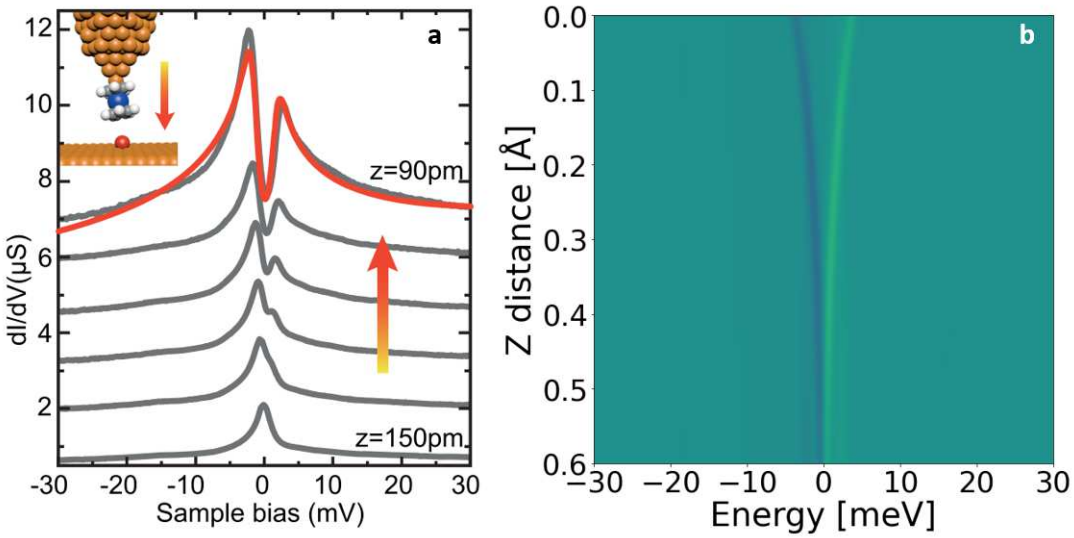

Figure 2.16: a) dI/dV(z) with a $CoCp_2$ probing a Fe atom on Cu(100) at 2.4K as the tip sample distance increases[53]. b) $d^2I/dV^2(z)$ current simulation with a modification of the Python script for a cobaltocene molecule[76]. The parameters are: $S = 3/2$, 2.5 K, 1:3 coupling strength favoring the Fe, D[0,0,-1.2] meV as utilized in the nickelocene simulation, an exchange coupling of $J = 2$ meV at the closest distance and a decay constant of $a = 4$ Å for a 0.6 Å tip retraction as in the experiment.

decomposition when scanning, making it mandatory to have a Cu-coated tip and a Cu sample to utilize the $CoCp_2$. The mechanism of this reaction of the molecule to the tip and substrate remains unknown and it could be an interesting subject of study.

To further understand its utilization let us analyze Garnier *et.al.* work[53] characterizing a $S = 3/2$ Fe atom deposited on a Cu(100) substrate (the same system prepared for the nickelocene measurement by Verlhac *et.al.* [63]).

The rationalization proposed by Garnier *et. al.*[53] consist of a simplification of the Heisenberg Hamiltonian by considering again an effective magnetic field that causes the d^2I/dV^2 peaks to split by Zeeman effect when approaching the cobaltocene tip to the Fe atom $H = g\mu B_{eff} S_{z,Fe}$. For comparison, let us examine the system using a more complete two-site Heisenberg Hamiltonian and implementing the cotunneling to obtain a simulation of the current. The Heisenberg Hamiltonian is:

$$\hat{H} = D_{Fe}\hat{S}^2_{Fe,z} + J\vec{\hat{S}}_{Cc} \cdot \vec{\hat{S}}_{Fe} \tag{2.15}$$

The $dim = 8$ spin operators for both the molecule and the cobaltocene $\vec{\hat{S}}_{Fe}, \vec{\hat{S}}_{Cc}$ are:

$$\vec{\hat{S}}_{Cc} = \hbar(\hat{\sigma}_x^{1/2} \otimes I_4, \hat{\sigma}_y^{1/2} \otimes I_4, \hat{\sigma}_z^{1/2} \otimes I_4) = (\hat{S}_{Cc,x}, \hat{S}_{Cc,y}, \hat{S}_{Cc,z}) \tag{2.16}$$

$$\vec{\hat{S}}_{Fe} = \hbar(I_2 \otimes \hat{\sigma}_x^{3/2}, I_2 \otimes \hat{\sigma}_y^{3/2}, I_2 \otimes \hat{\sigma}_z^{3/2}) = (\hat{S}_{Fe,x}, \hat{S}_{Fe,y}, \hat{S}_{Fe,z}) \tag{2.17}$$

D_{Fe} is the magnetic anisotropy of the Fe atom and J is the exchange coupling parameter as a function of the tip sample distance z. Fig. 2.16 showcases the experimental dI/dV(z) at different heights, which shows a peak splitting of the original Kondo peak as the cobaltocene tip approaches the Fe. Besides it, the current simulation is displayed showing the $\mathrm{d^2I/dV^2}$(z) and the peak splitting in agreement with the experiments. Some other transitions are barely visible in the upper part of the plot, suggesting the presence of more transitions hindered by the experiment resolution (especially considering the low energy resolution of the dI/dV compared to $\mathrm{d^2I/dV^2}$) that our model provides. This result is analogous to the result obtained by the nickelocene tip, which proves the adequacy of the cobaltocene tip as an spin sensor as well. Note that the cobaltocene molecule may be especially useful for systems with magnetic transitions very close to the Fermi energy as it boosts the current by its Kondo peak in that regime, opposing the nickelocene's tendency of hindering signals lower than its ±4 meV dip that gets overshadowed by the difference of current in and out the energy gap.

So far, the cobaltocene has been successfully modeled as a single spin site of $S = 1/2$.. However, the measured $\mathrm{d^2I/dV^2}$ peaks do not experiment any renormalization as the cobaltocene gets closer to a nickelocene deposited on Cu(111), as one would expected. The only noticeable effect of the cobaltocene tip on the measurement results in a sharpening of

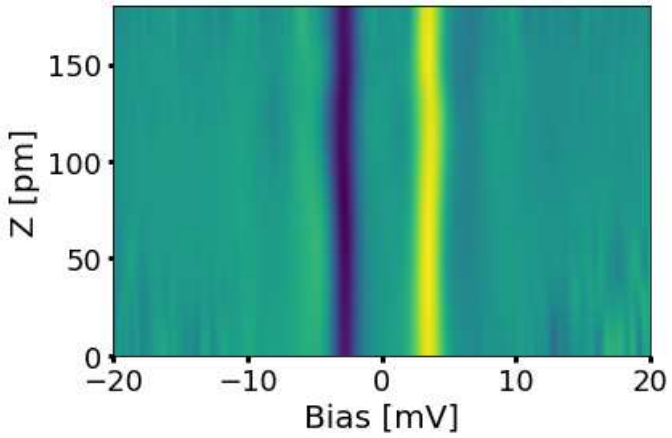

Figure 2.17: $d^2I/dV^2(z)$ of a nickelocene on Cu(111) measured with a cobaltocene functionalized tip varying the tip sample distance z. There is no renormalization of the ±4 meV nickelocene peaks when approaching the $S = 1$ nickelocene. 0 pm = closest distance. (See the "Experimental Details" section for a detailed explanation of the colormap). T=1.3 K, $B_z = 3$ T.

the nickelocene gap (Fig. 2.15). A different theoretical approach may be needed to fully understand the experimental STS from a cobaltocene tip in determined systems where the assumptions made for the nickelocene do not work. As seen in Fig. 2.1, the cobaltocene molecule has one unpaired electron that is shared by two active d orbitals. This hints at a possible fundamental limitation for the spin model so far discussed. To go beyond this shortcoming, we should at least construct a two-sites model for the tip and account explicitly for the charge transfer in the cotunneling simulation (not implemented so far). This can explain the failure of our current model to reproduce the interaction between a nickelocene and a cobaltocene tip (Fig. 2.17), which according to the spin cotunneling model should be equal to the case of a nickelocene approaching a single unpaired electron in one orbital.

2.3 Experimental details

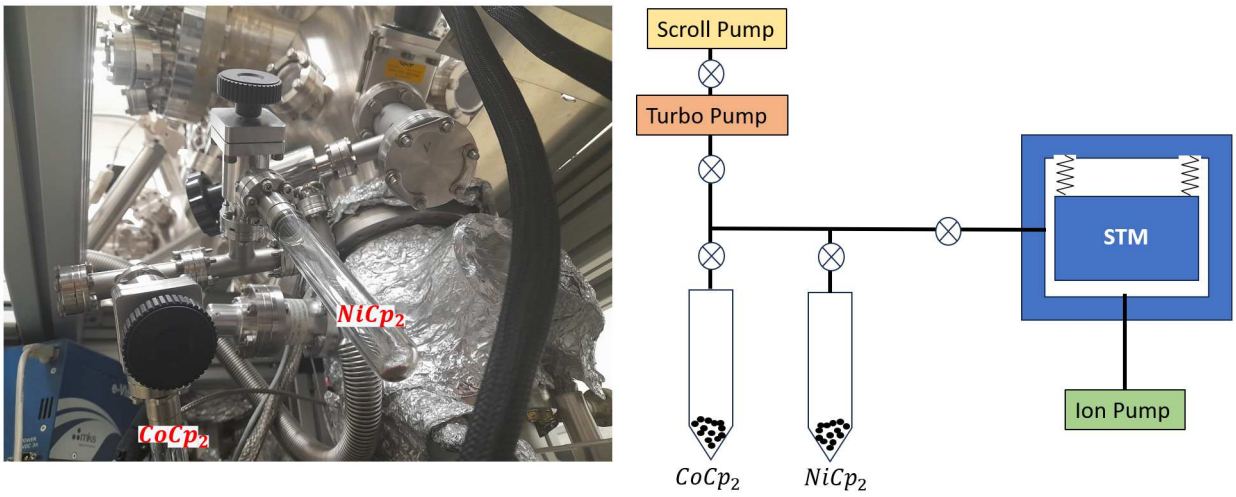

Figure 2.18: Nickelocene and cobaltocene molecules are kept in glass crucibles in static vacuum at RT conditions. Once the gate of one crucible is open to the preparation chamber pressure (8e-8mBar) the pressure increase to 1e-5mBar. When the pressure is stable, the molecules are dosed by a gate valve or a leak valve into the STM chamber, where they adsorb onto the <10K sample.

The SPM experiments were conducted using a commercial low-temperature (1.2 K) STM/nc-AFM microscope with a Specs-JT Kolibri sensor of f ≈ 1 MHz. The spectroscopies were performed with a lock-in amplifier with a 0.5 mV amplitude and 723 Hz oscillation frequency. The nickelocene molecule in the gas phase was deposited onto the prepared sample in the microscope head from a glass crucible with solid powder nickelocene kept at room temperature and static vacuum (Fig. 2.18). As the $NiCp_2$ and $CoCp_2$ molecules are volatile at room temperature in a vacuum, they can be directly dosed into the microscope like a regular gas. To dose it, a leak valve connecting the tantalum pocket to the microscope was utilized. The deposition time lasts 1 s at 1e-5 mbar pressure, which in our setup corresponds to 20-50 molecules per 100 nm^2. This amount hugely depends on the geometry of the evaporation ports and the evaporation-sample distance. Once the metallocene is on the sample, it must be kept below 4 K; otherwise, it diffuses to the step edges. Some

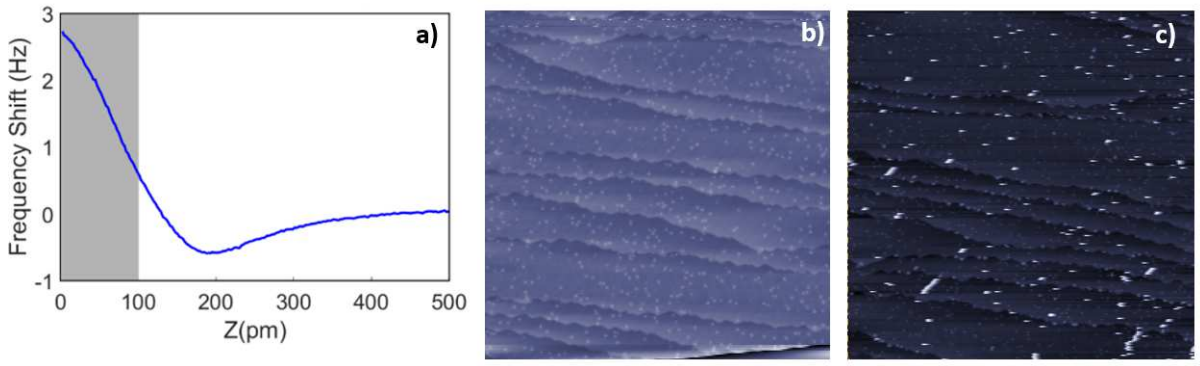

Figure 2.19: a) nc-AFM $\Delta f(z)$ spectroscopy of a nickelocene tip on Au(111) while pressing it onto the surface. The grey highlighted area shows 100 pm of z retraction from the closest position utilized to take $d^2I/dV^2(z)$ series in height, being the assumed tip-sample distance 3 at the minima position, where the repulsion regime starts. b,c) 100x100 nm^2 images (100 mV, 10 pA) of an Au(111) sample with Dy atoms before b) and after c) depositing nickelocene at 4 K. $NiCp_2$ appear like characteristic punctual tip-collisions as white dots and white stripes corresponding to a dragging event.

metallocenes can still be found after keeping the sample at 80 K, but they fully desorb at room temperature. Note that the cobaltocene has only been successfully deposited on Cu substrates.

Prior to tip functionalization, the symmetry of the metallic tip apex needs to be confirmed by scanning a metallocene and obtaining its characteristic ring shape. Usually, the tip gets functionalized spontaneously by scanning at a low current (>100 mV) and a bias setpoint of >50 pA (Fig. 2.19). When the tip gets functionalized, the apparent STM height increases by 4 Å. The usual picking method consists of pressing on top of the metallocene at low bias (1-5 meV) until it functionalizes the tip causing an abrupt change of current. The nickelocene in particular can also be picked up in a controlled way by scanning over the selected molecule at 4 mV with a low current setpoint >10 pA and carefully increasing the setpoint until the nickelocene jumps to the tip. Metallocenes can functionalize the tip in slightly different configurations that can cause instabilities when probing molecules with it. To ensure reproducible functionalization, the metallocene must

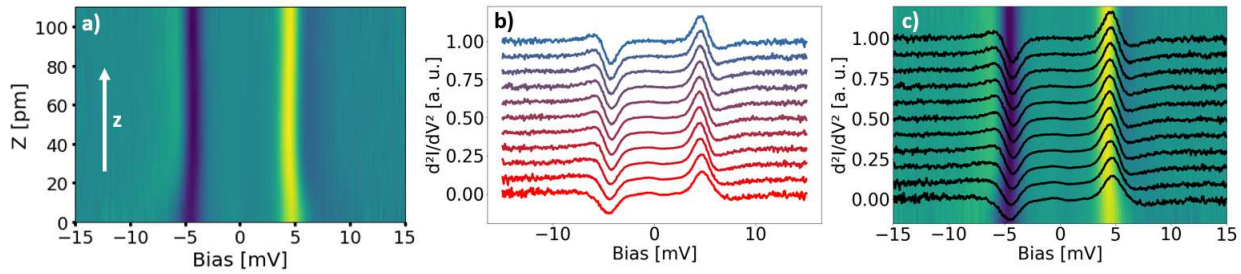

Figure 2.20: Different representations of a height dependent $d^2I/dV^2(z)$ IETS fo a nickelocene tip on Au(111). a) Color map translating the d^2I/dV^2 values to a color scale (black=negative, yellow=positive) for each z height. b) Plain $d^2I/dV^2(z)$ curves (red=closer tip sample distance). c) Both plots together.

rest in a stable configuration and provide its benchmark dI/dV ±4 mV step on a metallic substrate. The stability of the functionalized tip was evaluated by AFM $\Delta f(z)$ spectroscopy by approaching the tip to the closest distance of the measurement's range and retracting it while recording the frequency shift channel to obtain the Lenard-Jones-like curve (Fig. 2.19) (See section 2.1). Stable tips were defined as those that exhibited no hysteric behavior for forward and backward $\Delta f(z)$ curves. Besides, the frequency shift z spectroscopy serves as a mechanism to record the height and repulsion/attraction forces on the metallocene at every step of the height-dependent IETS measurements. To visualize the data, the curves were plotted by a Python script. Several representations were utilized (Fig. 2.20).

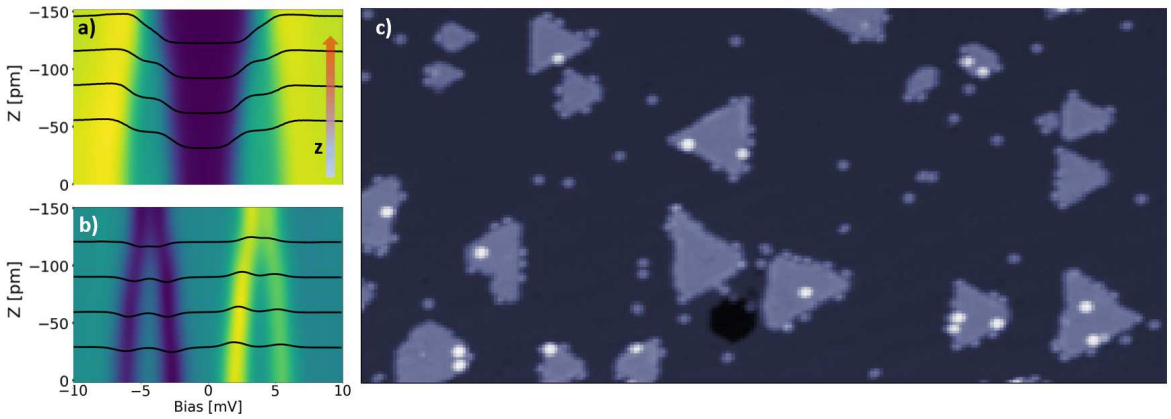

Figure 2.21: Cu(111) substrate with magnetic Co nanoislands[26] (grey triangles) and $NiCp_2$ (white dot=on top of the island/gray dot=on Cu111) deposited at 4K. a) dI/dV(z) with the nickelocene tip approaching the Co island at B=3T, showing the extra step emerging by Zeeman splitting reproducing the results detailed in [63]. b) $d^2I/dV^2(z)$ at the same conditions as a), showing the splitting of the peaks with the height. c) 100 x 50 nm^2 STM image of the sample taken at 100 mV, 10pA current.

Chapter 3

Magnetic systems probed with a Nickelocene functionalized STM tip

This chapter is devoted to showcasing the nickelocene STM tip's spin-sensing capabilities and the subsequent rationalization of the IETS data taken in four different magnetic systems:

- **Designer magnetic topological graphene nanoribbons**[77], by Song *et.al*, Arxiv (2022).
- **Highly-Entangled Polyradical Nanographene with Coexisting Strong Correlation and Topological Frustration**[78], by Song, Pinar, Matej *et.al*, Nature Chemistry (2024).
- **Role of the Magnetic Anisotropy in Atomic-Spin Sensing of 1D Molecular Chains**[79], by Wackerlin *et.al*, ACS Nano (2022).
- **Tunable ferromagnetic order in 2D layers of Transition Metal Dichlorides**, by Aguirre *et.al.* (Submitted to Advanced Materials (2024).

3.1 Graphene's π-magnetism

The magnetic characteristics of carbon-based nanostructures are highly sensitive to subtle alterations in bonding configurations. These structures rely on unpaired π-electrons, known for their significant chemical reactivity[80]. Nevertheless, the development of on-surface synthesis[81–84] enables the production of these materials[85]. The UHV conditions and the stabilizing influence of the cryogenics and substrate facilitate the synthesis of carbon-based nanostructures, limiting chemical degradation. These structures are perfect candidates for study by means of STM. In particular, the π-magnetism of graphene nanostructures is often probed by STS due to its lateral resolution[86]. There are three main mechanisms to obtain an open-shell nanographene with magnetic properties. The first one, also called Class I, consists of exploiting the topological frustration of a bipartite honeycomb lattice via sub-lattice imbalance, with the triangulene molecule being a well-known example[87–90]. The second mechanism, known as Class II, is another topological frustration, in this case, of two sets of balanced honeycomb bipartite lattices, as in Clar's goblet[85]. In both Class I and II systems, topological frustration generates unpaired π-electrons that can couple in several ways. The electron-electron interaction is the last mechanism to generate π-magnetism, arising from the Coulomb repulsion of the delocalized electrons on the honeycomb lattice, as in the rhombene nanographene[91]. All of these magnetic graphene classes have been extensively studied by means of STM and ncAFM techniques, making them perfect candidates for nickelocene tip IETS probing.

3.1.1 Designer magnetic topological graphene nanoribbons

In polycyclic aromatic hydrocarbons, such as the graphene honeycomb lattice, Clar's rule [92–94] establishes a connection between aromaticity and the stability of the molecule. In graphene nanostructures, this implies that the most stable configuration is achieved when the aromatic resonances are maximized. In this work[77], zigzag nanographene units (tzGNR) are fused to conform to a bigger nanographene. Clar's rule predicts a transition from close to an open-shell configuration as the tzGNR units are fused together in a bigger structure. This favors the creation of topological magnetic radicals at the edges of the tzGNR populated by localized π-electrons. In order to investigate these molecules, an anthracene-based unit was functionalized by Br atoms conforming the tzGNR building block. The brominated precursor was deposited in UHV deposition by Knudsen-cell evaporation on an Au(111) sample. The on-surface synthesis consisted of annealing the precursor to induce Ullman coupling by dehalogenation of the Br atoms to fuse the tzGNR units, and then cyclodehydrogenation to conform the final molecule. As a result, different lengths of GRNs were observed in the STM images and characterized by ncAFM and CO/metallic tip STS.

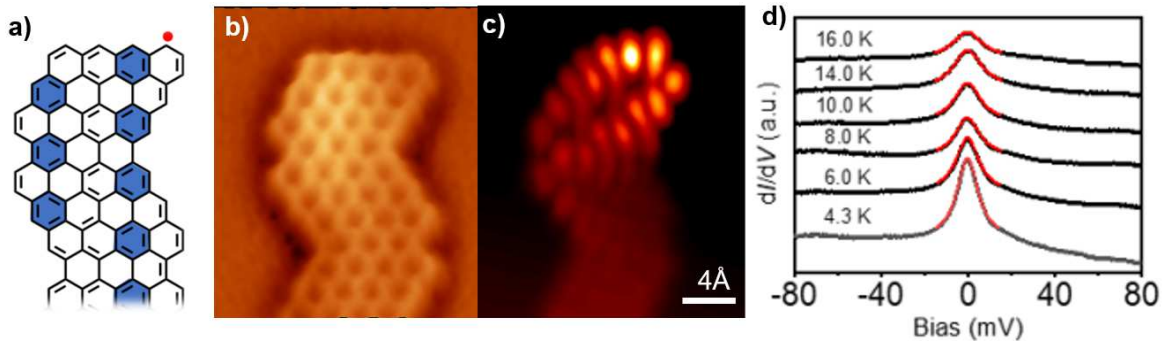

Figure 3.1: GNR on Au(111). a) Molecular scheme of a GNR section with a radical. b) CO tip nc-AFM image of the GNR. c) CO tip STM constant height image at 1mV. The bright lobes indicate a current enhancement due to the presence of the Kondo resonance around the edge. d) dI/dV with a metallic tip taken on the edge of the GNR at different temperatures. The Kondo peak gets broadened as the temperature increases.

The spectroscopies yielded sharp peaks around 0 bias identified as Kondo resonances[95, 96] with a calculated Kondo temperature of $T_k = 35$ K[97], suggesting the presence of S=1/2 unpaired electrons at the GNR edges. No spectroscopy feature was found elsewhere on the GNR at <10 meV. To confirm the Kondo nature of the dI/dV peak, STS at different temperatures were performed to observe the broadening and final destruction of the Kondo resonance as the temperature increased (Fig. 3.1).

To further study the S=1/2 impurity at the edges of the GNR, it was probed with a functionalized nickelocene STM tip. Nickelocene molecules were dosed on the prepared sample at 2.8 K and picked up with the metallic tip as described in Section 2. $\mathrm{d^2I/dV^2(z)}$ was performed by varying the tip-sample distance at different positions on the GNR (Fig. 3.2). As expected, only those taken at the edge showed a renormalization of the nickelocene ±4 meV peaks as the tip got closer to the GNR. The evolution of the peaks with Z was rationalized by a two-site Hubbard model composed of the nickelocene's $3d^8$ shell and one half-filled orbital of the GNR. This model can be approximated to a two-site Heisenberg spin model as the charge transfer is negligible (this assumption will also be taken in the following systems). The proposed Heisenberg Hamiltonian is:

$$\hat{H} = D_{Ni}\hat{S}^2_{Ni,z} + J\vec{\hat{S}}_{Nc} \cdot \vec{\hat{S}}_{GNR} \tag{3.1}$$

The $dim = 6$ spin operators for nickelocene $\vec{\hat{S}}_{Nc}$ and the radical $\vec{\hat{S}}_{GNR}$ are:

$$\vec{\hat{S}}_{Nc} = \hbar(\hat{\sigma}^1_x \otimes I_2, \hat{\sigma}^1_y \otimes I_2, \hat{\sigma}^1_z \otimes I_2) = (\hat{S}_{Nc,x}, \hat{S}_{Nc,y}, \hat{S}_{Nc,z}) \tag{3.2}$$

$$\vec{\hat{S}}_{GNR} = \hbar(I_3 \otimes \hat{\sigma}^{1/2}_x, I_3 \otimes \hat{\sigma}^{1/2}_y, I_3 \otimes \hat{\sigma}^{1/2}_z) = (\hat{S}_{M,x}, \hat{S}_{M,y}, \hat{S}_{M,z}) \tag{3.3}$$

I_3, I_2 represent the identity matrices for spin dimensions 3 ($NiCp_2$) and 2 (GNR), and $\hat{\sigma}^1_{x,y,z}, \hat{\sigma}^{1/2}_{x,y,z}$ are the Pauli matrices for $S_{Nc} = 1, S_{GNR} = 1/2$. D_{Ni} is the nickelocene's

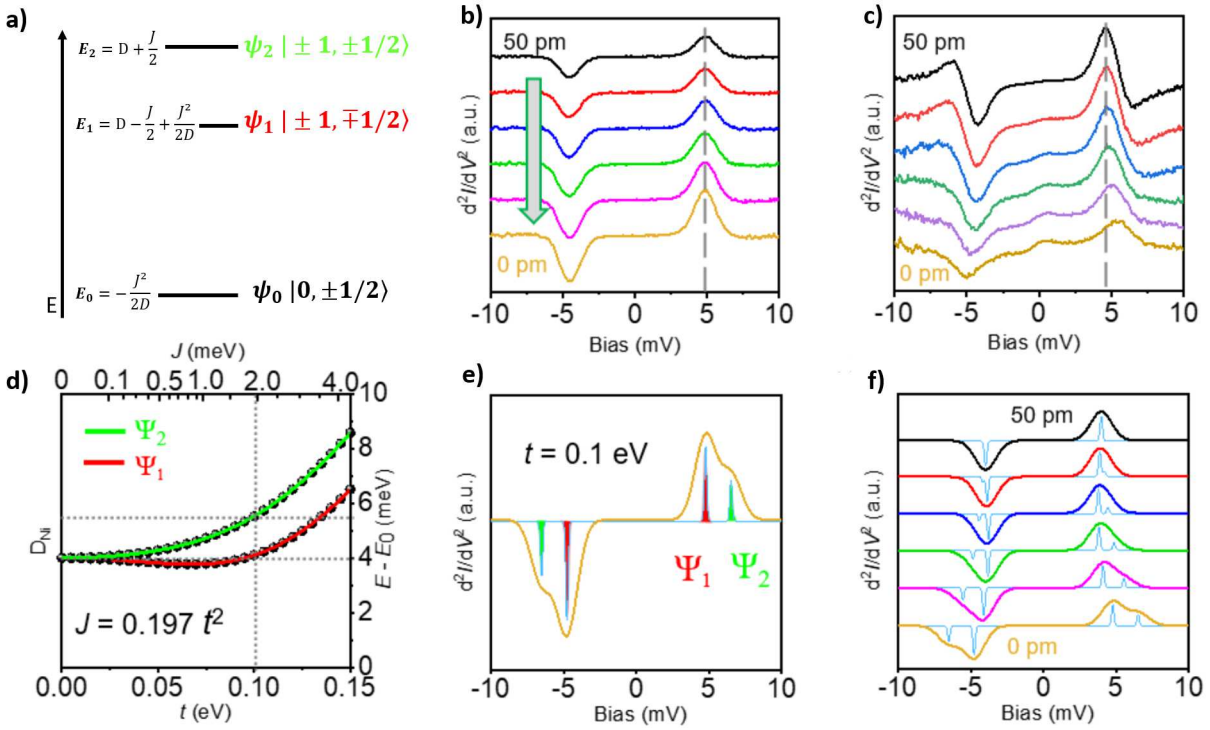

Figure 3.2: a) Approximated energies and eigenstates Ψ after diagonalizing the Heisenberg Hamiltonian. The exchange coupling parameter is $J(t)$ and D stands for the nickelocene's magnetic anisotropy (4 meV). b,c) Experimental $d^2I/dV^2(z)$ at the center (b) and the edge (c) of the GNR taken at different heights. Only c) exhibits renormalization as the tip gets closer to the sample. The matching colors indicate same spectroscopy height. d) Energy evolution of the Ψ_{0-1} (red) and Ψ_{0-2} (green) transitions as a function of the hopping parameter t with $J = 0.197t$. e) Calculated spectrum at $t = 0.1eV$ after adding thermal broadening with the assigned peaks with $J = 2$ meV. f) Calculated IETS at different t matching the experimental data in c).

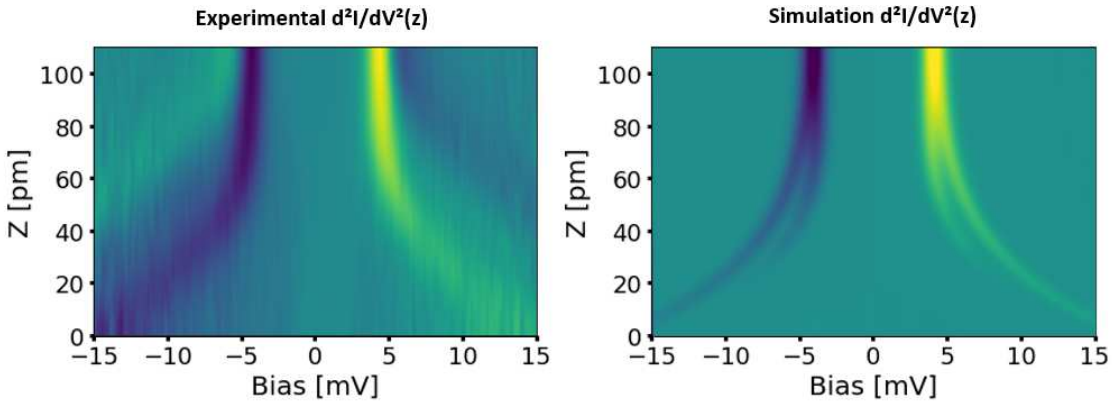

Figure 3.3: Experimental (left) and simulation (right) $d^2I/dV^2(z)$ with a nickelocene tip at different tip-sample distance on the S=1/2 edge of the GNR. The simulation parameters are: 2.5 K, $J = 10$ meV at the closest distance with a decay constant of $a = 3$ Åand 1:3 strength coupling favoring the GNR.

$S = 1$ out-of-plane magnetic anisotropy, and there is an inter-site hopping $t(z)$ and an exchange coupling parameter $J(t)$. The procedure involves diagonalization of the Heisenberg Hamiltonian to obtain the energy eigenvalues as a function of J and the tip-sample distance z. In this case, the diagonalization is exact, and six energies E and eigenfunctions Ψ are obtained for the nickelocene-GNR system as linear combinations of the basis $|m_{Nc}|m_{GNR}\rangle$: $(|1|1/2\rangle, |0|1/2\rangle, |-1|1/2\rangle, |1|-1/2\rangle, |0|-1/2\rangle, |-1|-1/2\rangle)$ (the basis vectors are implemented in this particular order by the Python script[76]). The evolution of the energies with z and the $d^2I/dV^2(z)$ simulations match perfectly with the experimental data by assuming $J = 0.197t^2$, confirming the $S_{GNR} = 1/2$ magnetic character of the edge states (Fig. 3.2). Another test was run using the Python script that includes the cotunneling theory to simulate the $d^2I/dV^2(z)$ along the Heisenberg model (Fig. 3.3) to showcase the agreement with the experimental data.

3.1.2 Highly-Entangled Polyradical Nanographene with Coexisting Strong Correlation and Topological Frustration

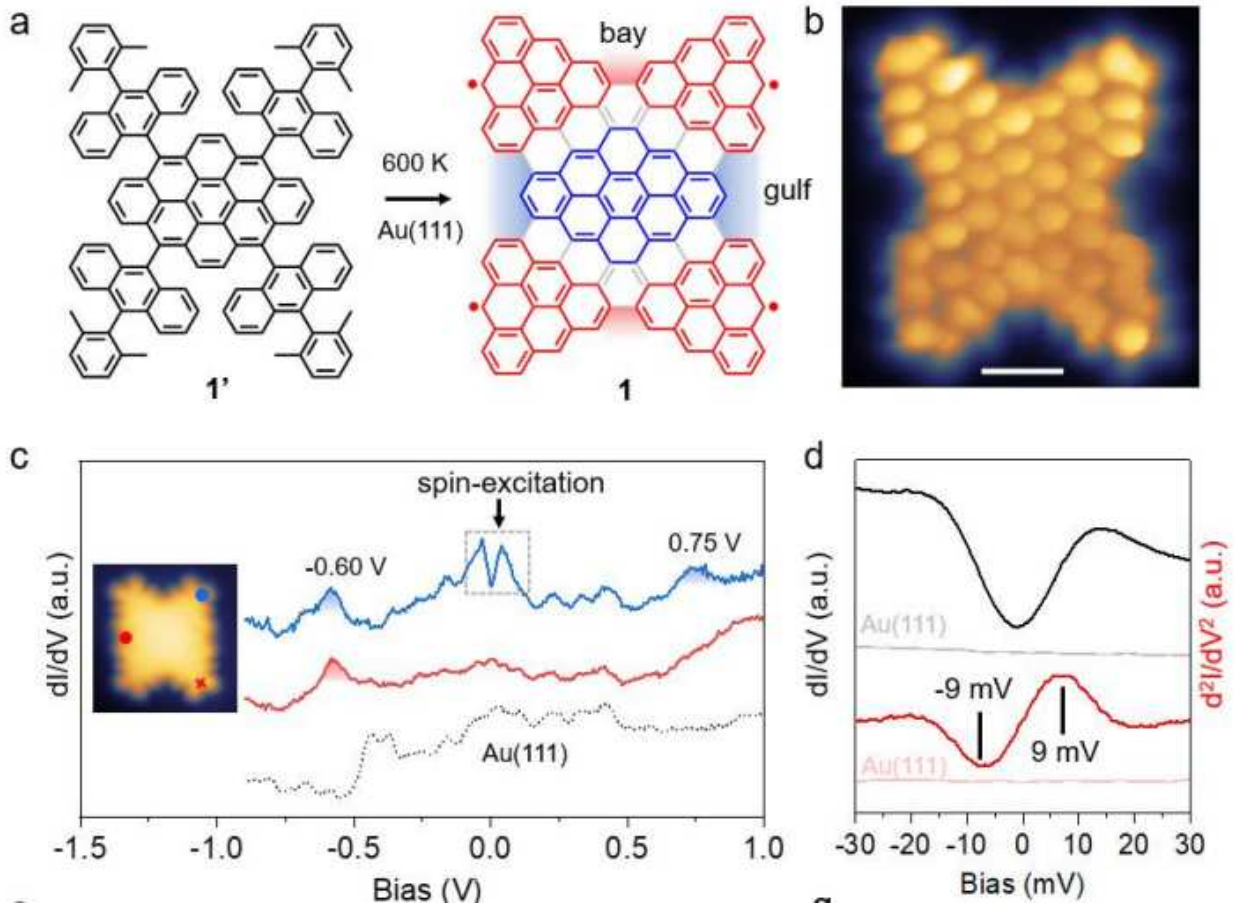

Figure 3.4: a) Precursor and OSS of the final product. b) Constant height STM image with a CO tip taken at 20mV. c) dI/dV with metallic tip performed at the positions marked over the molecule. d) d^2I/dV^2 IETS with a metallic tip at a corner site of the molecule.

In this work[78], a nanographene molecule is designed by fusing triangulene and rhombene molecules via on-surface synthesis (OSS) to obtain a polyradical graphene butterfly-shaped molecule. Its polyradical nature arises from the mix of topological frustration and electron-electron interaction simultaneously, which results in a tetraradical nanographene whose π-electrons are highly correlated. The precursor consists of a rhombene core decorated with four 9-(2,6-dimethylphenyl)anthryl groups at four zigzag edges. After depositing

the precursor by Knudsen-cell evaporation in ultra-high vacuum (UHV) on the Au(111) substrate, it undergoes a 600 K annealing to start the cyclodehydrogenation and synthesize the final product. STS characterization with a metallic tip yielded two prominent features at -0.6 and 0.75 eV in the dI/dV localized on the edges of the graphene butterfly, and another two close to the Fermi energy. A closer look via d^2I/dV^2 revealed two peaks at ±9 meV that were assigned to a spin-flip excitation (Fig. 3.4), in agreement with theoretical many-body calculations using the complete active space self-consistent field (CASSCFN)[98] as DFT is not appropriate for strongly correlated polyradical systems. The calculations yield a highly correlated S=0 singlet ground state and a S=1 triplet excited state separated by ≈ 9 meV.

In order to corroborate these assumptions, the butterfly was IETS probed with a nickelocene tip by performing $d^2I/dV^2(z)$ at different tip-sample distances at 1.3 K (Fig. 3.6). Spectroscopies taken over the corners of the molecule yielded a ±13 meV feature besides the nickelocene's ±4 meV when the tip-sample distance was large and the exchange coupling between the butterfly and the molecule was negligible. In this regime, the IETS ±13 meV peaks correspond to the inelastically lost energy of a tunneling electron that excites both spin-flips from the nickelocene (4 meV) and the molecule (9 meV), confirming the previous results. As the $NiCp_2$ tip is brought closer to the butterfly corners, the J starts renormalizing the spectrum.

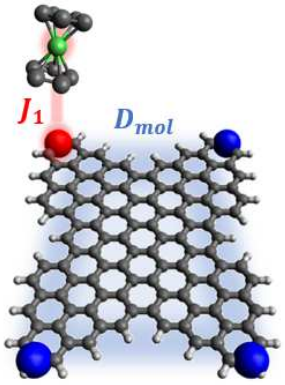

Figure 3.5: Representation of a butterfly molecule probed with a nickelocene. J_1 represents the exchange coupling of the nickelocene with one of the radicals (red) and D_{mol} accounts for the effective exchange coupling of the four radicals (red+blue).

A Heisenberg Hamiltonian is proposed to study the combined nickelocene-butterfly system. As the four electrons are ferro- and antiferromagnetically coupled, we assumed

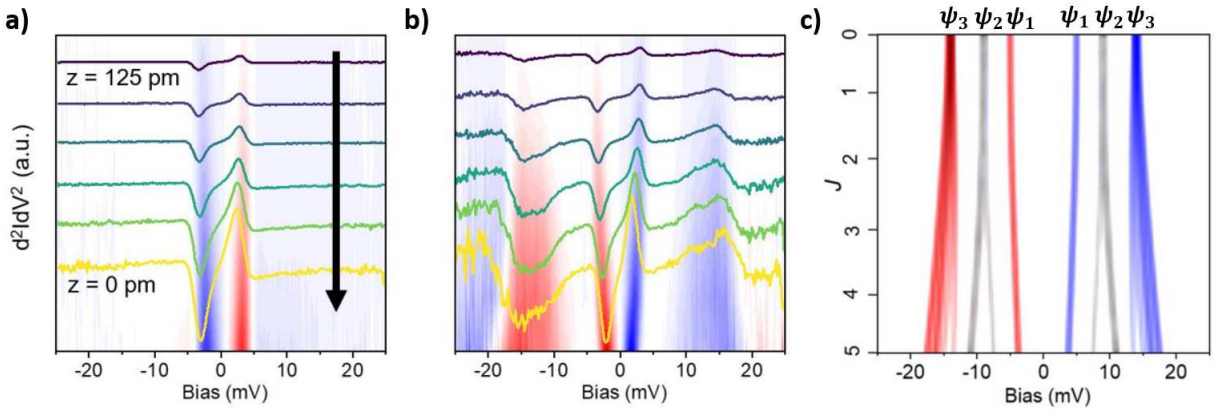

Figure 3.6: $d^2I/dV^2(z)$ maps at different tip-sample distances with a nickelocene functionalized tip with a 25 pm decrease step over bare Au(111) (a), on the butterfly edge (b) and the simulation from the Heisenberg Hamiltonian energy evolution as a function of $J(z)$. The only visible transitions correspond to the ones from Ψ_0 to Ψ_1, Ψ_3. Ψ_{0-2} is not visible in the experiment.

the nickelocene to exchange couple with only one radical on the probed corner, whose interaction is governed by the $J(z)$ term and has a $S_1 = 1/2$. Another effective interaction term encapsulates the coupling between the radicals themselves as an out-of-plane magnetic anisotropy D_{mol} factoring the square of the molecule's spin operator in the Z direction with $S_{mol} = 1$ (Fig. 3.5):

$$\hat{H} = D_{Nc}\hat{S}^2_{z,Nc} + D_{mol}\hat{S}^2_{z,mol} - J\vec{\hat{S}}_{Nc} \cdot \vec{\hat{S}}_1 \tag{3.4}$$

The $dim = 18$ spin operators for nickelocene $\vec{\hat{S}}_{Nc}$, the molecule $\vec{\hat{S}}_{mol}$ and the corner electron $\vec{\hat{S}}_1$ are:

$$\vec{\hat{S}}_{Nc} = \hbar(\hat{\sigma}^1_x \otimes I_3 \otimes I_2, \hat{\sigma}^1_y \otimes I_3 \otimes I_2, \hat{\sigma}^1_z \otimes I_3 \otimes I_2) = (\hat{S}_{Nc,x}, \hat{S}_{Nc,y}, \hat{S}_{Nc,z}) \tag{3.5}$$

$$\vec{\hat{S}}_{mol} = \hbar(I_3 \otimes \hat{\sigma}^1_x \otimes I_2, I_3 \otimes \hat{\sigma}^1_y \otimes I_2, I_3 \otimes \hat{\sigma}^1_z \otimes I_2) = (\hat{S}_{mol,x}, \hat{S}_{mol,y}, \hat{S}_{mol,z}) \tag{3.6}$$

$$\vec{\hat{S}}_1 = \hbar(I_3 \otimes I_3 \otimes \hat{\sigma}_x^{1/2}, I_3 \otimes I_3 \otimes \hat{\sigma}_y^{1/2}, I_3 \otimes I_3 \otimes \hat{\sigma}_z^{1/2}) = (\hat{S}_{1,x}, \hat{S}_{1,y}, \hat{S}_{1,z}) \tag{3.7}$$

I_3, I_2 represent the identity matrices for spin dimensions 3 ($NiCp_2$, butterfly) and 2 (radical), and $\hat{\sigma}^1_{x,y,z}, \hat{\sigma}^{1/2}_{x,y,z}$ are the Pauli matrices for $S_{Nc} = S_{mol} = 1, S_1 = 1/2$. D_{Ni}, D_{mol} are the nickelocene's and the butterfly magnetic anisotropy, and there is an inter-site hopping $t(z)$ and an exchange coupling parameter $J(t)$. The procedure again involves diagonalization of the Heisenberg Hamiltonian to obtain the energy eigenvalues as a function of J and the tip-sample distance z. The simulation from the diagonalized Heisenberg Hamiltonian shown in Fig. 3.6 reflects the evolution of the nickelocene and molecule $\mathrm{d^2I/dV^2}$ peaks as the tip gets closer to the butterfly. The most relevant states $|m_{Nc}|m_{mol}\rangle$ for the transitions from the ground state $\Psi_0 = |0|0\rangle$ are $\Psi_1 = |\pm 1|0\rangle, \Psi_2 = |0|1\rangle, \Psi_3 = |\pm 1|1\rangle$. While transitions Ψ_{0-1}, Ψ_{0-3} are present in the experimental maps, Ψ_{0-2} predicted at ± 9 meV is invisible. Further analysis implementing the cotunneling theory or varying the strength of the couplings did not explain the absence of this transition, which will be examined closely in the future.

3.2 1D Magnetic Polymers

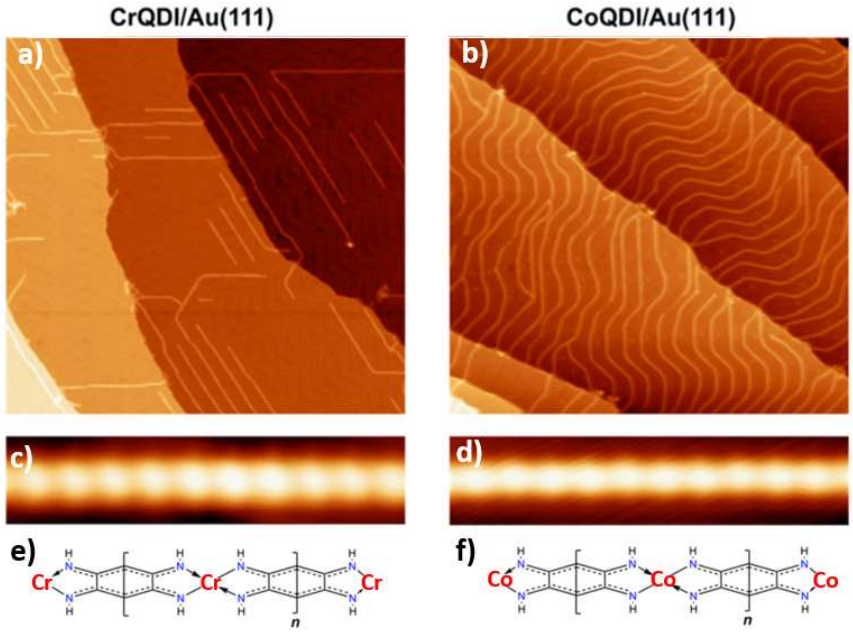

Figure 3.7: STM images of CrQDI a,c) and CoQDI b,c) chains on Au(111)[99]. Scan size: a,b) 200x200 nm^2 c,d) 8x2 nm^2. Scanning parameters: a) 100 mV, 30 pA, b) 350 mV, 30 pA c) 30 mV, 10 pA, d) -400 mV, 32 pA. e,f) correspond with the molecular diagram for both CrQDI and CoQDI respectively.

1D organometallic chains are a category of molecular nanomagnets suitable for constructing single-chain magnets by altering its metallic centers to vary its magnetic properties [100–105]. In particular, the synthesis of >100 nm long polymers consisting of transition metals (Fe,Ni,Cr,Co) linked by 2,5-diamino-1,4-benzoquinonediimine (QDI) on Au(111) has been demonstrated by Santhini *et.al.*[99] (Fig. 3.7). These polymers exhibit interesting magnetic properties. In this work[79], we prepared the Co and Cr derivatives to perform a combination of averaging spectroscopic techniques (XAS, XLD and XMCD), density functional theory (DFT) calculations, and IETS with metallic and nickelocene STM tips were utilized to extract the spin multiplicity, magnetic anisotropy and another extra magnetic features. The sample preparation was identical as the utilized by Santhini *et.al.*[99], consisting on a codeposition of the QDI precursor (heated at 385 K in a Knudsen cell) and

a)

metal atom	3d occupation	spin state	m_s (μ_B)	m_l (μ_B)	easy axis
Co	$3d^7$	1.47 ≅ 3/2 (HS)	2.94	1.79	Y
Cr	$3d^4$	4/2 (HS)	4	0.05	Z

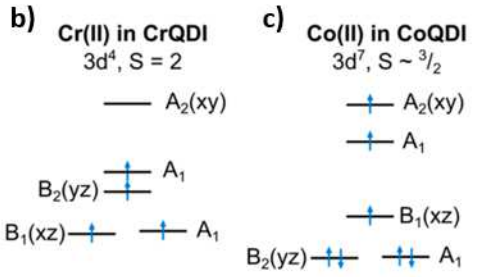

Figure 3.9: a) Magnetic properties from XAS/XLD. b,c) energy diagrams of the Cr(II),Co(II) ionic metal centers. Y=in plane, Z=out of plane. m_s, m_l correspond with the z component of the spin and the orbital momentum in μ_b units (Bohr magneton).

the metal atom (Co or Cr) onto the Au(111) substrate at 570 K. The XAS/XLD data processed with the optimized multiplet software MultiX[100] yields the magnetic properties shown in Fig. 3.9a). Both derivatives have the (II) ionic metal centers in a $3d$ occupation and a high spin configuration: $S_{Co} \approx 3/2$ and $S_{Cr} = 2$.

After acquiring information with the averaging techniques, STS at 1.2 K and UHV conditions were performed to measure electronic and magnetic features with atomic precision. Fig. 3.8 shows dI/dV curves measured with a metallic tip over the metal centers and the substrate. While the spectroscopy over the Co atom is featureless, the STS over the Cr shows a peak around zero bias corresponding to an unscreened Kondo effect[95, 96], a consequence of the calculated $S_{Cr} = 2$ high spin of the Cr atom on the chain with a $T_k = 21.9$ K obtained after fitting with the Frota function [106–108]. To obtain more magnetic information, IETS with the nickelocene STM tip were performed over the metal centers and linkers.

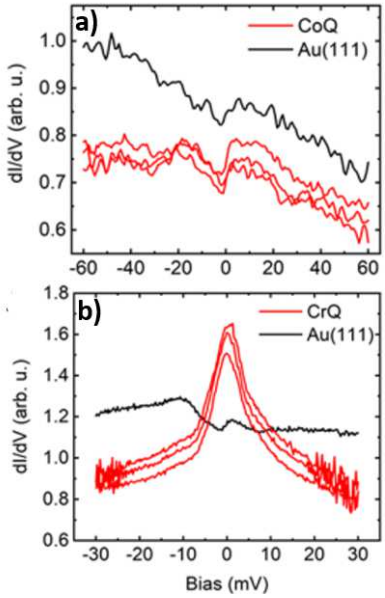

Figure 3.8: dI/dV with a metallic tip over the metal centers (red) and Au(111) (black). a) CoQDI b) CrQDI (Kondo feature around 0 bias).

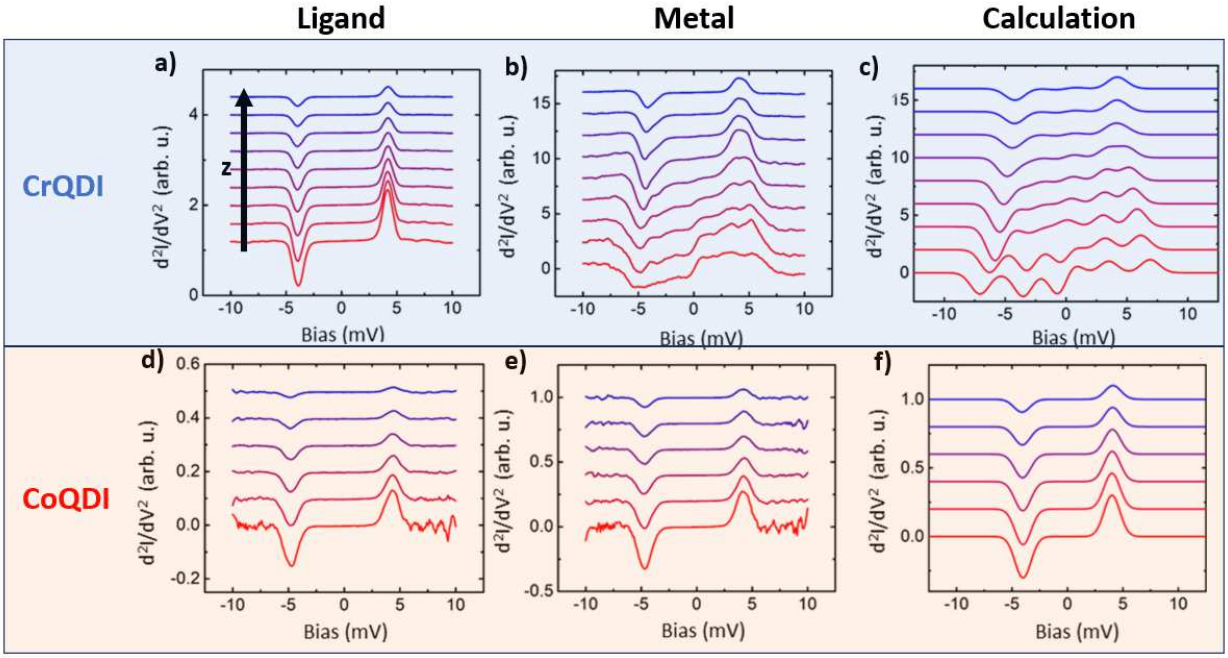

Figure 3.10: $dI^2/dV^2(z)$ with a nickelocene tip at different tip sample distance (red=closer, blue=farther) over the ligand (a,d) and the metal centers (b,e). (c,f) correspond to the simulated dI^2/dV^2 after fitting the curves and performing the calculations taking into account the crystal field from the multiplet model fitted from the x-ray data, the Heisenberg Hamiltonian and the cotunneling theory.

$dI^2/dV^2(z)$ were taken at different heights in a bias

range of ±10 mV (Fig. 3.10). No feature other than the ±4 mV peaks from the nickelocene's magnetic anisotropy D_{NiCp_2} were found when probing over the ligand sites in both chains, as expected. The spectrum only changed over the Cr sites; no renormalization was found when approaching with the nickelocene over the Co sites. This absence of interaction between the nickelocene and the in-plane magnetism of the Co atom is due to two contributing factors. First, the calculated in-plane magnetic anisotropy of the CoQDI chain is $E_{Co} = 37$ meV, much higher compared to the out-of-plane D_{NiCp_2} so the spin states of the compound system are out of the probed energy range. Secondly, the high in-plane magnetization locks up the spin parallel to the sample surface, orthogonal to the out-of-plane excited state of the nickelocene, making the exchange coupling negligible. In order to understand the experimental results from the CrQDI chain, we utilized a Heisenberg Hamiltonian:

$$\hat{H} = D_{Nc}\hat{S}^2_{z,Nc} + D_{Cr}\hat{S}^2_{Cr} - J\vec{\hat{S}}_{Nc} \cdot \vec{\hat{S}}_{Cr} \tag{3.8}$$

Where $D_{Nc} = 4$ meV, D_{Cr} is the out-of-plane magnetic anisotropy of the Cr center, $J(t)$ is the exchange coupling parameter as a function of t, and the spin operators are $\vec{\hat{S}}_{Nc} = (\hat{S}_{x,Nc}, \hat{S}_{y,Nc}, \hat{S}_{z,Nc})$ and $\vec{\hat{S}}_{Cr} = (\hat{S}_{x,Cr}, \hat{S}_{y,Cr}, \hat{S}_{z,Cr})$ for the nickelocene and the Cr site respectively, with $S_{Nc} = 1$ and $S_{Cr} = 2$. Fitting the $d^2I/dV^2(z)$ data, we obtained $D_{Cr} \approx -0.23$ meV and $J \approx 0.0975t$, where $t(z)$ is the hopping parameter related to the tip-sample distance Z as shown in Fig. 3.11. The value of D_{Cr} extracted from the fitting is different in module and sign compared to the $D_{Cr} \approx 4$ meV obtained from the XAS/XLM fitting. This can be attributed to the atomic sensitivity to the IETS on the metal centers compared to the averaging methods that measure the magnetism of the whole polymer, and some antiferromagnetic interaction may be present when probing with the nickelocene tip that would change the anisotropy's sign. Fig. 3.11 describes the eigenstates of the

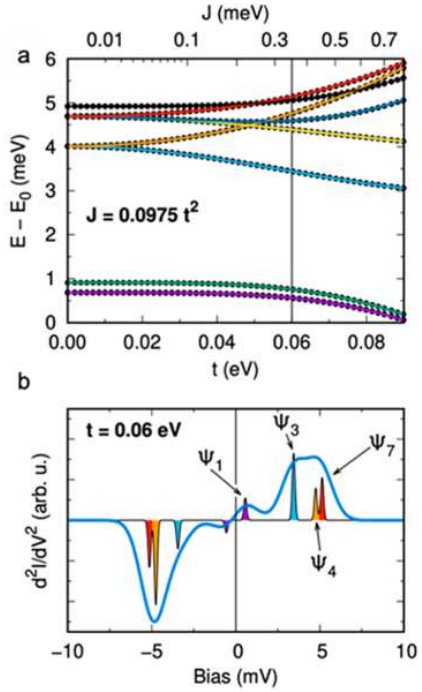

c

state	M_{Ni}	M_{Cr}	M_{tot}	Energy (keeping terms up to J^2)
Ψ_8	±1	0	±1	$D_{Ni} + \frac{3J^2}{D_{Ni} - D_{Cr}}$
Ψ_7	±1	±1	±2	$D_{Ni} + D_{Cr} + J + \frac{2J^2}{D_{Ni} - 3D_{Cr}}$
Ψ_6	±1	±1	0	$D_{Ni} + D_{Cr} - J + \frac{6J^2}{D_{Ni} + D_{Cr}}$
Ψ_5	±1	±1	0	$D_{Ni} + D_{Cr} - J$ (exact)
Ψ_4	±1	±2	±3	$D_{Ni} + 4D_{Cr} + 2J$ (exact)
Ψ_3	±1	±2	±1	$D_{Ni} + 4D_{Cr} - 2J + \frac{2J^2}{D_{Ni} + 3D_{Cr}}$
Ψ_2	0	0	0	$-\frac{6J^2}{D_{Ni} + D_{Cr}}$
Ψ_1	0	±1	±1	$D_{Cr} - \left(\frac{3}{D_{Ni} - D_{Cr}} + \frac{2}{D_{Ni} + 3D_{Cr}}\right)J^2$
Ψ_0	0	±2	±2	$4D_{Cr} - \frac{2J^2}{D_{Ni} - 3D_{Cr}}$

Figure 3.11: (a) Evolution of the combined nickelocene-metal center state energies respect to the ground state E_0 as a function of the hopping parameter t calculated with the Heisenberg model. Colors in (a) correspond to the colors in (c). (b) Calculated $d^2\,I/dV^2$ broadened spectrum of the NiCp2 tip on a Cr atom for $t = 0.06$ eV with the assigned individual peaks. (c) Eigenstates and energies of the Heisenberg model of the coupled system of the nickelocene tip and CrQDI metal center.

diagonalized Heisenberg Hamiltonian as a function of J, D_{Nc}, D_{Cr} keeping the J terms to J. Note that the allowed transitions are $\Psi_{0-1,3,4,7}$ by the selection rules.

3.3 2D Magnetic Materials

2D magnetic states in layered van der Waals compounds[109–111] exhibit robust magnetic properties[112–115], protected from spin fluctuations that usually disrupt the 2D magnetic order. Moreover, these materials have proven to have tunable magnetism and are adequate for STM characterization as they have been sublimated by Knudsen-cell evaporation in homogeneous layers[114, 115]. In this work yet to be published, we studied metallic chlorides whose magnetic order persists even on a metallic substrate and can be altered from perpendicular to in-plane by substituting the metal ion, in particular $FeCl_2$ and $NiCl_2$.

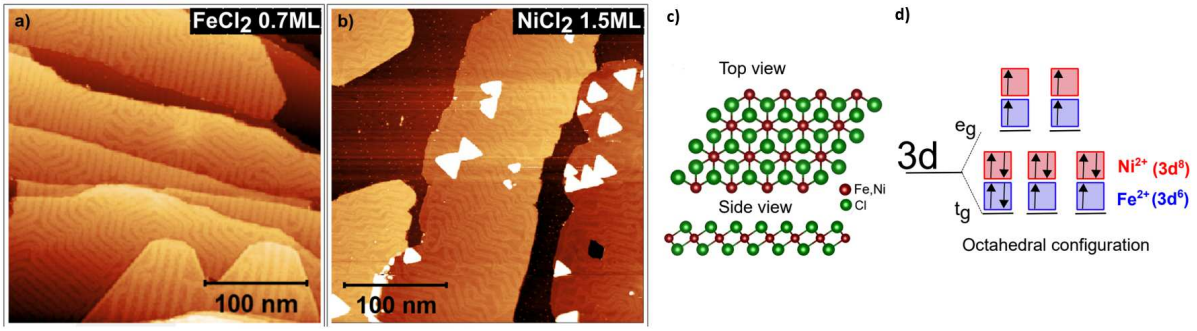

Figure 3.12: STM images of the dihalides on Au(111). (a) Submonolayer coverage of $FeCl_2$ (20 pA, 3 V). (b) 1.5 monolayers of $NiCl_2$ (10 pA, 2 V). (c) Atomic structure of the dihalides. The metal ions (red) are embedded in the Cl lattice (green) in octahedral coordination. (d) Energy diagram showing the splitting caused by the octahedral crystal field from the triply-degenerate t_g (d_{xy}, d_{xz}, d_{yz}) states of $FeCl_2$ (blue) and the doubly-degenerate e_g ($d_{x^2y^2}$, d_{z^2}) states of $NiCl_2$ (red).

Both dichlorides have different magnetic properties due to their distinct crystal field. This affects the metal ions: the Fe^{2+} has $S = 2$ with a mild out-of-plane magnetic anisotropy, and Ni^{2+} has $S = 1$ and has in-plane magnetic anisotropy[116, 117] (Fig. 3.12). After depositing the dicholirdes under UHV conditions on two different Au(111) samples, they underwent extensive characterization by means of STM/nc-AFM, high-resolution X-ray Photoelectron spectroscopy (HR-XPS), angle-resolved photoemission spectroscopy (ARPES), X-ray absorption spectra (XAS), and X-ray magnetic circular dichroism (XMCD).

$TMCl_2$	$B^{\perp}$ (T)	$B^{\parallel}$ (T)	MAE (meV)
$FeCl_2$	0.68	0.27	0.13
$NiCl_2$	0.37	0.68	-0.072

Figure 3.13: Experimental values of the magnetic field $\vec{B}$ for saturation in the XMCD magnetization loops.

From this characterization, we confirmed the correct growth of the dicholirdes' 2D structure, forming a monolayer on the Au(111) substrate with low electronic interaction. (Fig. 3.12) The antiferromagnetic order was confirmed in both materials after processing the experimental data, confirming the spin of both metal ions in the material as $S_{NiCl_2} = 1$ and $S_{FeCl_2} = 2$. Calculations from the XMCD experiment showed that both materials are magnetically soft, reaching magnetization saturation at <1 T. It also confirmed the out-of-plane magnetic anisotropy of $FeCl_2$, and the in-plane magnetic anisotropy of $NiCl_2$. Nevertheless, the magnetization of $NiCl_2$ turns to out-of-plane after saturation under a magnetic field of 0.65 T perpendicular to the sample.

All the magnetic characterization techniques employed to obtain these values are averaging techniques. A more detailed and local characterization of the dihalides was performed by probing them with the nickelocene functionalized tip.

The experimental procedure was identical to that in the previous sections, carried out at 4 K, after testing the nickelocene tip on Au(111) to ensure no contamination and checking for the expected ±4 meV peaks. Fig. 3.14 shows the experimental $d^2I/dV^2(z)$ at different heights with a metallic tip on top of the metallic ions of $FeCl_2$ and $NiCl_2$ (bright blobs in the STM contrast). In the case of $FeCl_2$, both sets of curves show a symmetric splitting of the nickelocene's ±4 mV peaks as the tip approaches the surface, and it does so with and without applying a perpendicular magnetic field of 3 T. For $NiCl_2$, the spectra behave quite differently. The nickelocene peaks do not split in the absence of a magnetic field but get slightly separated in energy as the tip approaches the surface. When the

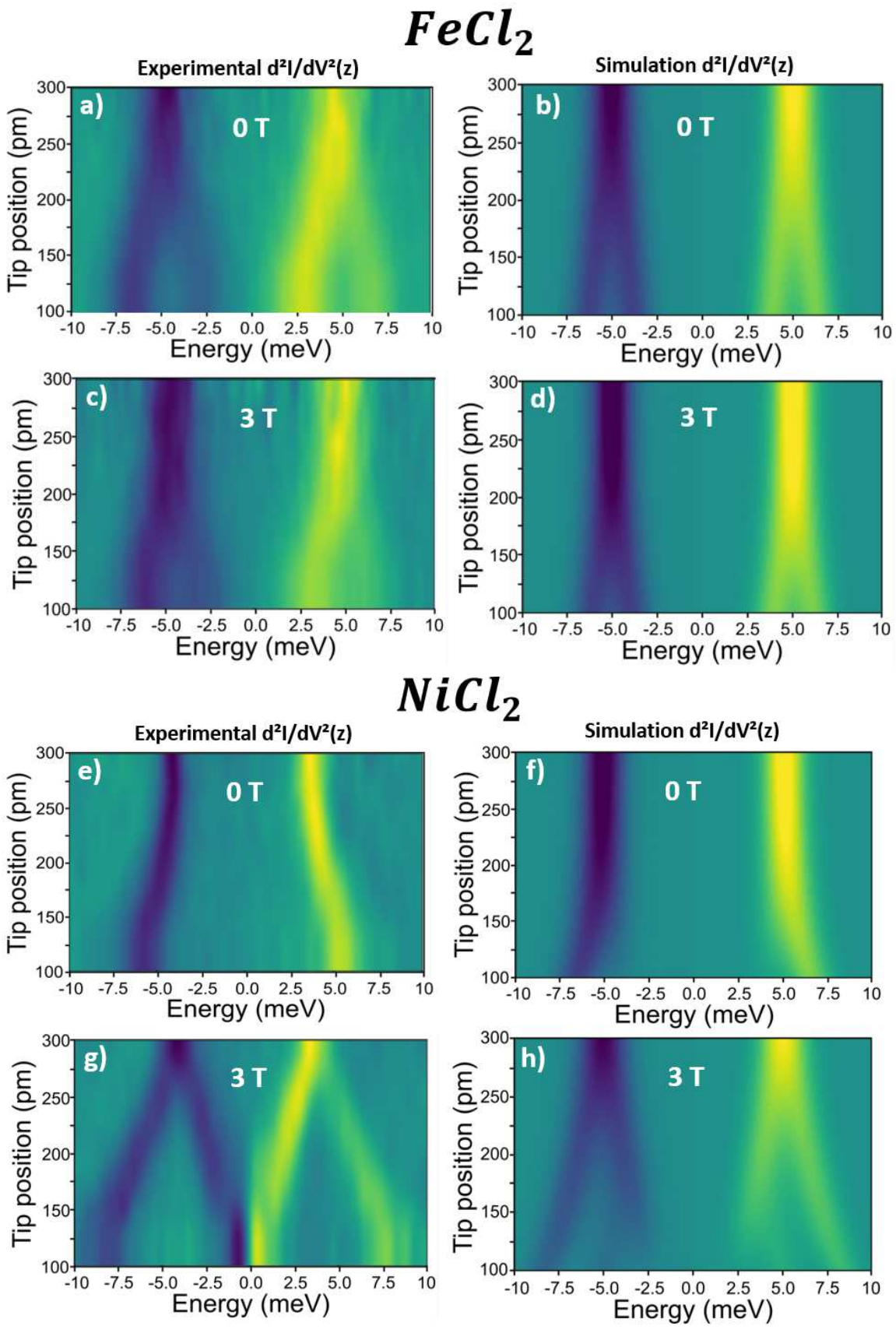
$FeCl_2$
Experimental d²I/dV²(z)
Simulation d²I/dV²(z)
a)
0 T
b)
0 T
c)
3 T
d)
3 T
$NiCl_2$
Experimental d²I/dV²(z)
Simulation d²I/dV²(z)
e)
0 T
f)
0 T
g)
3 T
h)
3 T
Tip position (pm)
Energy (meV)
300
250
200
150
100
-10 -7.5 -5.0 -2.5 0.0 2.5 5.0 7.5 10

Figure 3.14:

Figure 3.14: Experimental (a,c,e,g) and simulated (b,e,f,h) $\mathbf{d^2I/dV^2}$(z) maps over the dihalide metal ions ($Fecl_2$:[a-d], $NiCl_2$:[e-h]) with a nickelocene tip at different tip-sample distances (same for all the maps), starting 100 pm from the dihalide's surface and lifting the tip up to 300 pm relative to the surface. Each IETS curve is separated by 20 pm in height. The color scale indicates higher positive (yellow) or lower negative (blue) $\mathbf{d^2I/dV^2}$ values. A magnetic field $B_z = 3$ T was applied in (c,d,g,h). The simulations are also performed from 100 to 300 pm tip-sample distance, matching the tip-lift from the experiments. The Heisenberg Hamiltonian from 3.9, the cotunneling theory and a dipolar field from the six neighboring atoms (Fig. 2.9) are utilized to model the IETS. The anisotropy used in the simulations is detailed in Table 3.1. The exchange coupling constant $J(z)$ considered for $FeCl_2$ is 2.7 meV and 3.5 meV for $NiCl_2$ at the closest distance, with a decay constant of the exchange coupling with height of $a = 0.9$ Å. The dipolar field interaction was modeled after considering six hexagonal sites single occupied separated by 3.4Å. The simulated temperature is 4 K with a 1:3 coupling strength favoring the dihalides.

	0 T	**3 T**
$FeCl_2$	[0,0,0.13]	[0,0,0.13]
$NiCl_2$	[-0.072,0,0]	[0,0,-0.072]

Table 3.1: Magnetic anisotropy $[E_x, E_y, D_z]$ in meV for the different dihalides and B_z taken for the simulation using the XMCD values (Fig. 3.13).

perpendicular magnetic field is active, the spectra completely change, showing a stronger splitting than in the $FeCl_2$ case, indicating full magnetization and a change in the magnetic moment direction from parallel to perpendicular to the sample. To explain these results, a Heisenberg Hamiltonian is proposed:

$$\hat{H} = g\mu_B B_z \hat{S}_{z,MCl_2} + D_{Nc}\hat{S}^2_{z,Nc} + D_{MCl_2}\hat{S}^2_{z,MCl_2} + E_{MCl_2}(\hat{S}^2_{x,MCl_2} - \hat{S}^2_{y,MCl_2}) + J\vec{\hat{S}}_{Nc}\cdot\vec{\hat{S}}_{FeCl_2} \tag{3.9}$$

Where the first term accounts for the Zeeman splitting as described in Section 2. $\vec{\hat{S}}_{MCl_2} = (\hat{S}_{x,MCl_2}, \hat{S}_{y,MCl_2}, \hat{S}_{z,MCl_2})$ is the spin operator for each corresponding dihalide ($S_{FeCl_2} = 2, S_{NiCl_2} = 1$) (remember $dim(\hat{S}_{x,y,z}) = 3 \cdot dim(\sigma_{Pauli})$). D_{MCl_2}, D_{Nc} are the nickelocene's and the dihalide's out-of-plane magnetic anisotropy and E_{MCl_2} is the dihalide's in-plane magnetic anisotropy, only active for the $B_z = 3$ T $NiCl_2$ case. The magnetic

anisotropies were utilized as shown in Table 3.1. The simulations run using the Heisenberg model are in good agreement with the experimental data for $NiCl_2$ without B_z (in-plane magnetic anisotropy). Nevertheless, this model fails to describe the d^2I/dV^2 renormalization on $FeCl_2$ as an exchange coupling alone. An extra contribution was proposed as a dipolar magnetic field[27] (see Theoretical Framework) in order to account for the discrepancy with the Heisenberg model in this particular case.

Fig. 3.14 shows the comparison between experimental $d^2I/dV^2(z)$ maps and the simulation, in agreement between each other. In this particular system, the nickelocene functionalization was uitilized to obtain some more magnetic features from the dihalides. As shown in Fig. 3.12, the monolayer of both $FeCl_2$ and $NiCl_2$ presents some corrugations visible on the STM images. $d^2I/dV^2(z)$ maps with the nickelocene in different locations of a grid at the same tip-sample distances over the $FeCl_2$ show the unequal splitting of the nickelocene's IETS peaks, which is a proof of some magnetic inhomogeneity on the surfaces (Fig. 3.15).

The nickelocene tip also offered a direct proof of the magnetic saturation of the $NiCl_2$ surface under a variable magnetic field. In this experiment, the tip was allocated on top of a Ni atom of the lattice and $d^2V/dI^2(B)$ were recorded at the same position and height while increasing the B_z perpendicular to the sample (Fig. 3.16). From 0-0.5 T, the magnetic anisotropy of the surface remained in-plane, and the nickelocene's spectrum barely changes, definitely no splitting was recorded as the in-plane magnetism is perpendicular to the out-of-plane magnetic anisotropy of the nickelocene considerably reducing the exchange coupling. When the threshold 0.65 T is reached, the $NiCl_2$ magnetic anisotropy turns to out-of-plane, aligned with the nickelocene's and inducing a strong split that remains constant as the magnetic field increases. This is in complete agreement with the results from the XMCD and another interesting application of the nickelocene tip for characterizing magnetic systems.

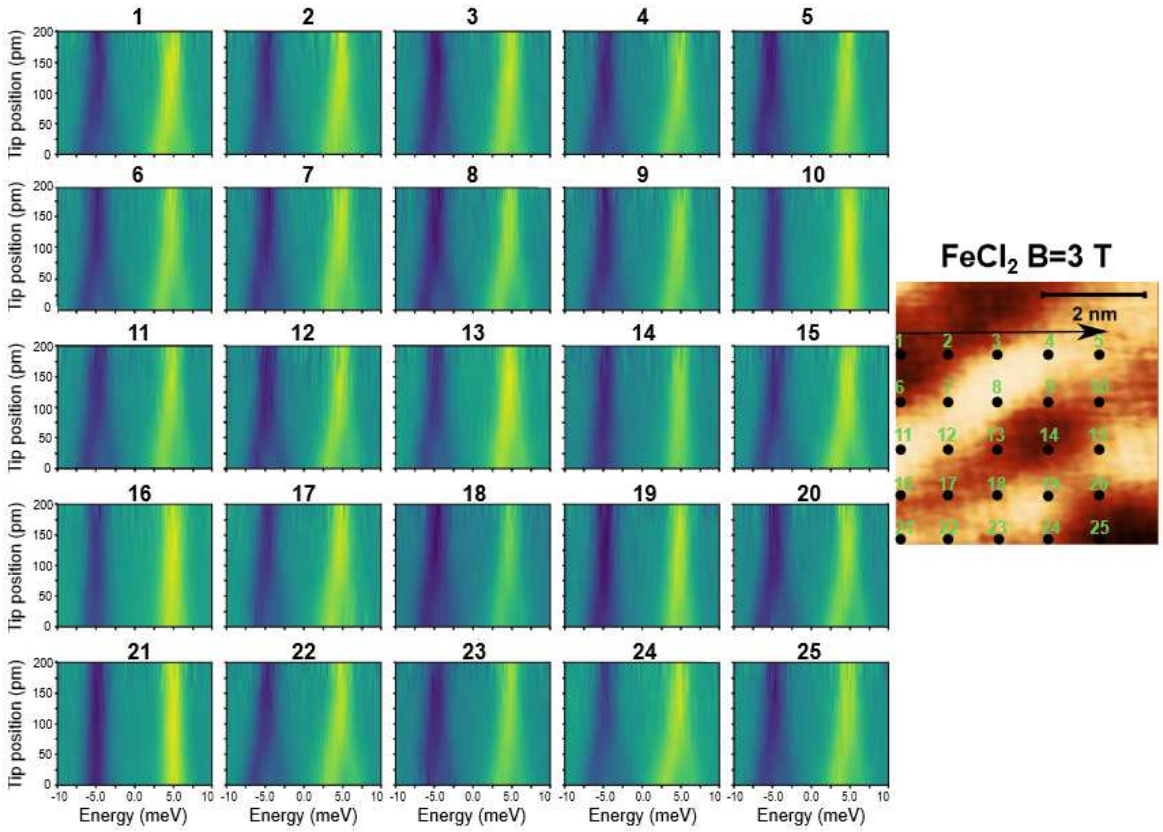

Figure 3.15: Experimental Nickelocene tip IETS at different positions on the $FeCl_2$ at an external magnetic field of 3 T. The $d^2I/dV^2(z)$ show a position dependent splitting. All $d^2I/dV^2(z)$ maps were taken starting from the same tip-sample distance determined by ncAFM. Right: STM image with a metallic tip of the $FeCl_2$ indicating each IETS location (10 pA, 10.4 mV).

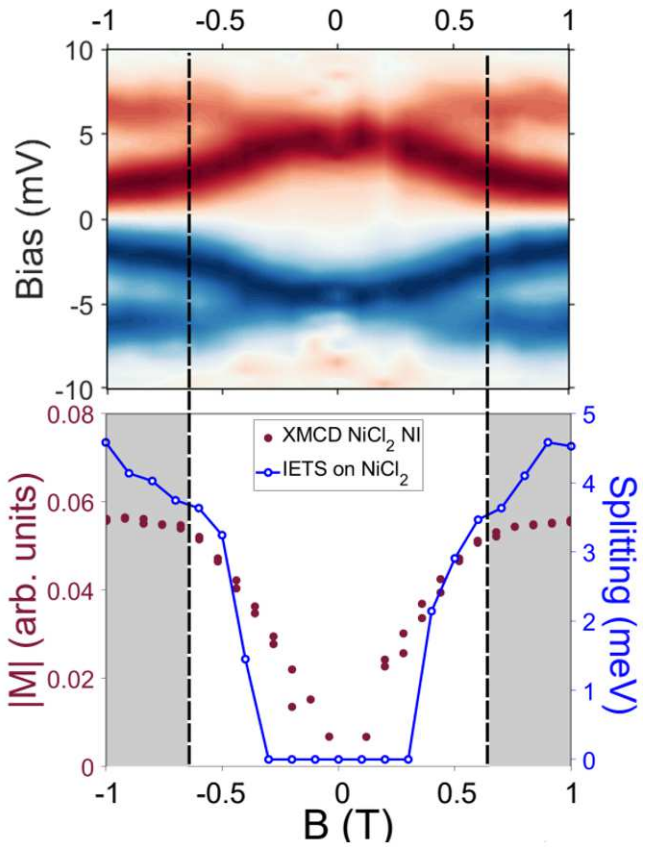

Figure 3.16: Top: $d^2I/dV^2(B_z)$ nickelocene tip map as a function of the magnetic field, ramping from -1 T to 1 T in 0.1 T steps taken at the same Ni atom and same height (red=positive, blue=negative IETS). Bottom: a comparison between the absolute value of magnetization with respect to the external magnetic field, in normal incidence (NI) (red dots), and the absolute value of the splitting of the nickelocene's IETS peaks (blue line). Saturation reached at 0.65±0.1 T.

As a final remark, Fig. 3.17 shows the Z spectroscopy recorded with a nickelocene tip for every map in Fig. 3.14 to ensure the same tip lifting after compressing the $NiCp_2$ onto the surface and reach the repulsion regime (positive values of frequency shift). The curves recorded demonstrates the controlled and reproducible behavior of the nickelocene tip.

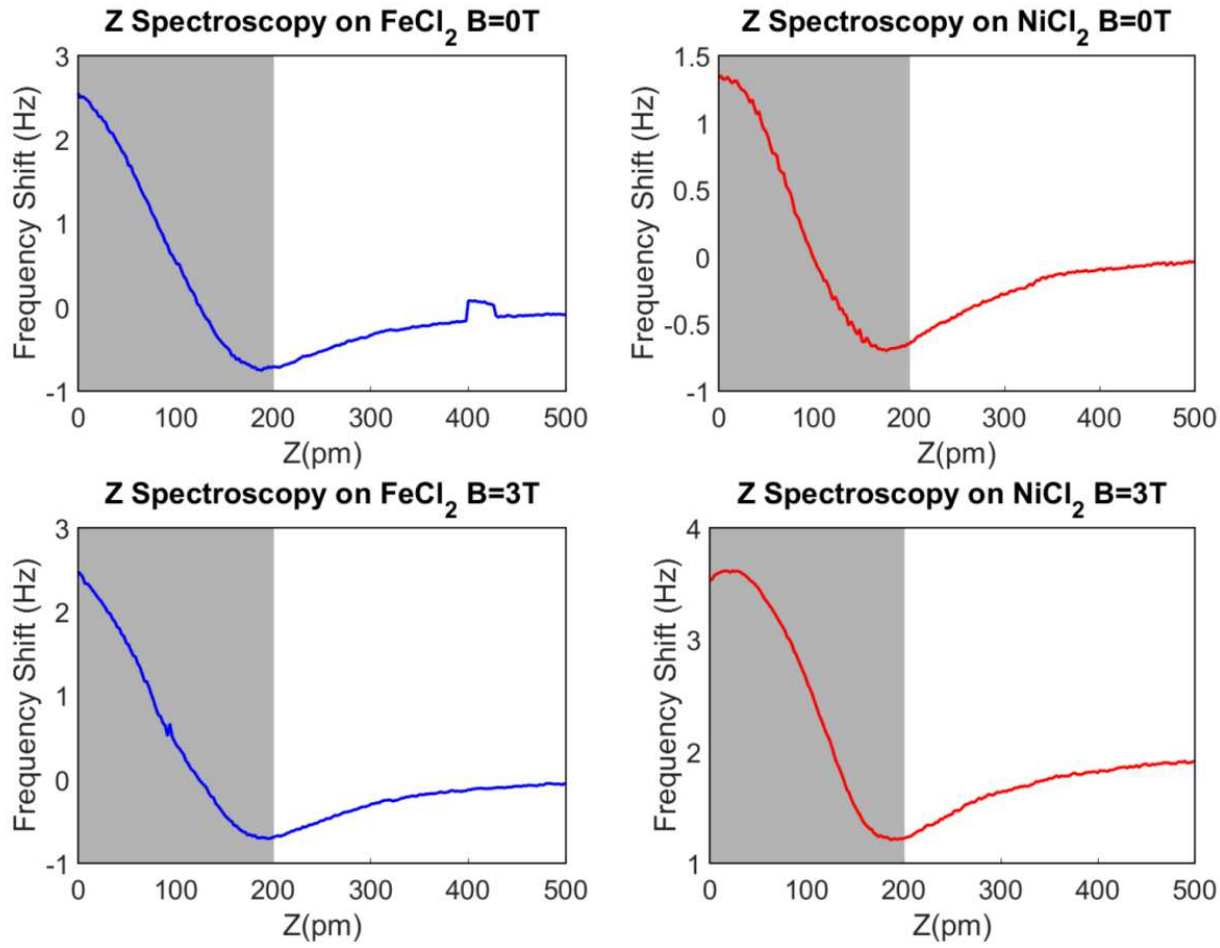

Figure 3.17: Z spectroscopy from nc-AFM frequency shift vs distance from the nickelocene maps shown in Fig. 3.14. The shaded area indicates the lifting regime followed in the experiments.

Conclusions

This thesis showcases the nickelocene STM probe's capability for magnetic characterization of molecular systems by determining physical variables such as spin, magnetic anisotropy, direction of magnetization, exchange coupling strength, etc. It also provides additional insights into studying systems whose magnetism cannot be explained solely by a two-site Heisenberg model.

The combination of Inelastic Electron Tunneling Spectroscopy (IETS) with atomically precise spectroscopic resolution, along with the magnetic contrast provided by the nickelocene tip, complements information obtained from averaging techniques such as XMCD, XPS, XAS, ARPES, etc. It surpasses the limited magnetic information obtained from Scanning Tunneling Spectroscopy (STS) with a metallic STM tip. As an added benefit, it brings to light the effect of orthogonal magnetic anisotropies on the exchange coupling and can benefit from the nc-AFM height determination.

The knowledge and expertise acquired in this thesis can also be applied to other metallocenes for their use as STM magnetic sensors, such as cobaltocene ($CoCp_2$) or vanadocene (VCp_2). Specifically, cobaltocene, with a spin $S = 1/2$, has already found application in magnetic sensing [53], attributed to its current enhancement nature around the Fermi energy (E_F). This contrasts with the ± 4 meV dip observed in nickelocene's dI/dV spectrum. Such distinctions may unveil additional features or enable access to transitions not allowed by the S=1 selection rules of nickelocene.

This thesis demonstrates the applicability of the theoretical framework used for nickelocene to be similar for the cobaltocene molecule, still to be fully adapted to the cobaltocene's electronic properties. Experimental evidence further supports its similarity in usage when

compared to nickelocene, with the only drawback being its exclusive deposition on a Cu sample.

As a final remark, nickelocene and, especially, cobaltocene may also have potential as an Electron Spin Resonance (ESR) tip functionalization to enhance the signal or magnetic characteristics of the probed systems [30].

Bibliography

[1] Gerd Binnig, Heinrich Rohrer, Ch Gerber, and Edmund Weibel. Surface studies by scanning tunneling microscopy. *Phis. Rev. Lett.*, 49(1):57, 1982.

[2] Bert Voigtländer. *Scanning probe microscopy: Atomic force microscopy and scanning tunneling microscopy*. Springer, 2015.

[3] Gerd Binnig and Heinrich Rohrer. Scanning tunneling microscopy. *Surf. Sci.*, 126 (1-3):236–244, 1983.

[4] Joseph A Stroscio and William J Kaiser. *Scanning tunneling microscopy*, volume 27. Academic press, 1993.

[5] John Bardeen. Tunnelling from a many-particle point of view. *Phis. Rev. Lett.*, 6(2): 57, 1961.

[6] VL Mironov. of the scanning probe microscopy.

[7] Mehmet Z Baykara. Noncontact atomic force microscopy for atomic-scale characterization of material surfaces. *Surf. Sci. Tools for Nanomaterials Characterization*, pages 273–316, 2015.

[8] Gerd Binnig, Calvin F Quate, and Ch Gerber. Atomic force microscope. *Phis. Rev. Lett.*, 56(9):930, 1986.

[9] Benjamín José Mallada Faes. Chemical and physical properties of molecular nanostructures on surfaces investigated by means of scanning probe microscopy. 2023.

[10] Ales Cahlik. Study of molecular structures on solid surfaces with scanning probe microscopy. 2021.

[11] Franz J Giessibl. Principle of nc-afm. In *Noncontact atomic force microscopy*, pages 11–46. Springer, 2002.

[12] Franz J Giessibl. Principles and applications of the qplus sensor. In *Noncontact Atomic Force Microscopy: Volume 2*, pages 121–142. Springer, 2009.

[13] Thomas R Albrecht, Peter Grütter, David Horne, and Daniel Rugar. Frequency modulation detection using high-q cantilevers for enhanced force microscope sensitivity. *Journal of applied physics*, 69(2):668–673, 1991.

[14] Specs surface nano analysis. kolibrisensor brochure [online]. available from: www.specs-group.com.

[15] Franz J Giessibl, Florian Pielmeier, Toyoaki Eguchi, Toshu An, and Yukio Hasegawa. Comparison of force sensors for atomic force microscopy based on quartz tuning forks and length-extensional resonators. *Phys. Rev. B*, 84(12):125409, 2011.

[16] Jhon P Ibe, Paul P Bey Jr, Susan L Brandow, Robert A Brizzolara, Nancy A Burnham, Daniel P DiLella, Kok P Lee, Christie RK Marrian, and Richard J Colton. On the electrochemical etching of tips for scanning tunneling microscopy. *Journal of Vacuum Science & Technology A: Vacuum, Surfaces, and Films*, 8(4):3570–3575, 1990.

[17] MJ Vasile, DA Grigg, JE Griffith, EA Fitzgerald, and PE Russell. Scanning probe tips formed by focused ion beams. *Review of scientific instruments*, 62(9):2167–2171, 1991.

[18] Leo Gross, Fabian Mohn, Nikolaj Moll, Peter Liljeroth, and Gerhard Meyer. The chemical structure of a molecule resolved by atomic force microscopy. *Science*, 325 (5944):1110–1114, 2009.

[19] Prokop Hapala, Georgy Kichin, Christian Wagner, F Stefan Tautz, Ruslan Temirov, and Pavel Jelínek. Mechanism of high-resolution stm/afm imaging with functionalized tips. *Phys. Rev. B*, 90(8):085421, 2014.

[20] Fabian Mohn, Bruno Schuler, Leo Gross, and Gerhard Meyer. Different tips for high-resolution atomic force microscopy and scanning tunneling microscopy of single molecules. *Applied Physics Letters*, 102(7), 2013.

[21] Taras Chutora, Bruno de la Torre, Pingo Mutombo, Jack Hellerstedt, Jaromír Kopeček, Pavel Jelínek, and Martin Švec. Nitrous oxide as an effective afm tip functionalization: a comparative study. *Beilstein journal of nanotechnology*, 10(1):315–321, 2019.

[22] B Mallada, A Gallardo, M Lamanec, B De La Torre, V Špirko, Pavel Hobza, and P Jelinek. Real-space imaging of anisotropic charge of σ-hole by means of kelvin probe force microscopy. *Science*, 374(6569):863–867, 2021.

[23] Roland Wiesendanger, H-J Güntherodt, G Güntherodt, RJ Gambino, and R Ruf. Observation of vacuum tunneling of spin-polarized electrons with the scanning tunneling microscope. *Phis. Rev. Lett.*, 65(2):247, 1990.

[24] Sebastian Loth, Christopher P Lutz, and Andreas J Heinrich. Spin-polarized spin excitation spectroscopy. *New Jour. Phys.*, 12(12):125021, 2010.

[25] A Kubetzka, M Bode, O Pietzsch, and R Wiesendanger. Spin-polarized scanning tunneling microscopy with antiferromagnetic probe tips. *Phis. Rev. Lett.*, 88(5): 057201, 2002.

[26] Roland Wiesendanger. *Atomic-and Nanoscale Magnetism*. Springer, 2018.

[27] Stephen Blundell. *Magnetism in condensed matter*. OUP Oxford, 2001.

[28] Joseph A Stroscio and DM Eigler. Atomic and molecular manipulation with the scanning tunneling microscope. *Science*, 254(5036):1319–1326, 1991.

[29] Markus Ternes, Christopher P Lutz, Andreas J Heinrich, and Wolf-Dieter Schneider. Sensing the spin of an individual ce adatom. *Phis. Rev. Lett.*, 124(16):167202, 2020.

[30] Susanne Baumann, William Paul, Taeyoung Choi, Christopher P Lutz, Arzhang Ardavan, and Andreas J Heinrich. Electron paramagnetic resonance of individual atoms on a surface. *Science*, 350(6259):417–420, 2015.

[31] Kasturi Vasudevan. *Basic Electronic Circuits: Problems and Solutions*. Springer Nature, 2022.

[32] Femto. Femto preamp dlpca-200 datasheet. Technical report, Femto, 2019.

[33] Chuan-Zheng Lee. Operational amplifiers engr 40m lecture notes. Technical report, Stanford University, 2017.

[34] Jerry Tersoff and Donald R Hamann. Theory and application for the scanning tunneling microscope. *Phis. Rev. Lett.*, 50(25):1998, 1983.

[35] Markus Ternes. Scanning tunneling spectroscopy at the single atom scale (phd thesis). 2006.

[36] SR830 STANFORD RESEARCH SYSTEMS. Digital lock-in amplifiers [online],. Technical report, www.thinksrs.com.

[37] C Julian Chen. *Introduction to Scanning Tunneling Microscopy Third Edition*, volume 69. Oxford University Press, USA, 2021.

[38] Andreas J Heinrich, Jay A Gupta, Christopher P Lutz, and Donald M Eigler. Single-atom spin-flip spectroscopy. *Science*, 306(5695):466–469, 2004.

[39] John H Scofield. Frequency-domain description of a lock-in amplifier. *Am. J. Phys.*, 62(2):129–133, 1994.

[40] Zurich Instruments. Principles of lock-in detection and the state of the art. Technical report, Zurich Instruments, 2016.

[41] G. Bradley Armen. Phase sensitive detection: the lock-in amplifier. Technical report, The University of Tennessee, Department of Physics and Astronomy.

[42] John M Birmingham. Synthesis of cyclopentadienyl metal compounds. In *Advances in Organometallic Chemistry*, volume 2, pages 365–413. Elsevier, 1965.

[43] Helmut Werner and Helmut Werner. A scientific revolution: The discovery of the sandwich complexes. *Landmarks in Organo-Transition Metal Chemistry: A Personal View*, pages 1–48, 2009.

[44] Didier Astruc. *Organometallic chemistry and catalysis*, volume 291. Springer, 2007.

[45] Maider Ormaza, Paula Abufager, Benjamin Verlhac, Nicolas Bachellier, M-L Bocquet, Nicolás Lorente, and Laurent Limot. Controlled spin switching in a metallocene molecular junction. *Nat. Com.*, 8(1):1974, 2017.

[46] Nicolas Bachellier. On-surface spin detection and doping of metallocenes (phd thesis). 2016.

[47] Kei Yosida. *Theory of magnetism.: Edition en anglais*, volume 122. Springer Science & Business Media, 1996.

[48] Michael Mohr, Manuel Gruber, Alexander Weismann, David Jacob, Paula Abufager, Nicolás Lorente, and Richard Berndt. Spin dependent transmission of nickelocene-cu contacts probed with shot noise. *Phys. Rev. B*, 101(7):075414, 2020.

[49] Gregory Czap, Peter J Wagner, Feng Xue, Lei Gu, Jie Li, Jiang Yao, Ruqian Wu, and W Ho. Probing and imaging spin interactions with a magnetic single-molecule sensor. *Science*, 364(6441):670–673, 2019.

[50] Jan Berger, Martin Ondráček, Oleksandr Stetsovych, Pavel Malỳ, Petr Holỳ, Jiří Rybáček, Martin Švec, Irena G Stará, Tomáš Mančal, Ivo Starỳ, et al. Quantum dissipation driven by electron transfer within a single molecule investigated with atomic force microscopy. *Nat. Com.*, 11(1):1337, 2020.

[51] Maider Ormaza, Paula Abufager, Nicolas Bachellier, Roberto Robles, Martin Verot, Tangui Le Bahers, Marie-Laure Bocquet, Nicolas Lorente, and Laurent Limot. Assembly of ferrocene molecules on metal surfaces revisited. *The Journal of Physical Chemistry Letters*, 6(3):395–400, 2015.

[52] BW Heinrich, L Limot, MV Rastei, C Iacovita, JP Bucher, Duval Mbongo Djimbi, Carlo Massobrio, and Mauro Boero. Dispersion and localization of electronic states at a ferrocene/cu (111) interface. *Phis. Rev. Lett.*, 107(21):216801, 2011.

[53] Léo Garnier, Benjamin Verlhac, Paula Abufager, Nicolás Lorente, Maider Ormaza, and Laurent Limot. The kondo effect of a molecular tip as a magnetic sensor. *Nano Lett.*, 20(11):8193–8199, 2020.

[54] Maider Ormaza, Nicolas Bachellier, Marisa N Faraggi, Benjamin Verlhac, Paula Abufager, Philippe Ohresser, Loıc Joly, Michelangelo Romeo, Fabrice Scheurer, M-L Bocquet, et al. Single-molecule enhanced spin-flip detection. *arXiv preprint arXiv:1611.00534*, 2016.

[55] N. Bachellier, M. Ormaza, M. Faraggi, B. Verlhac, M. Vérot, T. Le Bahers, M.-L. Bocquet, and L. Limot. Unveiling nickelocene bonding to a noble metal surface. *Phys. Rev. B*, 93:195403, May 2016. doi: 10.1103/PhysRevB.93.195403. URL `https://link.aps.org/doi/10.1103/PhysRevB.93.195403`.

[56] Maider Ormaza, Nicolas Bachellier, Marisa N Faraggi, Benjamin Verlhac, Paula Abufager, Philippe Ohresser, Loïc Joly, Michelangelo Romeo, Fabrice Scheurer, Marie-Laure Bocquet, et al. Efficient spin-flip excitation of a nickelocene molecule. *Nano Lett.*, 17(3):1877–1882, 2017.

[57] Gregory Czap, Peter J Wagner, Jie Li, Feng Xue, Jiang Yao, R Wu, and W Ho. Detection of spin-vibration states in single magnetic molecules. *Phis. Rev. Lett.*, 123 (10):106803, 2019.

[58] Nicolas Bachellier, Benjamin Verlhac, L Garnier, J Zaldívar, Carmen Rubio-Verdú, Paula Abufager, Maider Ormaza, D-J Choi, M-L Bocquet, José I Pascual, et al. Vibron-assisted spin excitation in a magnetically anisotropic molecule. *Nat. Com.*, 11 (1):1619, 2020.

[59] D.L. Pugmire, C.M. Woodbridge, N.M. Boag, and M.A. Langell. Adsorption and decomposition of nickelocene on ag(100): a high-resolution electron energy loss spectroscopy and temperature programmed desorption study. *Surf. Sci.*, 472(3):155–171, 2001. ISSN 0039-6028. doi: https://doi.org/10.1016/S0039-6028(00)00939-0. URL `https://www.sciencedirect.com/science/article/pii/S0039602800009390`.

[60] Peter Atkins, Julio De Paula, and James Keeler. *Atkins' physical chemistry*. Oxford university press, 2023.

[61] Cyrus F Hirjibehedin, Chiung-Yuan Lin, Alexander F Otte, Markus Ternes, Christopher P Lutz, Barbara A Jones, and Andreas J Heinrich. Large magnetic anisotropy

of a single atomic spin embedded in a surface molecular network. *Science*, 317(5842): 1199–1203, 2007.

[62] Juha Vaara, Syed Awais Rouf, and Jiri Mares. Magnetic couplings in the chemical shift of paramagnetic nmr. *Journal of chemical theory and computation*, 11(10): 4840–4849, 2015.

[63] Benjamin Verlhac, Nicolas Bachellier, L Garnier, Maider Ormaza, Paula Abufager, Robles Robles, M-L Bocquet, Markus Ternes, Nicolás Lorente, and Laurent Limot. Atomic-scale spin sensing with a single molecule at the apex of a scanning tunneling microscope. *Science*, 366(6465):623–627, 2019.

[64] Erik Koch. Exchange mechanisms. *Correlated electrons: from models to materials*, 2: 1–31, 2012.

[65] Jonathan Keeling. Quantum magnetism. *Lecture notes. University of St. Andrews*, 2008.

[66] Cyrus F Hirjibehedin, Christopher P Lutz, and Andreas J Heinrich. Spin coupling in engineered atomic structures. *Science*, 312(5776):1021–1024, 2006.

[67] S Meierott, N Néel, and J Kröger. Kondo effect of single co atoms on au (110). *Phys. Rev. B*, 91(20):201111, 2015.

[68] AF Otte, M Ternes, S Loth, CP Lutz, CF Hirjibehedin, and AJ Heinrich. Spin excitations of a kondo-screened atom coupled to a second magnetic atom. *Phis. Rev. Lett.*, 103(10):107203, 2009.

[69] Jenny C Oberg, M Reyes Calvo, Fernando Delgado, María Moro-Lagares, David Serrate, David Jacob, Joaquín Fernández-Rossier, and Cyrus F Hirjibehedin. Control

of single-spin magnetic anisotropy by exchange coupling. *Nat. Nano.*, 9(1):64–68, 2014.

[70] Nicolás Lorente and Jean-Pierre Gauyacq. Efficient spin transitions in inelastic electron tunneling spectroscopy. *Phys. Rev. Lett.*, 103:176601, Oct 2009. doi: 10.1103/PhysRevLett.103.176601. URL `https://link.aps.org/doi/10.1103/PhysRevLett.103.176601`.

[71] Joaquín Fernández-Rossier. Theory of single-spin inelastic tunneling spectroscopy. *Phis. Rev. Lett.*, 102(25):256802, 2009.

[72] F Delgado and J Fernández-Rossier. Cotunneling theory of atomic spin inelastic electron tunneling spectroscopy. *Phys. Rev. B*, 84(4):045439, 2011.

[73] Alexander Ako Khajetoorians, Tobias Schlenk, Benedikt Schweflinghaus, Manuel dos Santos Dias, Manuel Steinbrecher, Mohammed Bouhassoune, Samir Lounis, Jens Wiebe, and Roland Wiesendanger. Spin excitations of individual fe atoms on pt (111): impact of the site-dependent giant substrate polarization. *Phis. Rev. Lett.*, 111(15): 157204, 2013.

[74] T Balashov, T Schuh, AF Takács, A Ernst, S Ostanin, J Henk, I Mertig, P Bruno, T Miyamachi, S Suga, et al. Magnetic anisotropy and magnetization dynamics of individual atoms and clusters of fe and co on pt (111). *Phis. Rev. Lett.*, 102(25): 257203, 2009.

[75] Alexander Ako Khajetoorians, Samir Lounis, Bruno Chilian, Antonio T Costa, Lihui Zhou, Douglas L Mills, Jens Wiebe, and Roland Wiesendanger. Itinerant nature of atom-magnetization excitation by tunneling electrons. *Phis. Rev. Lett.*, 106(3):037205, 2011.

[76] Manish Kumar. Nicklocene as spin sensor (python script). URL `https://github.com/ManishMitharwall/Nickelocene_Spin_Sensor`.

[77] Shaotang Song, Pei Wen Ng, Shayan Edalatmanesh, Andrés Pinar Solé, Xinnan Peng, Jindřich Kolorenč, Zdenka Sosnová, Oleksander Stetsovych, Jie Su, Jing Li, et al. Designer magnetic topological graphene nanoribbons. *arXiv preprint arXiv:2204.12880*, 2022.

[78] Shaotang Song, Andrés Pinar Solé, Adam Matěj, Guangwu Li, Oleksandr Stetsovych, Diego Soler, Huimin Yang, Mykola Telychko, Jing Li, Manish Kumar, et al. Highly entangled polyradical nanographene with coexisting strong correlation and topological frustration. *Nat. Chem.*, pages 1–7, 2024.

[79] Christian Wackerlin, Ales Cahlik, Joseba Goikoetxea, Oleksandr Stetsovych, Daria Medvedeva, Jesús Redondo, Martin Svec, Bernard Delley, Martin Ondracek, Andres Pinar, et al. Role of the magnetic anisotropy in atomic-spin sensing of 1d molecular chains. *ACS nano*, 16(10):16402–16413, 2022.

[80] Thijs Stuyver, Bo Chen, Tao Zeng, Paul Geerlings, Frank De Proft, and Roald Hoffmann. Do diradicals behave like radicals? *Chemical reviews*, 119(21):11291–11351, 2019.

[81] Leonhard Grill, Matthew Dyer, Leif Lafferentz, Mats Persson, Maike V Peters, and Stefan Hecht. Nano-architectures by covalent assembly of molecular building blocks. *Nat. Nano.*, 2(11):687–691, 2007.

[82] Tao Wang and Junfa Zhu. Confined on-surface organic synthesis: strategies and mechanisms. *Surf. Sci. Pep.*, 74(2):97–140, 2019.

[83] Philipp Alexander Held, Harald Fuchs, and Armido Studer. Covalent-bond formation via on-surface chemistry. *Chem. Eur. J.*, 23(25):5874–5892, 2017.

[84] Lei Dong, Pei Nian Liu, and Nian Lin. Surface-activated coupling reactions confined on a surface. *Acc. Chem. Res.*, 48(10):2765–2774, 2015.

[85] Shaotang Song, Jie Su, Mykola Telychko, Jing Li, Guangwu Li, Ying Li, Chenliang Su, Jishan Wu, and Jiong Lu. On-surface synthesis of graphene nanostructures with π-magnetism. *Chemical Society Reviews*, 50(5):3238–3262, 2021.

[86] Dimas G de Oteyza and Thomas Frederiksen. Carbon-based nanostructures as a versatile platform for tunable π-magnetism. *Journal of Physics: Condensed Matter*, 34(44):443001, 2022.

[87] Jeremy Hieulle, Silvia Castro, Niklas Friedrich, Alessio Vegliante, Francisco Romero Lara, Sofía Sanz, Dulce Rey, Martina Corso, Thomas Frederiksen, Jose Ignacio Pascual, et al. On-surface synthesis and collective spin excitations of a triangulene-based nanostar. *Angewandte Chemie International Edition*, 60(48):25224–25229, 2021.

[88] Shantanu Mishra, Doreen Beyer, Kristjan Eimre, Junzhi Liu, Reinhard Berger, Oliver Groning, Carlo A Pignedoli, Klaus Mullen, Roman Fasel, Xinliang Feng, et al. Synthesis and characterization of π-extended triangulene. *JACS*, 141(27):10621–10625, 2019.

[89] Niko Pavliček, Anish Mistry, Zsolt Majzik, Nikolaj Moll, Gerhard Meyer, David J Fox, and Leo Gross. Synthesis and characterization of triangulene. *Nat. Nano.*, 12(4): 308–311, 2017.

[90] Shantanu Mishra, Gonçalo Catarina, Fupeng Wu, Ricardo Ortiz, David Jacob, Kristjan Eimre, Ji Ma, Carlo A Pignedoli, Xinliang Feng, Pascal Ruffieux, et al. Observation of fractional edge excitations in nanographene spin chains. *Nature*, 598(7880):287–292, 2021.

[91] Oleg V Yazyev. Emergence of magnetism in graphene materials and nanostructures. *Rep. Prog. Phys.*, 73(5):056501, 2010.

[92] E Clar and M Zander. 378. 1: 12-2: 3-10: 11-tribenzoperylene. *Journal of the Chemical Society*, pages 1861–1865, 1958.

[93] Erich Clar and Regina Schoental. *Polycyclic hydrocarbons*, volume 2. Springer, 1964.

[94] Miquel Solà. Forty years of clar's aromatic π-sextet rule. *Front. Chem.*, page 22, 2013.

[95] Nicolas Roch, Serge Florens, Theo A Costi, Wolfgang Wernsdorfer, and Franck Balestro. Observation of the underscreened kondo effect in a molecular transistor. *Phis. Rev. Lett.*, 103(19):197202, 2009.

[96] Piers Coleman and C Pépin. Singular fermi liquid behavior in the underscreened kondo model. *Phys. Rev. B*, 68(22):220405, 2003.

[97] V Madhavan, W Chen, T Jamneala, MF Crommie, and NS Wingreen. Tunneling into a single magnetic atom: spectroscopic evidence of the kondo resonance. *Science*, 280(5363):567–569, 1998.

[98] Björn O Roos. The complete active space self-consistent field method and its applications in electronic structure calculations. *Advances in Chemical Physics: Ab Initio Methods in Quantum Chemistry Part 2*, 69:399–445, 1987.

[99] Vijai M Santhini, Christian Wäckerlin, Aleš Cahlík, Martin Ondráček, Simon Pascal, Adam Matěj, Oleksandr Stetsovych, Pingo Mutombo, Petr Lazar, Olivier Siri, et al. 1d coordination π–d conjugated polymers with distinct structures defined by the choice of the transition metal: Towards a new class of antiaromatic macrocycles. *Angewandte Chemie International Edition*, 60(1):439–445, 2021.

[100] Mathieu Koudia, Elena Nardi, Olivier Siri, and Mathieu Abel. On-surface synthesis of covalent coordination polymers on micrometer scale. *Nano Res.*, 10:933–940, 2017.

[101] Hassan Denawi, Mathieu Koudia, Roland Hayn, Olivier Siri, and Mathieu Abel. On-surface synthesis of spin crossover polymeric chains. *The Journal of Physical Chemistry C*, 122(26):15033–15040, 2018.

[102] Hassan Denawi, Mathieu Abel, and Roland Hayn. Magnetic polymer chains of transition metal atoms and zwitterionic quinone. *The Journal of Physical Chemistry C*, 123(7):4582–4589, 2019.

[103] Hassan Denawi, Elena Nardi, Mathieu Koudia, Olivier Siri, Mathieu Abel, and Roland Hayn. Magnetic polymer chains of iron and zwitterionic quinoidal ligands on the ag (111) surface. *The Journal of Physical Chemistry C*, 124(2):1346–1351, 2019.

[104] Jing Liu, Yifan Gao, Tong Wang, Qiang Xue, Muqing Hua, Yongfeng Wang, Li Huang, and Nian Lin. Collective spin manipulation in antiferroelastic spin-crossover metallo-supramolecular chains. *ACS nano*, 14(9):11283–11293, 2020.

[105] Jing Liu, Jie Li, Qiwei Chen, Qiang Xue, Yifan Wang, Bin Di, Yongfeng Wang, and Kai Wu. Lattice-directed stabilization of different spin-state phases in metallo-supramolecular chains on au surfaces. *Chemistry of Materials*, 33(15):6166–6175, 2021.

[106] HO Frota. Shape of the kondo resonance. *Phys. Rev. B*, 45(3):1096, 1992.

[107] Henning Prüser, Piet E Dargel, Mohammed Bouhassoune, Rainer G Ulbrich, Thomas Pruschke, Samir Lounis, and Martin Wenderoth. Interplay between the kondo effect and the ruderman–kittel–kasuya–yosida interaction. *Nat. Com.*, 5(1):5417, 2014.

[108] Jan Girovsky, Jan Nowakowski, Md Ehesan Ali, Milos Baljozovic, Harald R Rossmann, Thomas Nijs, Elise A Aeby, Sylwia Nowakowska, Dorota Siewert, Gitika Srivastava, et al. Long-range ferrimagnetic order in a two-dimensional supramolecular kondo lattice. *Nat. Com.*, 8(1):15388, 2017.

[109] Kin Fai Mak, Jie Shan, and Daniel C Ralph. Probing and controlling magnetic states in 2d layered magnetic materials. *Nature Reviews Physics*, 1(11):646–661, 2019.

[110] Michael A McGuire. Crystal and magnetic structures in layered, transition metal dihalides and trihalides. *Crystals*, 7(5):121, 2017.

[111] Bevin Huang, Genevieve Clark, Efrén Navarro-Moratalla, Dahlia R Klein, Ran Cheng, Kyle L Seyler, Ding Zhong, Emma Schmidgall, Michael A McGuire, David H Cobden, et al. Layer-dependent ferromagnetism in a van der waals crystal down to the monolayer limit. *Nature*, 546(7657):270–273, 2017.

[112] Manuel Bonilla, Sadhu Kolekar, Yujing Ma, Horacio Coy Diaz, Vijaysankar Kalappattil, Raja Das, Tatiana Eggers, Humberto R Gutierrez, Manh-Huong Phan, and Matthias Batzill. Strong room-temperature ferromagnetism in vse2 monolayers on van der waals substrates. *Nat. Nano.*, 13(4):289–293, 2018.

[113] Cheng Gong, Lin Li, Zhenglu Li, Huiwen Ji, Alex Stern, Yang Xia, Ting Cao, Wei Bao, Chenzhe Wang, Yuan Wang, et al. Discovery of intrinsic ferromagnetism in two-dimensional van der waals crystals. *Nature*, 546(7657):265–269, 2017.

[114] Mohammad Amini, Adolfo O Fumega, Héctor González-Herrero, Viliam Vaňo, Shawulienu Kezilebieke, Jose L Lado, and Peter Liljeroth. Atomic-scale visualization of multiferroicity in monolayer nii _2. *arXiv preprint arXiv:2309.11217*, 2023.

[115] Djuro Bikaljevic, Carmen González-Orellana, Marina Pena-Díaz, Dominik Steiner, Jan Dreiser, Pierluigi Gargiani, Michael Foerster, Miguel Angel Nino, Lucía Aballe, Sandra Ruiz-Gomez, et al. Noncollinear magnetic order in two-dimensional nibr2 films grown on au (111). *ACS nano*, 15(9):14985–14995, 2021.

[116] ME Lines. Magnetic properties of co cl 2 and ni cl 2. *Phys. Rev.*, 131(2):546, 1963.

[117] MK Wilkinson, JW Cable, EO Wollan, and WC Koehler. Neutron diffraction investigations of the magnetic ordering in fe br 2, co br 2, fe cl 2, and co cl 2. *Phys. Rev.*, 113(2):497, 1959.

[118] Bentham instruments. Lock-in amplifiers [online],. Technical report, 2 Boulton Road, Reading, Berkshire, RG2 0NH.

[119] Arthur T Hubbard. Electrochemistry at well-characterized surfaces. *Chemical Reviews*, 88(4):633–656, 1988.

[120] Alex Saywell, Johannes K Sprafke, Louisa J Esdaile, Andrew J Britton, Anna Rienzo, Harry L Anderson, James N O'Shea, and Peter H Beton. Conformation and packing of porphyrin polymer chains deposited using electrospray on a gold surface. *Angewandte Chemie*, 122(48):9322–9325, 2010.

[121] VS Edel'man. Stm observation of twin microlayers on cleaved bismuth surfaces. *Physics Letters A*, 210(1-2):105–109, 1996.

[122] Marco Di Giovannantonio, Kristjan Eimre, Aliaksandr V Yakutovich, Qiang Chen, Shantanu Mishra, José I Urgel, Carlo A Pignedoli, Pascal Ruffieux, Klaus Mullen, Akimitsu Narita, et al. On-surface synthesis of antiaromatic and open-shell indeno [2, 1-b] fluorene polymers and their lateral fusion into porous ribbons. *JACS*, 141(31): 12346–12354, 2019.

[123] Qiang Sun, Bay V Tran, Liangliang Cai, Honghong Ma, Xin Yu, Chunxue Yuan, Meike Stöhr, and Wei Xu. On-surface formation of cumulene by dehalogenative homocoupling of alkenyl gem-dibromides. *Angewandte Chemie*, 129(40):12333–12337, 2017.

[124] Alissa Wiengarten, Knud Seufert, Willi Auwarter, David Ecija, Katharina Diller, Francesco Allegretti, Felix Bischoff, Sybille Fischer, David A Duncan, Anthoula C Papageorgiou, et al. Surface-assisted dehydrogenative homocoupling of porphine molecules. *JACS*, 136(26):9346–9354, 2014.

[125] Kalyan Biswas, Maxence Urbani, Ana Sánchez-Grande, Diego Soler-Polo, Koen Lauwaet, Adam Matej, Pingo Mutombo, Libor Veis, Jiri Brabec, Katarzyna Pernal, et al. Interplay between π-conjugation and exchange magnetism in one-dimensional porphyrinoid polymers. *JACS*, 144(28):12725–12731, 2022.

List of Figures

List of abbreviations

Ag Silver

ARPES Angle Resolved Photoemission Spectroscopy

Au Gold

CO Carbon monoxide

Co Cobalt

CoCp2 Cobaltocene

Cu Copper

DFT Density Functional Theory

ESR Electron Spin Resonance

Fe Iron

GNR Graphene nanoribbon

IETS Inelastic Electron Tunneling Spectroscopy

LDOS Local density of states

LN2 Liquid nitrogen

LHe Liquid helium

nc-AFM Non-Contact Atomic force microscopy

Ni Nickel

NiCp2 Nickelocene

OSS On-surface synthesis

SPM Scanning Probe Microscopy

STM Scanning tunneling microscopy

STS Scanning tunnelling spectroscopy

UHV Ultra-high vacuum

XMCD X-ray Magnetic Circular Dichroism

XAS X-ray Absorption Soectroscopy

XPS X-ray Photoelectron Spectroscopy

List of publications

1. **Role of the Magnetic Anisotropy in Atomic-Spin Sensing of 1D Molecular Chains**, Christian Wackerlin, Ales Cahlik, Joseba Goikoetxea, Oleksandr Stetsovych, Daria Medvedeva, Jesús Redondo, Martin Svec, Bernard Delley, Martin Ondracek, Andres Pinar, Maria Blanco-Rey, Jindrich Kolorenc, Andrés Arnau, Pavel Jelinek. (2021) *ACS Nano*, 16 (10), 16402-16413

2. **Designer magnetic topological graphene nanoribbons**, Shaotang Song, Pei Wen Ng, Shayan Edalatmanesh, Andrés Pinar Solé, Xinnan Peng, Jindřich Kolorenč, Zdenka Sosnová, Oleksander Stetsovych, Jie Su, Jing Li, Hongli Sun, Alexander Liebig, Chenliang Su, Jishan Wu, Franz J Giessibl, Pavel Jelinek, Chunyan Chi, Jiong Lu. (2022) *arXiv*, arXiv:2204.12880

3. **Highly-Entangled Polyradical Nanographene with Coexisting Strong Correlation and Topological Frustration**, Shaotang Song, Andrés Pinar Solé, Adam Matěj, Guangwu Li, Oleksandr Stetsovych, Diego Soler, Huimin Yang, Mykola Telychko, Jing Li, Manish Kumar, Jiri Brabec, Libor Veis, Jishan Wu, Pavel Jelinek, Jiong Lu. (2024), *Nature Chemistry* https://doi.org/10.1038/s41557-024-01453-9

4. **On-Surface Synthesis of Helicene Oligomers**, Andrés Pinar Solé, Jiří Klívar, Michal Šámal, Irena G. Stará, Ivo Starý, Jesús Mendieta, Karl-Heinz Ernst, Pavel Jelínek and Oleksandr Stetsovych. (2024) *Submitted to European Chemistry Journal.*

5. **Light-controlled multiconfigurational conductance switching in a single 1D metal-organic wire**, Aleš Cahlík, Martin Ondráček, Christian Wäckerlin, Andrés Pinar Solé, Olivier Siri, Martin Švec, Pavel Jelinek. (2024) *Submitted to ACS Nano*

6. **Designing highly delocalized solitons by harnessing the structural parity of π-conjugated polymers**, Jesús Janeiro, Aurelio Gallardo, Marco Lozano, Ana Barragán, Berta Alvarez, Diego Soler, Oleksandr Stetsovych, Andrés Pinar Solé, José M. Gallego, Dolores Pérez, Rodolfo Miranda, José Urgel, Pavel Jelinek, Diego Peña, Kalyan Biswas. (2024) *Submitted to Nature Synthesis*

7. **Unveiling the inter-layer interaction in a 1H/1T TaS2 van de Waals heterostructure**, Cosme G. Ayani, M. Bosnar, F. Calleja, Andrés Pinar Solé, O. Stetsovych, Iván M. Ibarburu, Clara Rebanal, Manuela Garnica1, Rodolfo Miranda, M. M. Otrokov, M. Ondraček, Pavel Jalínek, A. Arnau, Amadeo L. Vázquez de Parga. (2024) *Submitted to Nanoletters*

8. **Tunable ferromagnetic order in 2D layers of Transition Metal Dichlorides**, Andrea Aguirre, Andrés Pinar Solé, Diego Soler Polo, Carmen González-Orellana, Amitayush Thakur, Jon Ortuzar, Oleksandr Stesovych, Manish Kumar, Marina Peña-Díaz, Andrew Weber, Massimo Tallarida, Jan Dreiser, Matthias Muntwiler, Celia Rogero, J.I. Pascual, Pavel Jelínek, Maxim Ilyn, and Martina Corso. (2024) *Submitted to Advanced Materials*

Attachments

A.1 Lock-in setup

Apart from the generalities described in Section 1.6 for a lock-in amplifier, there are other important parameters to be taken into account like the input/output connections, sensitivity, gain and the dynamic reserve (some parameters for the Standford SR830 lock-in will be used as reference [36, 40, 41, 118]).

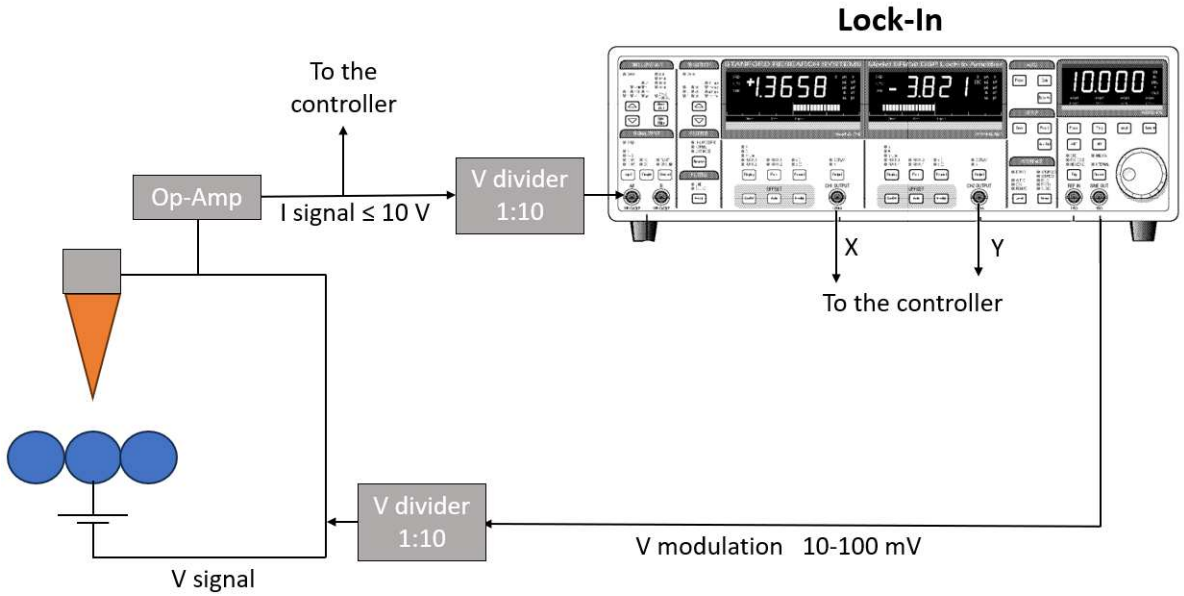

Figure 0.18: Signal connections and voltage dividers for a Standford SR380 lock-in [118].

The lock-in input signal is the current signal, and the output signals are the modulation, X, and Y signals (Fig. 0.18). The amplified current signal can be diminished by a voltage divider as a measure of protection (the lock-in accepts input signals with a maximum of 10 V). It is often filtered before the lock-in input connection to avoid external noise. The modulation signal must have the desired oscillation amplitude, which usually ranges between 1-10 mV; nevertheless, it may be set up to 10-100 mV to preserve the modulation signal

from losses through the cable. Another voltage divider lowers the modulation amplitude before it is injected into the bias signal, which will be modulated with the desired amplitude value. This signal can also be extra-filtered to avoid noise in the injection process.

The amplification or gain provided by the lock-in is split into two components: AC gain before the lock-in operations and DC gain following the lock-in phase detection. The AC gain amplifies the input signal's amplitude, while the DC gain amplifies the DC output. The gain is directly related to the lock-in's sensitivity as 10V/sensitivity (10V is a typical maximum for the gain full scale DC output). Normally, the sensitivity ranges between 2nV to 1V. Higher sensitivity means the lock-in can detect weaker input amplitudes. The key is to strike a balance between sensitivity and noise, ensuring that one has sufficient sensitivity to detect the signal while keeping noise at acceptable levels, while higher sensitivity leads to a lower gain. Too small sensitivity will lead to an excess of amplification that will saturate the amplifier's signal. The dynamic reserve is an indication of the lock-in's resistance to noise at frequencies away from the reference signal. It is given by $\mathrm{DM} = 20\log_{10}(V_n/V_s)$, where V_s is the signal's amplitude of interest and V_n is the amplitude of the noise signal. While the total gain is set by the sensitivity, the distribution of the AC and DC gain is set by the reserve. In the case of the Stanford SR830, the dynamic reserve recommended for measuring from 100nV to 5mV is 60 dB (HIGH); more reserve can increase the noise levels. To convert between volts per input (linear) to decibel (logarithmic) amplification, this expression can be utilized: Gain (dB) = $20\log_{10}$(Voltage Ratio). The lock-in has a digital low-pass filter [118] that prevents the noise and the modulation signal from spoiling the data acquisition. Usual values are 6, 12, 18, and 24 dB/oct rolloff. A dB/oct rolloff refers to the rate at which the signal's amplitude changes as the frequency increases or decreases. For example, in a filter with a 12 dB/octave rolloff, the signal level decreases by 12 decibels for every octave (double the frequency) increase. The frequency of oscillation should be lower than the cutoff frequency f_{cutoff}, and in this case, it is also limited by the

hardware to process the signal (Nanonis), so it is better to keep it below $1kHz$. The filter has usual values for time constants from 10s to 30Ks. Finally, the acquisition or integration time t_{aq} should be set properly to allow the filter to fully cancel the noise. It refers to the time it takes for a lock-in amplifier to synchronize with a reference signal. Higher frequency signals may allow for quicker acquisition of the measurement, but this also depends on the lock-in amplifier's bandwidth (cutoff). The filter settings on the lock-in amplifier can influence acquisition time. Narrower bandwidth filters may require longer acquisition times but protect better against noise. Also, the amplitude of the signal compared to the noise level plays a significant role in acquisition time. Stronger signals are easier to acquire and require shorter times. For a Standford SR830 lock-in, the acquisition times should be 2 cycles + 5 ms or 40 ms, whichever is greater. The acquisition time of the software utilized to process the signal also has to be taken into account and calculated minding the amount of pixels/mV when performing the dI/dV. Lastly, the analog signal from the lock-in must be converted into a digital signal to be processed by the analysis software by a digital-to-analog converter (DAC).

Here are some general settings to tune up a lock-in [2]:

- Cutoff frequency f_{cutoff}: Defines the bandwidth of the filter. A smaller bandwidth will have a bigger TC as it takes more time to filter.

- Time constant TC: Should be at least three times the acquisition time ($t_{\text{aq.}}$ = 2 cycles + 5 ms or 40 ms) and also three times the acquisition time per pixel of the dI/dV. Also depends on the filter's orders O. More orders offer more precision but increment the TC. A usual value is 300 ms.

$$TC = \frac{O}{2\pi f_{\text{cutoff}}} > \frac{3t_{\text{aq.}}}{\text{pixels}} \tag{10}$$

- Oscillation frequency f_0: Avoid even numbers and factors of 5 and 10, as they coincide

with the power line frequency of the electric cables. Maintain the frequency lower than the cutoff frequency of the filter, normally below 1 kHz. An example would be 827 Hz. To measure d^2I/dV^2, $f \approx f_0/2$.

$$f_0 > \frac{10}{TC} < f_{\text{cutoff}} \tag{11}$$

- Amplitude V_{mod}: has to be set minding the resolution of the spectroscopy (bias/pixel) and the features to resolve. Often, the amplitude should be at least five times lower than the bias feature to resolve. For low-energy dI/dV like IETS below $\pm$20 mV in range, amplitudes of 1-0.5 mV will resolve features like Kondo peaks and spin-flips. For band gap measurements from 100 mV to 2V, amplitudes of 2 to 5 mV may be required. Higher amplitudes will smooth the signal and decrease the resolution by smearing out the features.

$$V_{\text{mod}} > \frac{\text{Bias range}}{\text{pixels}} \tag{12}$$

- Gain: The op-amp from the acquisition software (Nanonis in this case) has to be set to a specific gain that will not saturate the current if performing measurements in an open loop. Modifications in the current signal gain will introduce phase shifts in the signal, so after a gain modification, the lock-in must be reset. Also, the sensitivity and reserve must be adjusted after an op-amp gain modification.

A.2 Sample preparation

Although SPM sample substrates can be made of a wide variety of materials, it is usually a metal monocrystal (Au, Cu, Ag, Pt, etc.) polished in a particular crystallographic plane. The standard process to clean samples in UHV and prepare them for SPM goes as follows[119]. Initially, the surface undergoes bombardment by Ar^+ ions with a sputtering gun (Fig. 0.19) using about 1 kV for 15 minutes, although these parameters may vary depending on the substrate and the amount of debris and impurities it presents. This action is aimed at eliminating the topmost layers. The sputtering (ion) gun is composed of a biased filament that ionizes the 6×10^{-5} mBar Ar atmosphere by electron bombardment and an anode-cathode configuration with an aperture to accelerate the plasma beam and collimate it towards the sample. The ion gun must be aligned to focus the beam correctly on the surface. This can be done by using 2 kV energy and 1×10^{-4} mBar of Ar to create a visible plasma beam and orient the sample accordingly. The Ar^+ ions will create a small current on the manipulator in the range of $1 - 20\mu A$, depending on the optimal conditions and energy applied. During the ion bombarding, the ion getter pump must be switched off or isolated by a gate to avoid Ar poisoning. Once the sample is clean, the substrate undergoes annealing by e-beam heating with a biased filament to heal the defects by mobilization of surface atoms by heat. The specific annealing temperature depends on the type of crystal, typically ranging from 400°C to 600°C for 20 minutes. The electrons from the filament will create a small current when reaching the sample, about 5 mA, which can be the control parameter for the annealing, apart from the high voltage bias input of 700 V.

Once the sample is clean, the object of study (generally molecular structures or single atoms) can be deposited under room temperature conditions, on a warmed-up sample, or in cryogenic conditions by depositing directly in the SPM chamber in UHV conditions. The most commonly used deposition technique consists of evaporating the materials and

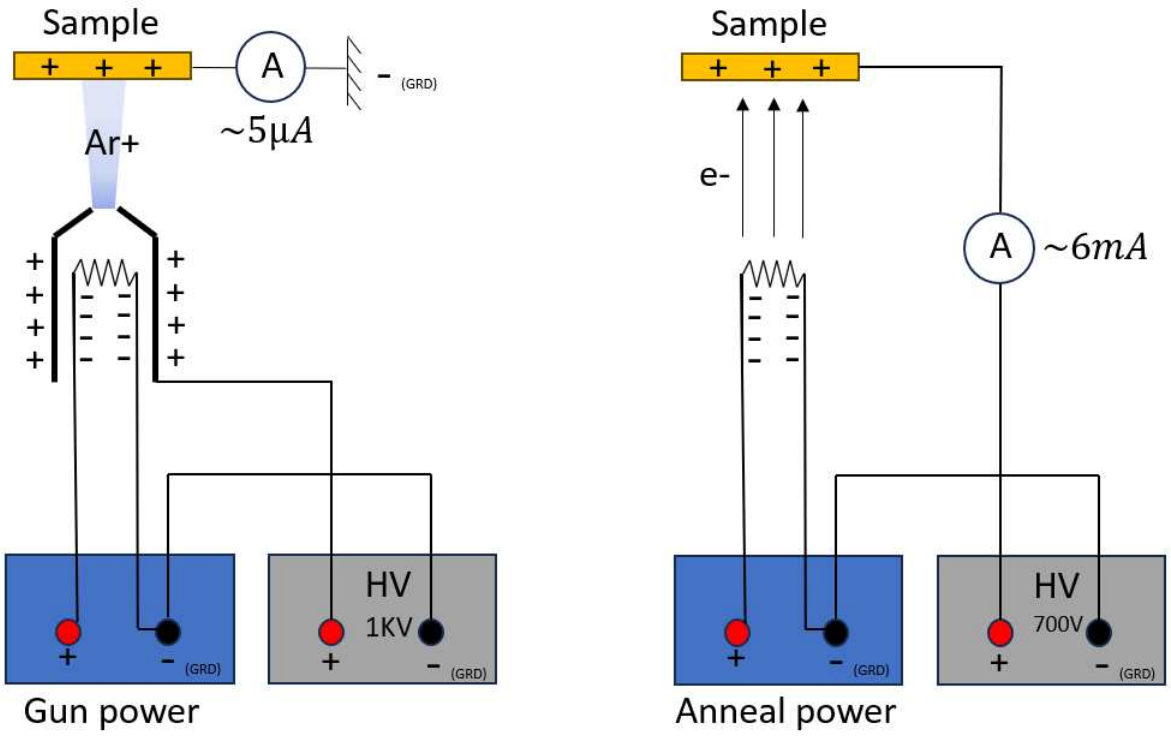

Figure 0.19: Sputtering (left) and annealing (right) setups.

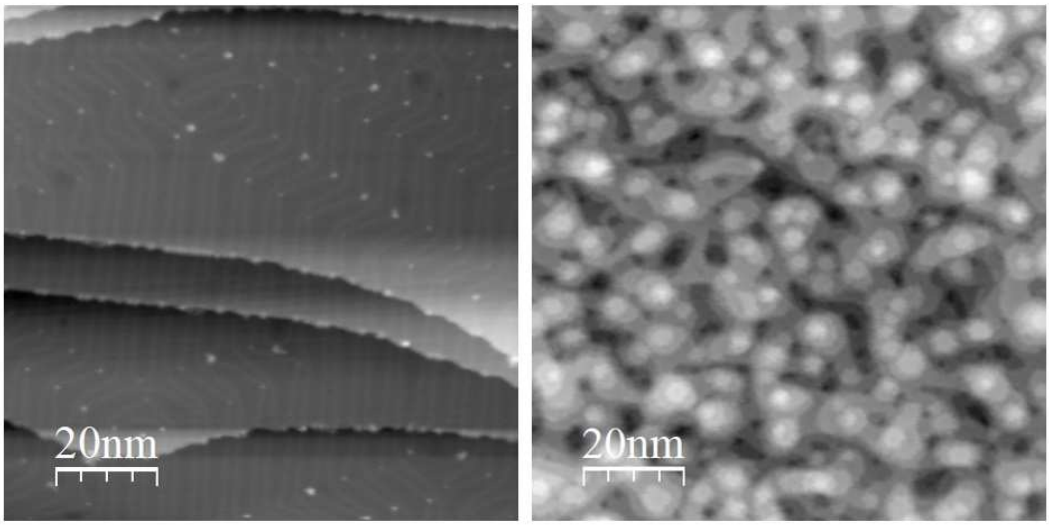

Figure 0.20: SPM images of an Au(111) crystal before (left) and after sputtering (right). The surface gets defected by the Ar^+ ion bombardment.

depositing them on the surface using Knudsen-cell evaporation. The molecular evaporator consists of a tantalum or quartz crucible where the molecules can be deposited, and a filament or some other element like a silicon carbide (SiC) wafer for resistive heating of the crucible to sublimate the molecules onto the bare sample. Different deposition rates and temperatures will result in different coverages, and by varying the sample temperature during the deposition, the absorption, kinetics, and molecular association of the molecules can be controlled as well. In the case of metals with a high sublimation temperature, a metal evaporator equipped with a filament and a high-voltage input can be used to allow e-beam heating to increase the temperature of the materials to the required levels. There are other techniques to prepare SPM samples, such as electrospray deposition[120] or UHV cleaving of a layered sample[121]. Furthermore, the system can be prepared through on-surface synthesis by catalytic Ullman coupling-like reactions[81–84], annealing the molecules to obtain different products [122], homocoupling[123], cyclodehydrogenation [124], or SPM/AFM atomic manipulation[125], for example, dehydrogenation to create radicals and derivatives (Fig. 0.21).

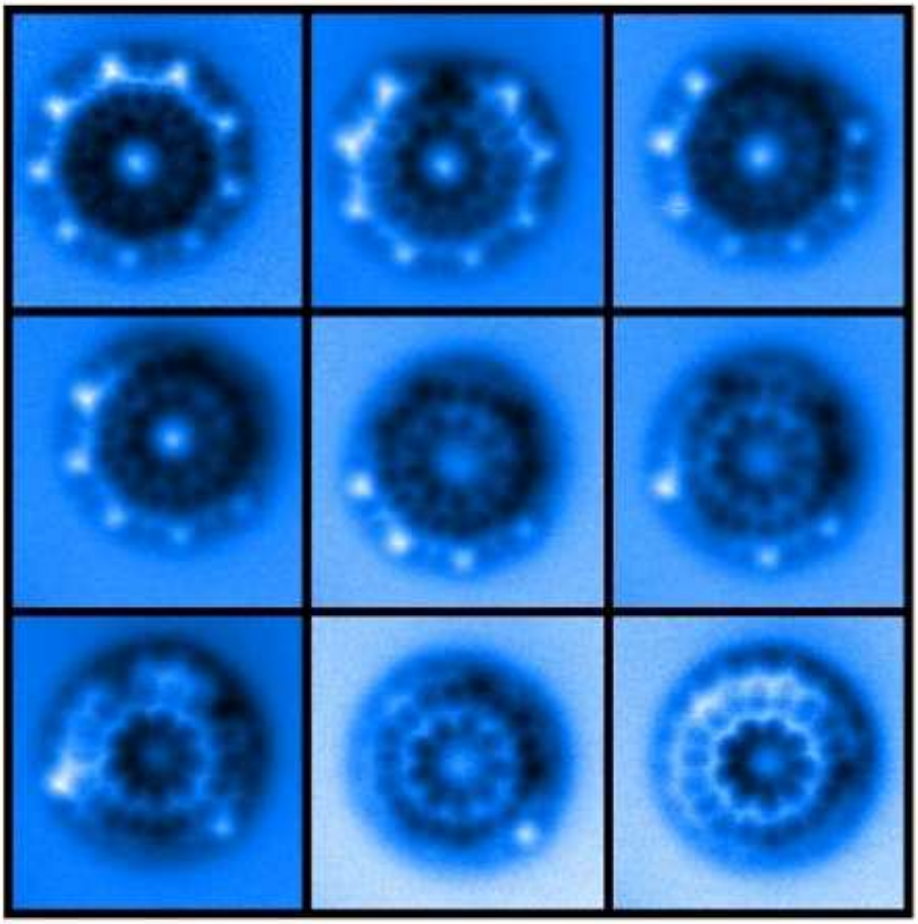

Figure 0.21: 2x2 nm^2 nc-AFM high resolution images of a process of a polyaromatic hydrocarbon ring dehydrogenation by bias pulsing with a CO functionalized tip. The white dots correspond to the H atoms protruding upwards. The top left image correspond to the original hydrogenated molecule, and the dehydrogenation ends on the right bottom image, where no H is left and the molecule planarizes on the Au(111) substrate. To dehydrogenate the molecule, the CO tip was located on top of the H and the bias was increased to 2.5-3 V keeping the current below 400pA.

A.3 Example: eigenvalues and eigenvectors for a $S = 1$ system with magnetic anisotropy

To obtain the energies and eigenfunctions of a $S = 1$ system we can utilize the following spin Hamiltonian:

$$\hat{H} = D\hat{S}_z^2 + E(\hat{S}_x^2 - \hat{S}_y^2) \tag{13}$$

Where D, E are the out of plane and in plane components of the magnetic anisotropy respectively. The spin matrices can be built from the Pauli matrices for $S = 1$ choosing $\hat{S}_z$ as the vertical axis ($\hat{S}_z |m_s\rangle = \hbar m_s$) in the basis $|1\rangle, |0\rangle, |-1\rangle \rightarrow (1,0,0), (0,1,0), (0,0,1)$:

$$\hat{S}_x, \hat{S}_y, \hat{S}_z = \frac{\hbar}{\sqrt{2}} \begin{pmatrix} 0 & 1 & 0 \\ 1 & 0 & 1 \\ 0 & 1 & 0 \end{pmatrix}, \quad \frac{\hbar}{\sqrt{2}} \begin{pmatrix} 0 & -i & 0 \\ i & 0 & -i \\ 0 & i & 0 \end{pmatrix}, \quad \hbar \begin{pmatrix} 1 & 0 & 0 \\ 0 & 0 & 0 \\ 0 & 0 & -1 \end{pmatrix} \tag{14}$$

After the matrix's square products, the Hamiltonian will look like:

$$\hat{H} = \hbar^2 \begin{pmatrix} D & 0 & E \\ 0 & 0 & 0 \\ E & 0 & D \end{pmatrix} \tag{15}$$

Diagonalizing this matrix $|H - I\lambda| = 0$ provides the energies (eigenvalues) and the secular equation (here as the time independent Schrodinger equation) $\hat{H} |\Psi\rangle = \epsilon |\Psi\rangle$ the eigenfunctions. Taking $\hbar = 1$ for simplicity, we obtain:

$$\epsilon_0 = 0 \quad |\Psi_0\rangle = (0,1,0) \rightarrow |0\rangle \tag{16}$$

$$\epsilon_1 = D + E \quad |\Psi_1\rangle = \left(\frac{1}{\sqrt{2}}, 0, \frac{1}{\sqrt{2}}\right) \rightarrow \frac{1}{\sqrt{2}}(|1\rangle + |-1\rangle) \tag{17}$$

$$\epsilon_2 = D - E \quad |\Psi_2\rangle = \left(\frac{1}{\sqrt{2}}, 0, \frac{-1}{\sqrt{2}}\right) \rightarrow \frac{1}{\sqrt{2}}(|1\rangle - |-1\rangle) \tag{18}$$

If $E = 0$ then $\epsilon_1 = \epsilon_2$ and we obtain the zero field splitting for a $S = 1$ system like in the nickelocene molecule:

$$\epsilon_0 = 0 \quad |\Psi_0\rangle = |0\rangle \tag{19}$$

$$\epsilon_{1,2} = D \quad |\Psi_{1,2}\rangle = |1\rangle, |-1\rangle \tag{20}$$

This operation is automatically performed by the Python script[76]. For a system with $S = 1, D = -0.23$ meV, Each eigenstate Ψ ordered by increasing energy is a linear combination of the basis vectors.

[0]	$\|1\|1\rangle$
[1]	$\|0\|1\rangle$
[2]	$\|-1\|1\rangle$
[3]	$\|1\|0\rangle$
[4]	$\|0\|0\rangle$
[5]	$\|-1\|0\rangle$
[6]	$\|1\|-1\rangle$
[7]	$\|0\|-1\rangle$
[8]	$\|-1\|-1\rangle$

Table 2: Ordered basis for the combined nickelocene (S=1) and M (S=3/2) system as displayed by the Python script[76] according to the last calculated value of J.

Fig. 0.22 represents a matrix provided by the script whose columns correspond with each eigenstate Ψ_0 (ground state) to Ψ_8 written by following the basis order described.

For example, the ground state is $\Psi_0 = 0.9\,|0|0\rangle - 0.2\,|1|-1\rangle$. The energy will be height dependent as J varies with the tip-sample distance.

	0	1	2	3	4	5	6	7	8
0	0.0	0.0	0.0	0.0	0.0	0.0	0.0	1.0	0.0
1	0.0	0.0	0.9	0.0	0.0	0.0	0.2	0.0	0.0
2	0.0	0.0	0.0	-0.7	0.7	0.0	0.0	0.0	0.0
3	0.0	0.0	-0.2	0.0	0.0	0.0	0.9	0.0	0.0
4	0.9	0.0	0.0	0.0	0.3	0.0	0.0	0.0	0.0
5	0.0	-0.2	0.0	0.0	0.0	0.9	0.0	0.0	0.0
6	-0.2	0.0	0.0	0.7	0.7	0.0	0.0	0.0	0.0
7	0.0	0.9	0.0	0.0	0.0	0.2	0.0	0.0	0.0
8	0.0	0.0	0.0	0.0	0.0	0.0	0.0	0.0	1.0

Figure 0.22: Eigenvectors Ψ as columns of the matrix offered by the Python script[76]. The numbers 0-8 correspond with the basis vectors from 2. The coefficients are rounded from their original output value.

In general, the script arranges the base vectors of the combined system $|m_{Nc}|m_M\rangle$ in the following way: $|1|m_M\rangle\,, |0|m_M\rangle\,, |-1|m_M\rangle\,, |1|m_M - 1\rangle\,|0|m_M - 1\rangle\,, |-1|m_M - 1\rangle$...

A.4 Nickelocene $d^2I/dV^2(z)$ example simulations

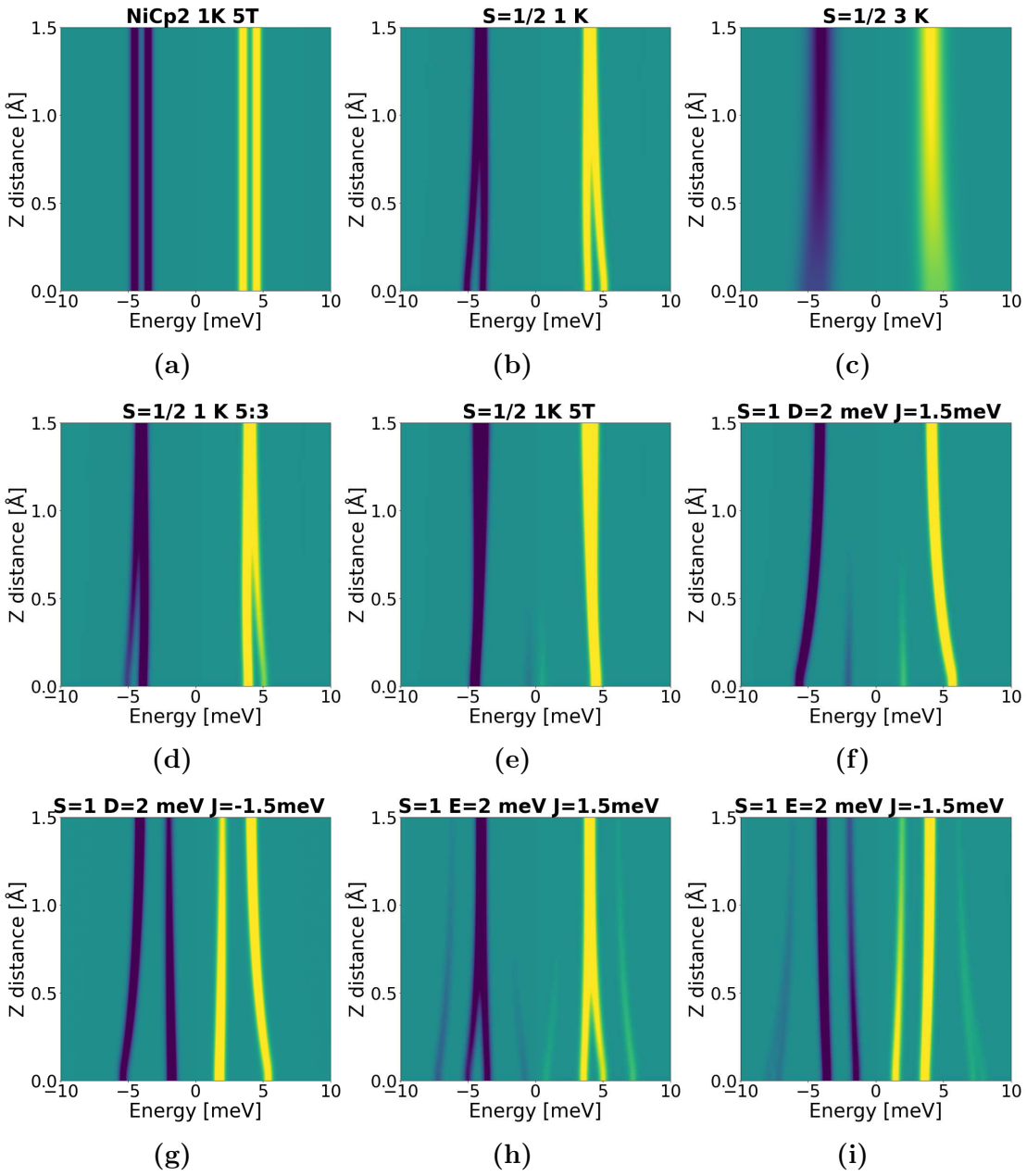

Figure 0.23: Nickelocene dI^2dV^2 simulations with the Python script[76] employing the Heisneberg model and the cotunneling theory. a) Zeeman splitting of the single nickelocene spectrum , the rest correspond to simulations of measurements of impurities with different spin S. Default parameters: T=1 K, $J = 1.5$ meV antiferromagnetic exchange coupling at the closest distance, 1.5 Åtip retraction, z decay $a = 1$ Å, a coupling strength favoring the impurity 1:3 and 0T magnetic field in the z direction. Parameters not present in the titles are set as default. In d) the coupling strength favors the nickelocene 5:3. D, E are the out-of-plane and in-plane anisotropies. Color map: yellow=higher positive value.